STRUCTURAL MASS SPECTROMETRY APPROACHES FOR THE STUDY OF COMPLEXED SMALL MOLECULES

By

Emanuel Zlibut

Dissertation
Submitted to the Faculty of the
Graduate School of Vanderbilt University
in partial fulfillment of the requirements
for the degree of

DOCTOR OF PHILOSOPHY
in

Chemistry

May 12, 2023

Nashville, Tennessee

Pending Approval:

John A. McLean, Ph.D.

Renã A. S. Robinson, Ph.D.

David E. Cliffel, Ph.D.

Jeffrey M. Spraggins, Ph.D.

Copyright © 2023 Emanuel Zlibut
All Rights Reserved

For my mother, who I think we can finally admit loves me best of all her children
For my wife, all the good in me is *because* of you
For God, all the good in me is *through* You
For my family whose unwavering love and sacrifice anchored me and made this all possible.

ACKNOWLEDGMENTS

Many thanks are due to the people that have impacted me along the way to here. Through the highs and lows these special individuals have kept me going.

Fascinated with drugs from a young age(not as a user, my mother was an in-home care provider), I began my academic studies as a pharmacy major at Fisk University. A special thanks to Prof. Natalie Y. Arnett for taking a chance on a young boy going nowhere fast and saving me from a life of professional drug dealing. I am grateful to Dr. Arnett for not only introducing me to the research field, but investing in me as an adviser and mentor. Under her guidance, I developed a solid chemistry foundation that has supported my success as a researcher.

Thank you to Prof. John A. McLean for providing me with a professional environment to learn, a supportive community, and access to resources necessary for developing as an analytical chemist specialized in IM-MS. Graduate school has required a lot of personal growth that at times was challenging, but Dr. McLean's kind and genuine support throughout the process was crucial in guiding me to the end and building my confidence. Thankful that throughout my graduate experience Dr. McLean actively supported all professional development opportunities(workshops, conferences, and fostering connections through industry collaborations) available to me.

Thank you to my committee, Chair. John A. McLean, Prof. Renã A. S. Robinson, Prof. David E. Cliffel, and Prof. Jeffrey M. Spraggins for facilitating a environment for discussions and scientific growth during our scheduled meetings.

It has been a team effort, all that I have been able to achieve as part of my dissertation work is through the support of many McLean lab members. When I joined the lab, Dr. James Dodds and Dr. Caleb Morris took the time to train me on the day to day maintenance and the process of running experiments on the Agilent 6560 platform. Dr. Jody C. May continued to reinforce that training and providing a space for intellectual conversations challenging my understanding of the instrumentation and the IM-MS field for the better. I would be an even greater fool than I am if not for Dr. May. We joined the lab the same year and shared in the experience together. Dr. Bailey Rose and Nadjali Chung are rockstars that pushed me to give it my all throughout the process. It has been a pleasure to overlap with Hawkins Shepard, David Koomen, Allison Reardon, Ben Blakely, Kyle Lira, and Alex Toler. I thank each of you for the laughs, scientific discussions, and stepping up to carrying the McLean lab research forward.

Thank you to our industry collaborators Agilent Technologies and Pfizer Inc. for the opportunity to learn and grow as a researcher through our regularly scheduled meetings. The collaborative efforts of the entire Pfizer team: Yansheng Wei, Dennis Gessmann, Constance S. Wood, Bryan A. Bernat, Teresa E. Pugh, Lauren Palmer-Jones, Ronan P. Cosquer, and Eric Dybeck has resulted in the culmination of two separate manuscripts.

While mom has been battling a less than ideal health situation for years, on Thanksgiving of November 2021, things, unfortunately, took a drastic turn for the worst. Thankful for the medical teams' expertise at Vanderbilt Medical Hospital for saving her life, turning a dire situation around, and providing my mother with the best quality of life given the circumstances. The recovery process has been slow, but grateful that I am able to share this achievement with her. This accomplishment means the most to her. It is because of my mother that I was able to attend and complete university debt free. More often than not my mother is sacrificial beyond what is appropriate. Thank you MOM. Thank you Dad for leading by example and showing up each day. Showing up even on the days its not easy. Thank you to my siblings. My life long partner in crime, my younger sister Sarah, someone I admire for her dedication, always putting her entire heart and self into everything she does. My younger brothers, James and Matthew, always pushing me to be the best version of myself. Last but not least, my youngest sister Sephora, for always reminding me to be silly, to take time to be in the moment, and enjoy life.

Showing up early, as I like to do, but one person was missing at the start time of our masters program day one orientation. We waited. 15 minutes later walks in Jennifer Michelle Quinde Zlibut, and since then I have never been early to anything again. Seven years later, I continue to grow in love with you more and more each day. Today and forever, I am happy to be spending the rest of my life with you. I am a better man because of you. I admire your dedication and passion for everything you do, compassion towards others, and especially your genuine Thank you Jen for always reminding me what matters most in life. Thank you to the Quinde family for your kindness and generosity that you have shown Jennifer and I throughout this process. From day one of meeting me, having not even started graduate school yet, ”Dr. Emanuel,” she would call me. As someone who has always struggle with self-doubt and self-deprecating tendencies, thank you Bertha Quinde for always speaking that over me. Barely knowing me, you believed in me even when I did not believe in myself. It is such a silly thing, but sometimes it is the small things that mean the most.

Thank you to the higher powers for these special people, for health, and the wisdom to achieve everything I have thus far in life.

TABLE OF CONTENTS

LIST OF TABLES

LIST OF FIGURES

CHAPTER 1

Overview of Metabolomics and Ion Mobility[1]

1.1 Overview of Metabolomics and Ion Mobility

Metabolomics includes the broad scale study of small molecules within cells, biofluids, tissues, and organisms. [1, 2] Metabolomics, which remains a growing field, has become a cornerstone of systems biology because of the unique insights it provides that are not directly obtained with other omics methods. Metabolomics encompasses the study of all substrates and products of the metabolic processes that are impacted by both genetic and environmental factors.[3] Therefore, the metabolome contains downstream biochemical products of the genome, proteome, and transcriptome, providing direct and real-time understanding into the state of the system under investigation. Primary metabolites are directly involved in growth, development, and reproduction, while secondary metabolites are only cursorily associated with these process.[4] The role of secondary metabolites in an organism can vary significantly from having no known influence on an organism's state, to altering its long-term survivability and expressivity. Human exposure to secondary metabolites produced by other organisms includes medicines, toxins, food additives (flavorings, stabilizers, etc.), cosmetics, pigments and dyes, and recreational drugs.

Because metabolites are fundamentally different from proteins (i.e., not biopolymers with repeating structural motifs), techniques widely implemented in the field of proteomics (.e.g,, enzymatic digestion, tandem MS fingerprinting, predictive databases) are not easily transferrable to metabolomics. Nuclear magnetic resonance spectroscopy (NMR) and mass spectrometry (MS) techniques are predominantly used to detect and identify metabolites.[5] These tools can be used either independently or in combination with additional methods, depending on the goals of the investigation. Liquid chromatography coupled to MS (LC-MS), for example, has become an increasingly popular platform to perform broad untargeted metabolomic analyses. LC-MS provides high peak capacity necessary to resolve and detect a large number of signals, or features, from biological samples. An untargeted metabolomics MS experiment can easily yield more than 25,000 detected features.[6] For complete analysis in a single experiment, high-resolution MS in combination with chromatographicseparation and tandem mass spectrometry (MSn, where n is the number of mass isolation stages used) has become a vital tool for successful annotation and relative quantification of the metabolome. LC is capable of separating molecules in solution-phase before ionization for m/z measurement, while MS^2 fragmentation data serves as a unique molecular fingerprint for identification.

---

[1] Parts of this chapter have been adapted from "Ion Mobility-Mass Spectrometry in Metabolomics Studies", published in *The Royal Society of Chemistry* and has been reproduced with the permission of the publisher

Implementation of ion mobility spectrometry (IM) into an already powerful analytical LC-MS technique further increases the peak capacity and provides an additional molecular descriptor to bolster identification confidence. In an IM experiment, analyte ions formed during the ionization step travel through an inert buffer gas under the influence of an electric field. Depending on the IM method used, ions are separated either temporally along the same transmission path or spatially filtered into different, mobility-selective trajectories.[7] IM techniques featured in this chapter include: drift tube IM (DTIM), traveling wave IM (TWIM), structures for lossless ion manipulations (SLIM), cyclic IM (cIM), trapped IM spectrometry (TIMS), and differential mobility spectrometry (DMS). In-depth descriptions of each IM technique are provided in a recent IM review.[8]

Several metrics are commonly used by the IM field to quantify analytical separation performance, most notably resolving power (R_p, single peak) and resolution (R_{p-p}, two peak separation). R_p is commonly used in MS as a measurement of instrument capabilities, whereas R_{p-p} is often utilized in chromatography, aptly illustrating the role that IM has played in bridging the performances of these two separation techniques.[9] Although drift time is the primary measurement of time-dispersive IM, is the measured arrival times are commonly converted into gas-phase collision cross section (CCS) values either through a fundamental relationship based on the kinetic theory of gases (i.e. the Mason-Schamp equation) as with DTIM, or through various calibration procedures either based upon prior CCS measurements or CCS values derived from models.[10, 11, 12, 13, 14, 15] CCS values, which are in part a representation of the size and shape of the analyte, incorporate the rotationally averaged cross sectional area of ions as well as interactions between the ion and drift gas during transit through the IM region. Thus, the measured CCS is a composite of both ion structure, but also the composition of the drift gas used for the measurement, such that CCS values are specific to the ion form and the drift gas in which the measurement was obtained.[16, 17] IM experimental parameters necessary to achieve highly reproducible CCS measurements within the range incorporating metabolites have been evaluated under various conditions.[16] As a normalized measurement of gas phase dimensions under given experimental conditions, CCS provides a common basis for comparison across different IM platforms.[18] IM can be readily integrated into current MS-based metabolomics workflows to enhance the detection and identification of metabolites, particularly through four application areas, discussed below, which include: (1) signal filtering by reducing MS spectral complexity, (2) isomer separation, (3) metabolomic annotations, and (4) gas-phase IM structural analysis.

1.2 Signal Filtering

Metabolomics experiments measure expansive chemical classes, each with unique molecular properties. A major focus of IM is minimizing the complexity of mass spectral data by reducing the background ion signals relative to the ions of interest. In particular, IM is capable of partitioning the ion signal into different spectral regions, which in turn can address isobaric spectral overlap. Mass isobars, which are convoluted ion signals with similar mass measurements (but not necessarily isomers), pose a challenge to MS based techniques because they are unresolved by MS alone. While the vast majority of IM metabolomics experiments utilize the IM dimension to help filter out concomitant chemical noise to varying degrees, DMS is particularly well-suited for mobility filtering functionality. DMS is a spatially-dispersive IM technique, which in a specific geometry is also known as field-asymmetric wave form ion mobility spectrometry (FAIMS), is particularly advantageous for targeted metabolomics applications where high sensitivity is desired. DMS operates at ambient pressure, and, unlike many other IM techniques, can be coupled to existing MS instruments with minimal modification. Ions which are transmitted by a DMS device are distinguished by differences between mobilities at high and low electric fields, exploiting the dependence of an ion's mobility value on the applied field strength. Thus, DMS separates ions based on a slightly different principle than most other IM techniques, namely the change in the gas-phase mobility, which can be tailored to improve the selectivity for specific analytes. Vouros and colleagues demonstrated enhanced detection of targeted drug metabolites, such as benzoylecgonine (a major metabolite of cocaine), from background biological matrices before MS analysis.[19] Using DMS as a signal filter resulted in elimination of urine matrix background including the removal of m/z signals closely overlapping with protonated benzoylecgonine (m/z 290).

Incompatible with chromatographic separations, ambient ionization imaging techniques like desorption electrospray ionization (DESI) are profoundly aided by DMS filtering capabilities. The Fernández group reported signal-to-noise (ratio (S/N) improvements between 70 - 190% during DESI-DMS-MS analysis of metabolomic pharmaceuticals and low m/z isobaric chemicals.[20] Additionally, by optimizing the FAIMS compensation field, Feider and coworkers demonstrated improved detection and imaging of molecular species' subsets in biological tissues.[21] Through optimization, improved S/N can be achieved for small metabolites, fatty acids, and phospholipids with minimal to no detection of larger ions (high concentrations of biological material are separated/filtered away). DMS and FAIMS have been used for selective high-throughput monitoring of biomarkers in urine, rapid metabolic analysis of complex dried blood spots, and breast cancer diagnosis through tissue metabolic profiling.[22, 23, 24] Results support DMS and FAIMS as fast alternatives to enhance metabolomic detection sensitivity and selectivity. In addition, while not differentiation between background and analyte of interest, recently, McKenna and coworkers demonstrated the use of TWIM and DTIM for distinguishing between carbohydrate isobars with 95% confidence.[25]

1.3 Isomers in Metabolomics

Isomers are molecules that share the same chemical formula and m/z but differ in how their atomic compositions are arranged. These differences are comprised of either structural (differing connectivity between atoms), or spatial (similar bond connectivity but distinct geometries) divergence. Some examples of isomerism include constitutional, rotational, diastereomers and enantiomers. Because of the vast number of metabolites that share a chemical formula within a limited m/z window (approximately 0 – 3000 m/z), isomers are very prevalent in metabolomics and often require additional separation for differentiating which isomer a particular signal corresponds to.

Prior to mass spectrometry analysis, the molecules under consideration must first be ionized, and for metabolites, this yields almost exclusively a singly-charged ion. In the most common ionization techniques used, namely electrospray ionization (ESI) and matrix assisted laser desorption ionization (MALDI), ionization is routinely conducted in the positive ion mode and yields an $[M+H]^+$ ion whereby the molecule is ionized by the addition of a proton, generally at the most basic region of the gas-phase molecule. However, many small molecules possess multiple potential protonation sites and, as a consequence, the possibility of protonation site isomers ('protomers') forming during the ionization step. Since the m/z values are identical, protomers cannot be distinguished with high-resolution mass spectrometry alone. Whereas, a single unique drift time is most often observed in IM experiments for small molecules, sometimes IM analysis of small molecules can occasionally exhibit multiple drift times some of which are a result of the molecule ionizing at varying protonation sites.[26] Both the ionization technique and specific source conditions have been demonstrated to influence abundance ratios between these generated protomers.[27] When considering protomers, multiple drift times for a single ion mass can suggest the presence of more than a single gas-phase molecular conformation or, if molecular geometry remains unaffected, differences in electrostatic interaction between the mobility buffer gas and each 'fixed' protomer. One of many possible examples is shown in Figure 10.1(a), which illustrates a TWIM-MS spectrum of protonated aniline (m/z 94.07) formed via positive mode ESI with two well-resolved peaks, each attributed to a unique site of protonation. Even though these gas-phase structures differ only in their site of protonation, a peak (apex-to-apex) separation in IM by 1.17 ms is observed.[28] While it might seem the position of a single proton should have a subtle effect on the molecule, this variation can result in distinct CCS values for a number of metabolites. A difference greater than 10 $Å^2$ (approximately 7% difference) was observed by the Lemière and Sobott labs while varying the protonation site for atomistic models of melphalan.[29] Hercules and coworkers, while characterizing 3- and 4- ring methylenedianiline isomers using IM-MS, also demonstrated that protonation sites influence the the mobility of gas-phase ions to a measurable degree. Differences of almost 20 $Å^2$ have been observed when exploring protonation site modifications of atomistic models.[30, 31] Many primary metabolites contain molecular scaffolds that exhibit multiple possible sites of protonation (e.g., aniline, phenol, hydroxypyridine) and thus might be expected to exhibit protomers which would remain unresolved by MS alone, but can be uniquely addressed through the inclusion of IM analyses. Depending on the application, MS protomer studies may serve as a useful tool for characterizing chemical stability and reactivity of molecules.[32] However, protomer formation is a consequence of the ionization stage necessary for the analytical measurement, and the presence of multiple drift times for a single molecule increases spectral complexity and exacerbates MS spectral interpretation difficulty. This complexity has not yet been a major concern with lower IM resolution capabilities, because protomers may not be completely resolved, but instead contribute to broad peaks or peak features such as the presence of unresolved shoulders.[33, 34] Nonetheless, with higher IM resolution capabilities as anticipated with the next generation of IM platforms, the resolution of protomers may become more common, requiring additional considerations for IM data interpretation.

For stereoisomers, ‘R’ and ‘S’, D and L, or ‘+’ and ‘-‘ are used to note specific molecular conformations, specify chiral orientation, or optical rotation, respectively. Stereoisomer detection is important, because even with only minor structural changes, the chemical and biological activities of isomers can differ drastically.[35] For example, L-3,4-dihydroxyphenylalanine (L-DOPA) is the most commonly used therapeutic agent for Parkinson’s disease, while its enantiomer, D-DOPA, has no clinical effect without metabolic conversion into L-DOPA.[36] Drastic differences in the bioactivity of enantiomers have also been implicated in one of the largest human caused medical disasters in history. In the 1960s, R-thalidomide was heavily prescribed for the successful treatment of morning sickness in pregnant women. Subsequently, thousands of children across Europe and Asia were born with varying degrees of incurable malformities.[37] This was later linked to the presence of a enantiomer, S-thalidomide, in the prescribed medication. While R-thalidomide has shown effectiveness in treating morning sickness, its enantiomer, S-thalidomide, was discovered to be teratogenic. Today, enantiopure R-thalidomide is used successfully to treat a range of conditions, including multiple myeloma and complications of leprosy.[38] Optically pure compounds are suitable for increasing potency, reducing toxicity, and yielding only the desired therapeutic effects. However, the structural similarities of enantiomers can make them quite challenging to detect, and even more challenging to separate. Uniquely suited for isomer detection, IM-MS investigations have included both endogenous and exogenous isomeric metabolites.[39, 40, 41] However, IM enantiomer separation and detection still remains challenging at present resolving powers. In an investigation of 11 leucine isomers sharing the same molecular formula ($C_6H_{13}NO_2$), DTIM-MS provided sufficient resolution to separate mixtures of constitutional isomers (differences in bond connectivity), but exhibited limited separation for enantiomers (same bond connectivity, but different three-dimensional shape) for $[M+H]^+$ ions.[42] For $[M+H]^+$ leucine enantiomers, the authors predicted that an IM resolving power in excess of 2000 would be necessary to completely resolve all combinations of leucine/isoleucine enantiomers investigated in the study.

The importance for chiral separation techniques is pervasive due to the existence and use of enantiomers in a broad range of applications involving drug development for pharmaceutical, agricultural, and food industries.[43] Thus, there is a long-standing and growing interest in the advancement of efficient and reliable chiral analysis methods that assist with production and quality control of chiral drugs. The majority of successful enantiomer separations and detection has primarily been achieved with chiral chromatography and capillary electrophoresis methods.[44, 45] However, the pursuit of faster and more sensitive analytical techniques for quantitative chiral measurements has led to the development of MS-based approaches.[46, 47, 48] While MS is a highly selective technique for identifying analytes with different molecular formulas, techniques in addition to MS are required for identifications of isomers. Successful implementation of MS^2 for enantiomer quantitation was developed by Cooks and coworkers in a technique called the kinetic method.[49, 50, 51] Detection and quantification of enantiomeric excess of α-hydroxy acids, amino acids, atenolol, DOPA, ephedrine, pseudoephedrine, isoproterenol, norepinephrine, and propanol drug mixtures were measured with samples containing less than 5% enantiomeric contamination utilizing various coordination metals and chiral selectors.[52, 49, 53, 54] IM provides a complementary tool for separation of isomers by utilizing differences in mobility to resolve analytes. However, because of the structural similarity of metabolomic enantiomers and the limited resolving powers of first-generation IM instrumentation, it has remained difficult to distinguish enantiomeric species.[55] This may lead to low-confidence identifications of components in complex samples. Enhanced ion mobility separation has been achieved in isomeric species, including enantiomers, by (1) doping samples with various metals in combination with chiral selectors, (2) modifying the experimental conditions of DTIM-MS and TWIM-MS instruments, and (3) the use of trapped, cyclic, SLIM, and HRdm high-resolution IM-MS instruments and techniques.[56, 57, 58, 59, 60, 61, 62, 63, 9, 64, 65, 66, 67, 68, 69]

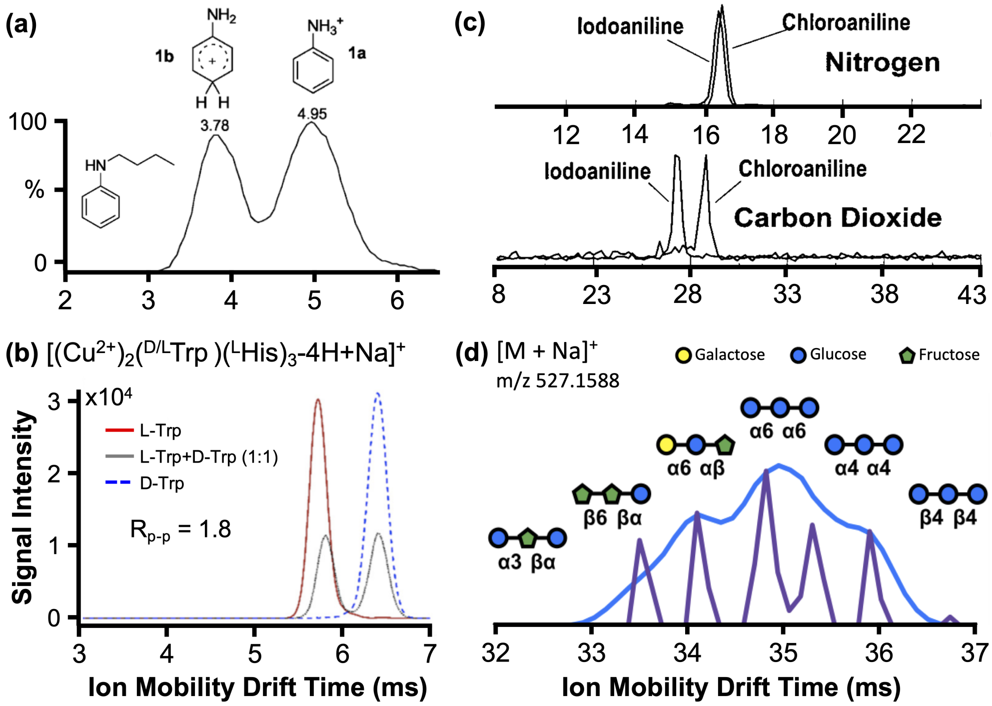

Figure 1.1: Small molecule IM-MS separation.

(a) ESI-TWIM-MS drift time spectra of n-butyl aniline protomers (m/z 94.07). Reproduced/Adapted from Ref. 24 with permission from **Journal of Mass Spectrometry, Copyright 2012.** (b) IM spectra of $[(Cu^{+2})_2(^{D/L}Trp)_3(LHis)_3 - 4H + Na]^+$ with enantiomer analyte concentrations of 10 μM. Reproduced/Adapted from Ref. 53 with permission from **Analytica Chimica Acta, Copyright 2017.** (c)IM spectra of choroaniline and iodoaniline with nitrogen and carbon dioxide drift gas. Reproduced/Adapted from Ref. 66 with permission from **American Chemical Society, Copyright 2006.** (d) Trisaccharide isomeric mixture obtained under standard demultiplexing (Blue) and HRdm (Purple) Reproduced/Adapted from Ref. 75 with permission from **American Chemical Society, Copyright 2020.**

1.3.1 Isomer-Selective Sample Additives

For enantiomers with the same mass-to-charge ratio (m/z), IM distinction is based on differences in their CCS values, which are in part contingent on the ion size and shape. Metal coordination complexes can, in some cases, exaggerate minor stereoselective structural variance, in comparison to smaller, more conventional $[M+H]^+$ and $[M-H]^-$ ion forms, resulting in larger CCS differences and thus more significant isomer discrimination. Adopted from the kinetic method, metal complexes continue to be investigated for IM recognition including, amino acid and glycan isomers.[56, 57, 58, 59, 60, 61] As shown in Figure 10.1(b), tryptophan (Trp) complexes formed using Cu^{+2} metal with histidine chiral selectors provided significant separation for D- and L-Trp.[61] As is the case for D- and L-Trp and all tested amino acids, when the selector molecule possessed L-chirality (in this case L-His), the resulting L-amino acid complexes exhibited smaller CCS values than their D- counterparts, signifying the importance of the selector chirality in forming a stereoselective complex. Specifically, L-amino acids are able to form a more compact gas-phase complex in the presence of an L-chiral selector, which is likely due to steric hindrance. Work from Yao and coworkers demonstrated chirally-selective binuclear metal bound complexes, $[(Cu(II))_2(S/R-naproxen)(L-His)^2-3H]^+$, which enabled the effective identification of naproxen isomers with IM-MS.[70] Proposed structural candidates of these binuclear copper complexes were generated through quantum mechanical approaches. A structural understanding of these chirally-selective complexes will enable such interactions to be predicted prior to screening them through trial and error, and may lead to more generalized strategies that are more amendable for untargeted metabolomic analyses using IM-MS.

1.3.2 Ion Mobility Strategies

Traditionally, IM analysis is performed with either helium or nitrogen drift gas. One motivation for utilizing helium is its low polarizability - a property that minimizes more complex long-range interactions between ions and the drift gas during the IM experiment.[18] Made common through widespread use in TWIM instruments, nitrogen gas is readily available and has shown to provide high resolving power across a wide range of m/z with high CCS reproducibility.[71, 16] However, dependent on the analyte of interest, modification of the drift gas conditions has demonstrated potential to enhance the separation of isomers, including amino acids, drug molecules, monosaccharide methyl glycosides, and disaccharides.[62, 63, 9] Investigated modifications include (1) using more polarizable drift gases such as CO2, (2) conducting the IM analysis at atmospheric pressure, and (3) doping the drift gas with gas-phase modifiers.[62, 72, 73, 74, 9, 75, 63] In Figure 10.1(c), chloroaniline and iodoaniline were used to demonstrated the effects of varying the drift gas composition on IM separations. With nitrogen as the drift gas, chloroaniline and iodoaniline have nearly identical drift times, however, they are separated when CO_2 is used.[75] These findings reported by Asbury and coworkers suggest that both size and polarizability of the drift gas alter an ion's mobility through the drift region. Similarly, CO_2 was utilized by Fasciotti and coworkers for successful separation of lactose and maltose isomers.[63] While the use of alternative drift gases and gas modifiers has not been extensively explored, these strategies show promise for improving IM resolution without significant hardware modifications.

1.3.3 Next Generation Ion Mobility Instrumentation

Methods for enhancing IM resolution without hardware modifications have extended the isomer separation capabilities of IM instruments now considered to be lower resolution IM-MS platforms (those typically performing with less than R_p 100). However, new commercial IM offerings have made significant improvements in IM resolving power. In particular, TIMS, cIM-based instrumentation, high resolution IM based on SLIM, and high resolution demultiplexing (HRdm) have extended the accessible R_p of IM to greater than 100, and these strategies are discussed below. Following introduction by Park and co-workers in 2011, TIMS has primarily been used for proteomic studies, but explorations have included monitoring (detection, separation, and quantification) of common polychlorinated biphenyl and lipid isomers in human plasma.[76, 77, 78] Additional expansion of TIMS applications has included development of a plant metabolomics TIMS CCS library, and implementation in combination with MALDI imaging techniques to enhance spectral quality and coverage by improved isobar and isomer separations.[79, 80] Spraggins and coworkers observed four components well separated via IM from a single feature with m/z 267.956 while imaging entire kidney sections. Following the seminal description and development by the Smith group, SLIM-IM has been used to differentiate peptide, sugar, and amino acid isomers that are indistinguishable by mass and remained problematic to study using first generation IM platforms.[65, 68, 69] Although the long path-length structures (e.g., 13 meter) utilized in high resolution SLIM-IM necessitates longer experimental collection times on the order of seconds, SLIM-IM separation capabilities have surpassed first-generation IM resolving powers while providing additional experimental versatility. Similarly, cyclic geometry TWIM (cIM) instrumentation capable of performing multi-pass IM experiments to enhance resolution has demonstrated improved separation of isobaric ribonucleotide variants and carbohydrate isomers.[64, 66, 67] In addition to hardware approaches, a recently-described software approach to achieve enhanced IM resolving powers, referred to as high resolution demultiplexing (HRdm), was demonstrated to enhance the separation capabilities of a first generation IM instrument. This work has prioritized multiplexing strategies and post-acquisition data processing improvements over hardware modifications, but conceptually can also be used in combination with higher resolving power hardware as well. May and co-workers demonstrated a 2- to 3- fold improvement in resolving power when compared with conventional DTIM when differentiating monoglyceride positional isomers.[81] Shown in Figure 10.1(d) is a trisaccharide isomeric sample analyzed on a DTIM instrument using standard demultiplexing (shown in blue) and HRdm (shown in purple) software protocols. Whereas standard demultiplexed IM yielded a broad, unresolved peak for the isomeric mixture, the HRdm analysis resolved 5 peaks. HRdm is unique in that it allows for improved resolution while operating at relatively faster speeds in comparison to next generation instrumentation.

1.4 Metabolite Identifications

Metabolite annotations are important in linking experimental data with meaningful biological information. Original guidelines for communicating confidence in identifications were published by the chemical analysis working group (CAWG) in 2007.[82] These guidelines consist of a five level system utilizing multidimensional analysis to achieve the broadest metabolome coverage, as well as prescribing minimum data requirements for confident identifications. The highest confidence level are validated identifications (Level 1), and they require confirmation by two orthogonal properties, such as MS^2 or LC, obtained from a pure reference standard using an independent experiment with indistinguishable conditions. In the absence of a reference standard, predictive or external diagnosis with similar instrument configuration (matches of m/z and either MS^2 or LC), would be considered putative identifications (Level 2). Tentative identifications (Level 3) match only a precursor ion m/z to a metabolite database. Molecular formula candidates (Level 4) corresponding to a unique experimental m/z (Level 5) are low confidence annotation classifications.[83] In some cases, the identifications confidence level can depend on instrument performance, specifically resolving power and accuracy. A higher resolving power and increased measurement accuracy leads to higher confidence levels by minimizing isobaric interference and the scope of possible identifications. At the time CAWG developed its five level confidence system, IM was still an emerging analytical technique, and as such, CCS measurements were not included in the original guidelines for metabolite annotations. CCS was later adopted as an orthogonal measurement to support metabolite identification following the efforts that demonstrated its utility in differentiating between biochemical classes.[18] Ion mobility workflows implementing standardized protocols have yielded highly reproducible CCS values across multiple platforms and laboratories, framing IM-MS as suitable for metabolomics annotations. When standardized protocols are implemented, CCS values exhibit relative standard deviation (RSD) of better than 3% across different instrumental platforms and much better when comparing results obtained across similar instruments.[84, 85]

Bearing in mind the vast size of the metabolome and complexity of MS spectra, metabolite databases have been established to assist with feature identification thereby reducing the need for individual laboratories to obtain reference standards. METLIN (METabolite LINk), the first MS-based metabolite database, was developed by the Scripps Research Institute and currently includes over 500,000 metabolite entries with both m/z and MS^2.[86, 87] To date, the most comprehensive database of endogenous metabolites is the human metabolome database (HMDB), which reports m/z, MS^2, and LC retention times for more than 144,000 metabolite entries, specific to human biology.[88, 89] Between these two databases, a vast number of known molecular classes are encompassed, including small organic acids, amino acids, sugars, nucleotide, nucleosides, carbohydrates, sugar phosphates, drugs, vitamins, lipids, and short chain peptides. Implementation of METLIN and HMDB databases have facilitated the ability of metabolomics to guide systems biology data interpretation through unknown characterizations. The utility of IM for metabolite annotations has remained limited by the availability of reference CCS values for comparison. As CCS has been more widely accepted and implemented for metabolite annotations, progress has been made towards expanding metabolomics databases to include metabolite CCS values.

A number of laboratories have generated independent CCS databases inclusive of small molecules encompassing drugs, lipids, both primary and secondary metabolites, and natural products.[90, 91, 92, 93, 94, 41, 95] It's important to note that CCS values are not solely a property of the molecules themselves but also dependent on the internal conformational energy, charge state of the analyte, the specific ion form, and its interaction with the specific mobility gas. As these CCS databases efforts span a wide range of instrumentation, techniques, and different mobility gases, researchers have also explored the curation of libraries incorporating CCS values into a single compendium. As such, recommendations on nomenclature have been introduced including the method type as a superscript and the drift gas used as a subscript (e.g. $^{DT}CCS_{He}$ and $^{TW}CCS_{N2}$).[96] Recently, standard CCS databases have been established for a variety of chemical classes on both DTIM (approximately 3800 entries) and TWIM (approximately 7300 entries) platforms with standardized protocols for CCS contribution to the databases by the broader community.[97, 17, 98] Figure 10.2(a) is the DTIM-based Unified CCS Compendium interface depicting measured CCS classified by super class established by the McLean research group. Figures 10.2(b-c) represent the RSD of all measurements binned by CCS/z and the distribution of ions contained in the database as a function of m/z, respectively. Duplicate measurements were highly reproducible with the global RSD of included CCS measurements being 0.025% with a minimum inclusion threshold of 0.7%. Due to the immensity of chemical space represented by the metabolome and the limited number of unique reference standards available, it is currently intractable to populate a fully comprehensive metabolite CCS database with empirical data. To bridge these efforts, theory driven modeling, deep neural networks, and classical machine learning methods have been utilized to predict CCS values and provide CCS entries for compounds that do not have an experimental CCS. A key step towards the implementation of CCS as a broad metabolite identifier hinges on the prediction of high quality CCS values. Both DTIM and TWIM CCS databases have been used as training sets for machine learning to expand metabolite annotation capabilities.[99, 17, 100, 101, 102]

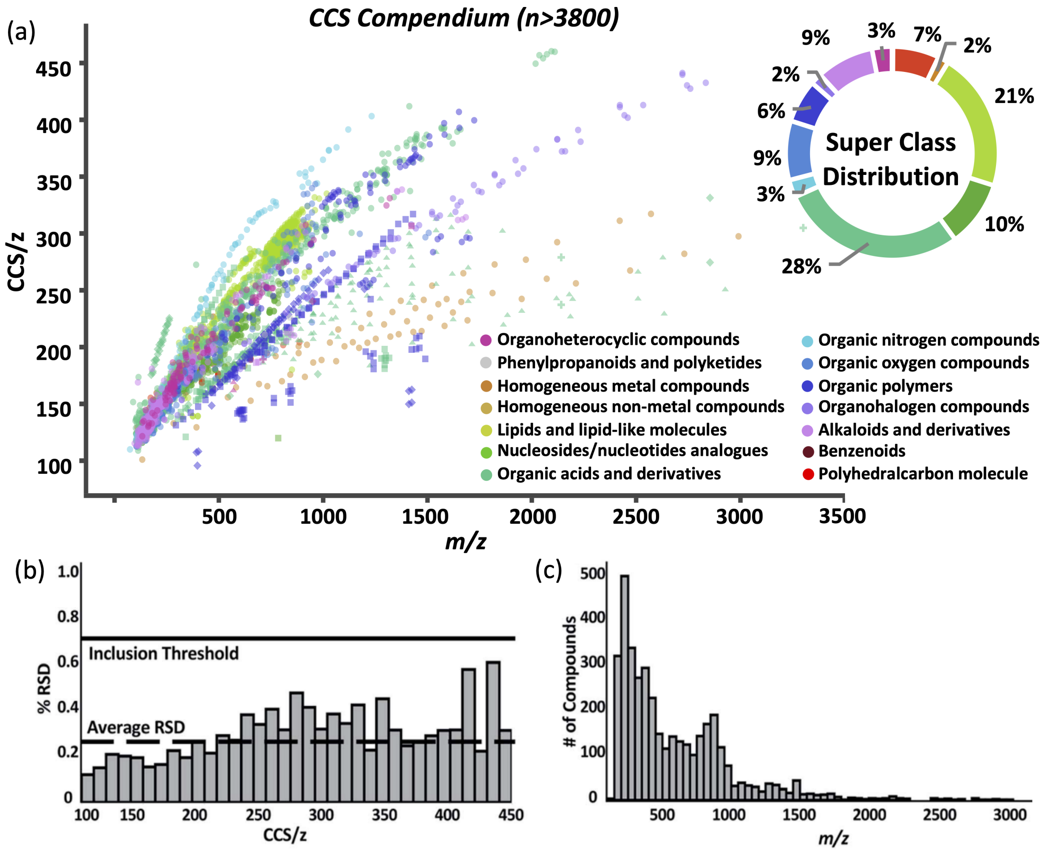

Figure 1.2: CCS compendium.

(a) Compendium interface depicting measured data points classified by superclass with distributions across 14 super class (b) RSD of all measurements binned by CCS/z and (c) m/z distribution of ions contained in database. Reproduced/Adapted from Ref. 91 with permission from **Royal Society of Chemistry, Copyright 2019.**

1.5 IM Structural Analysis

Although the measured CCS is in part representative of the structure of the analyte, these measurements are considered “coarse-grained” and are not adequate by themselves to allow detailed structural interpretations. Like a silhouette conveys the outline of a shape, CCS provide general information of molecular structure, but lack specificity. To better understand the conformations and shapes adopted by ions in the gas-phase, the experimentally-derived CCS values can be compared to computationally-established atomistic models. A simplified schematic of this concept is presented in Figure 10.3(a). The main challenges associated with the structural interpretation of IM data are (1) developing reliable atomistic models and (2) obtaining theoretical CCS values which correspond to these computationally-derived models.

1.5.1 Atomistic Modeling Methods

To date, an immense number of computational approaches exist for the purpose of achieving reliable atomistic models. Atomistic models, as their name suggests, include a wide range of computational approaches that account for individual atoms in complex systems. Atomistic modeling approaches include quantum mechanical (QM), ab initio or semi-empirical, and classical methods. QM methods provide a high degree of accuracy, but are computationally-intensive and the calculation complexity scales exponentially with molecular size. Hartree-Fock (HF) theory is one type of QM method which leverages the many-body wavefunction to approximate electron-electron interactions to solve structural questions.[103] However, as highlighted by Moncrieff and Wilson, a lower convergence accuracy agreement is observed with HF for negatively charged species than for neutral or positively charged species.[104] Another QM method commonly implemented for small molecules is density functional theory (DFT), which is used to investigate electronic or nuclear structures of many-body systems and, unlike HF theory, uses electron density rather than wave function as the fundamental property.[105, 106] While ab initio methods precisely reproduce accurate geometries, they are not economical for molecules larger than a few atoms. Semi-empirical methods are built on HF theory, and improve speed and accuracy by excluding or parameterizing equations with empirical data such as ionization energy or dipole moment.[107] Semi-empirical methods have been used for larger systems incorporating metals, such as stereospecific metal complexes of L- and D-DOPA isomers.[108, 109] So-called classical methods including Monte Carlo and molecular dynamics (MD) are most widely used for atomic-level modelling. Monte Carlo methods model complex systems by estimating unknown parameters through repetitive random sampling, providing a collection of representative conformations. MD investigates time-dependent development of molecular structure.[110] Researchers studying systems of multiple particles often use the Monte Carlo method in conjunction with MD to first establish placement and velocities of particles and then calculate their momentum at a later time. Generally, the size of the system being studied is an important component in determining the method used, but is defined by the preference as well as computational capabilities at the disposal of the user. In addition, theoretical investigations have concluded that ionized small molecules require careful attention with appropriate selection of charge placement.[29, 26] With the numerous options available, a good working knowledge of the field of computational chemistry is required to obtain reliable atomistic models.

1.5.2 Theoretical CCS Determination

Once atomistic models have been appropriately generated, several CCS calculation models can be applied to these theoretical structures, which generally involve simulation of the collisions between the buffer gas and varying structural orientations of the atomistic model. The projection approximation (PA), exact hard sphere scattering (EHSS), diffuse hard sphere scattering (DHSS), trajectory method (TM), and the projected superposition approximation (PSA) are broadly-recognized, currently-used algorithms which determine a corresponding CCS value or suite of values from a theoretical chemical structure. Differences between each CCS algorithm stem from a compromise between physical thoroughness and computational expense, resultant of their fundamental assumptions. Depicted in Figure 10.3(b), TM is considered to be the most thorough but also most time intensive because it explicitly accounts for both long-range and short-range interactions as well as numerous scattering events.[111, 112, 113] Slightly more streamlined, EHSS disregards long-range interactions and takes into consideration only hard-sphere collisions (Figure 10.3(c)).[114] This is based on the assumption that long-range interactions become less prominent for larger molecules. Depicted in Figure 10.3(d), PA does not account for either long-range interactions or scattering events, but rather with the understanding that CCS is a rotationally averaged cross-sectional area, PA determines CCS using a hit-or-miss model of varying ion projections. PA requires no integration of probe trajectories and is considerably faster than the other methods.[115] Finally, PSA utilizes an optimized PA algorithm and applies an additional weighting factor based on a surface area approximation of the theoretical atomistic structure. Optimization of these algorithms have been reported while several new algorithms have also been proposed.[116, 117, 118, 119, 120] For appropriate parametrization of CCS calculations the user must consider the type and size of the system as well as the experimental conditions the theoretical workflow is designed to parallel. For a minimally-polarizable drift gas such as helium, interactions between the analyte and buffer gas would be minimal. Therefore, at a much lower computation cost in comparison to alternative methods, PA may be sufficient to use for helium CCS calculations but not for nitrogen. However, because the influence of electronic interactions are much more prominent in small molecules than in larger systems, TM may be best suited for metabolite studies.

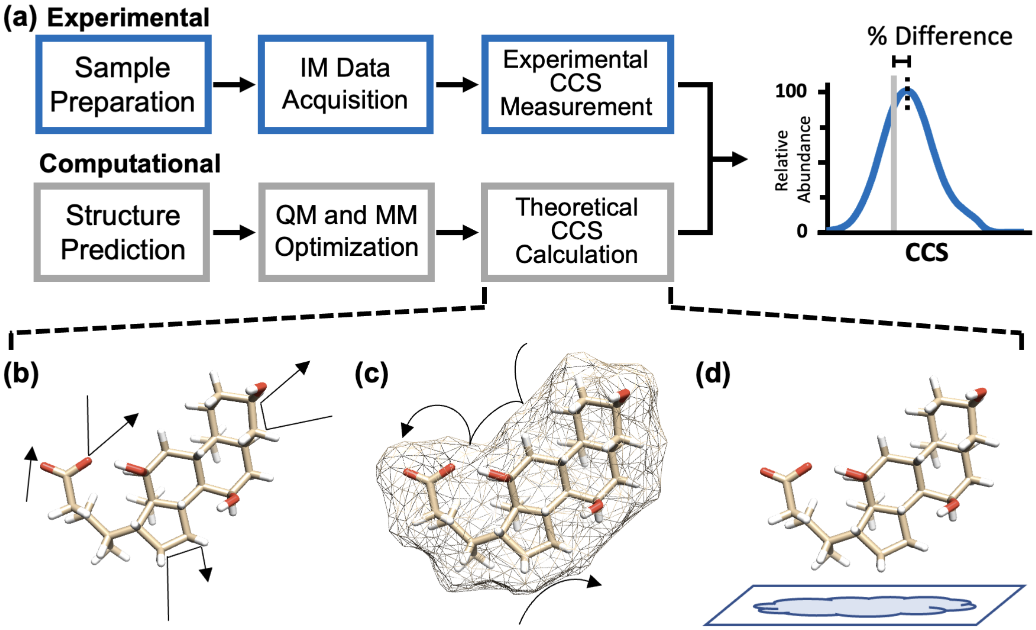

Figure 1.3: Theoretical modeling schematic.

(a) Schematic of the junction between experimental workflow and theoretical methods. Graphics of theoretical protocols for CCS determination: (b) trajectory method, (c) exact hard sphere scattering, (d) projected approximation.

1.5.3 Applied Theoretical Analysis

An in-depth study describing the current standing of theoretical strategies in combination with IM-MS recently has been published by Allison and coworkers.[121] Although the focus is on macromolecules, many of the challenges and considerations discussed are also relevant for small molecules. With proper parameterization and optimization, deviation between theoretically and empirically derived CCS values for small molecules can be less than 3%.[122] Atomistic models have been used to support IM-MS observations by (1) providing insight on possible protonation site isomers ('protomers', introduced in Section 10.3), (2) visualizing structural features which give rise to isomer separation (Section 10.3), (3) yielding additional information on molecular folding and sequence, and (4) exploring the structure of ion complexes formed between metabolites and metals.[123, 124, 125, 40, 126]

Computational workflows have expanded the structural understanding of gas-phase isomer ions and electrostatic interactions. Diastereomers, dexamethasone and betamethasone, can reproducibly exhibit a small difference in their CCS values (differences of approximately 1 $\mathring{A}^2$), presented in Figure 10.4(a). Theoretical investigations by Kim and coworkers determined the observed CCS differences between betamethasone and dexamethasone were not a result of long-range charge induced dipole interaction, but of short-range Van der Waals interactions between the ions and drift gas during the IM experiment. [123] In another example, Figure 10.4(b) shows the structural representation of theoretical conformations and CCS distributions of protonated nonapeptide diastereomer L-vasopressin (VP). With 3000 theoretically derived conformations for both L-VP, two CCS distributions are denoted for L-VP whereas a single CCS distribution was observed for D-VP (not shown).[40] This two peak distribution for L-VP agrees with experimental observations. Theoretical sampling of conformational space provided evidence for two distinct gas-phase configurations for L-VP (folded and extended), whereas D-VP exclusively adopts a single extended conformation in the gas-phase. While not specifically probed in this report, the relative stabilities of these gas-phase conformations might be expected to exhibit some dependence on the energy of the experiment, specifically, as the ion temperature is increased, the peptide structure might exhibit measurable changes to the gas-phase CCS. In general, the primary structural differences of chiral isomers are minor and, particularly for small molecules, chirality may not be measurable via IM-MS without interventions such as chiral modifiers. Theoretical workflows can support the study of chiral small molecules via IM-MS by providing detailed electrostatic interaction information and structural insights. Through optimization, the structurally-selective capabilities of IM-MS holds promise to addressing the challenges associated with separating enantiomers in mixtures.

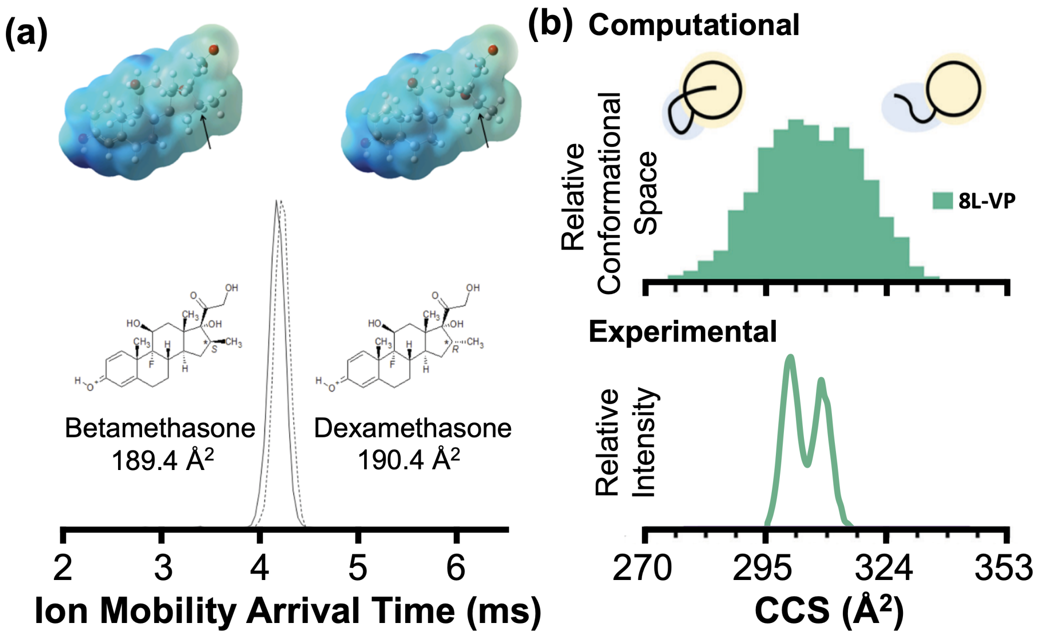

Figure 1.4: Small molecule modeling.

(a) Individual TWIM overlays of betamethasone (solid line) and dexamethasone (dotted line). Arrows indicate the chiral center on models. Reproduced/Adapted from Ref. 113 with permission from **American Chemical Society, Copyright 2011.** (b) IM of protonated L-vasopressin (below) and theoretical conformation distribution across calculated CCS values for L-vasopressin. Reproduced/Adapted from Ref. 36 with permission from textbfRoyal Society of Chemistry, Copyright 2018.

In addition to the $[M+H]^+$ ion form, metal-adducted ion species, such as $[M+Na]^+$ ions can also be observed in IM-MS metabolomics experiments. Sodium cation interactions with metabolites can significantly alter their gas-phase structure, which in turn yields different drift times and CCS values in IM experiments. Because the gas-phase conformations of sodium-coordinated metabolites are not well understood, Stow and colleagues developed a distance geometry protocol to sample the conformational space of 11 natural products and investigate their interactions with sodium cations. A single drift time was observed for the $[M+Na]^+$ ion form of each natural product, indicating one gas-phase conformation was adopted in response to sodium coordination. Based on computational results, it was determined that for the natural products studied, sodium cations typically coordinated with multiple hydroxyl and carboxyl groups simultaneously, leading to a compact gas-phase structure.[127] Importantly, this work avoided the potential of local energy minima that can be encountered with more traditional molecular dynamics approaches, because distance geometry methods are unbiased in their ability to sample all potential conformational space.[127] While the metabolites investigated in this work exhibited a narrow range of structures, in other instances, metabolite ions can adopt multiple gas-phase conformations, which manifest as multiple IM features at a common m/z. For example, theoretical results from the sodium-adducted 25-hydroxyvitamin D3 ion suggests that it has two energetically favorable gas-phase structures, which was in general agreement with experimental findings, suggesting this ion adopts both a closed (compact) and open (extended) conformation in the gas-phase.[128]

1.6 Applications in Metabolomics

Fundamental technique developments have been highlighted above on topics related to the progression of IM-MS utility for broadscale metabolomics studies. Hill and colleagues have presented elsewhere a general overview of the emerging applications of IM technology.[129] Emphasized below are studies on the forefront of metabolomics-specific research utilizing IM. IM has made continued contributions as a standalone system as well as in combination with MS platforms for metabolomics investigations.

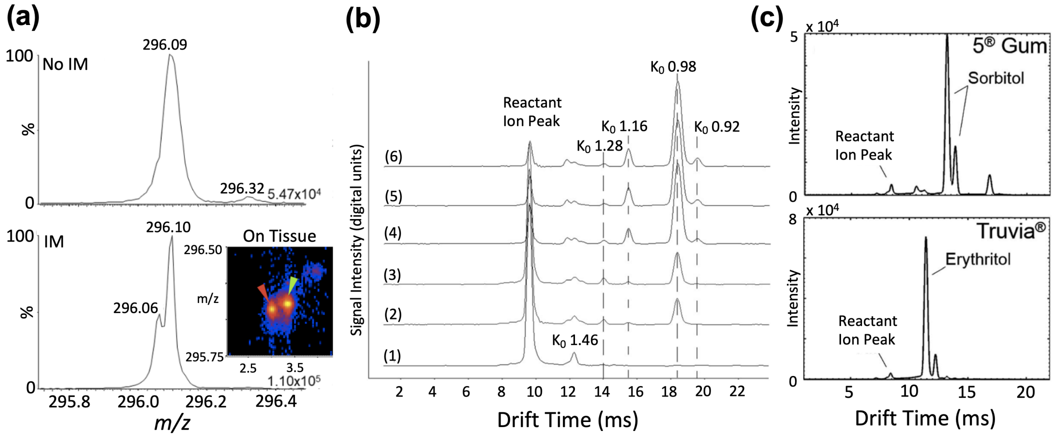

Figure 1.5: IM-MS clinical studies.

(a) Mass spectra acquired on tissue with and without IM demonstrating the separation of MBZ signal from an interfering ion. Reproduced/Adapted from Ref. 128 with permission from **American Chemical Society, Copyright 2020.** (b) (1) IM spectra of blank and benzoylfentanyl at (2) 8.4ng, (3) 42ng, (4) 84ng, (5) 168ng, and (6) 336ng. Reproduced/Adapted from Ref. 145 with permission from International Journal for Ion Mobility Spectrometry, Copyright 2019. (c) IM spectra of 5® gum and Truvia® natural sweetener. Reproduced/Adapted from Ref. 152 with permission from **Royal Society of Chemistry, Copyright 2016.**

1.6.1 IM-MS Imaging

Techniques commonly used for drug and metabolite distribution studies in animal tissues are generally considered costly and tedious, often requiring the use of radiolabels, adding complexity and sample handling safety considerations.[130] An alternative approach for spatially-resolved metabolomics is mass spectrometry imaging (MSI), which allows the simultaneous mapping of both spatial locations and relative abundances for numerous analyte ions originating from biological samples. The most commonly used ionization sources in MSI studies are MALDI, DESI, and laser ablation electrospray ionization (LAESI). The challenging task of imaging metabolites is to cover as much of the metabolome of interest as possible, ideally in a single experiment. Typically in MS-based metabolomics, LC-MS is utilized to maximize peak capacity and analyte coverage, however, online MSI is incompatible with conventional liquid chromatography, because of the sampling speeds required to generate the spatially-resolved maps of analyte coverage. As a post-ionization separation technique, IM separations are compatible with the timescales necessary for MSI, and can be utilized to enhance image quality, improve selectivity, and increase S/N by resolving isobaric interferences.[131, 132] Vertes and coworkers utilized LAESI combined with IM-MS to identify four species contributing to 1566.22 m/z while mapping untreated biological tissue.[133] Additionally, Caprioli and coworkers utilized MALDI-based MSI combined with IM-MS for differentiating between two lipids that shared the same m/z of 756.55.[134] Figure 10.5(a) shows the mass spectrum of mebendazole (MBZ) measured from tissue sample with and without IM. With no IM, the expected MBZ signal at m/z 296.10 is slightly shifted and appears to contain a shoulder because of an interfering ion at m/z 296.06. These two overlapping ions are more resolved when IM is used. Numerous additional laboratories have demonstrated the utility of IM to discriminate between biological background signal masking the low abundance signal of interest present in tissue samples.[135, 136, 137, 138]

1.6.2 Clinical Laboratory

IM is not yet a routine technique in the clinical laboratory, and in fact it is only within the past decade that LC-MS has been adopted in clinical settings. Recent improvements in IM include higher resolution and sensitivity, support for CCS-based identification workflows, and advancements in ambient ionization methods which merit IM consideration for deployment in clinical applications. As a gas-phase analysis technique, IM complements direct air sampling protocols. The analyses of human exhaled breath by IM offers a non-invasive rapid sampling process for diagnosis and monitoring of various disease states. Rapid disease diagnosis by breath sampling of volatile organic compounds (VOCs) with IM is thoroughly highlighted in a review published by Yost and coworkers.[139] Breath analysis by IM as a standalone system has encompassed cancer, asthma, inflammation, Alzheimer's, and Parkinson's disease states. For a clinically feasible system, the goal would be a portable, low cost IM apparatus capable of reproducible assays.[140, 141, 142]

Metabolite identification in blood samples provides insight into numerous human disease mechanisms and potential biomarkers for disease diagnosis.[143] Traditionally, LC methods are used for reducing data complexity, but at times even that may not be enough. LC-IM-MS workflows have been implemented that leverage the IM separation dimension for added peak capacity while providing an additional descriptor for metabolomic identification.[144, 145] However, without LC ("shotgun metabolomics"), Hill and coworkers demonstrated the use of two-dimensional IM-MS for detection and separation of metabolites including amino acids, carbohydrates, sterols, estrogen, and cholesterol derivatives. With a modest IM resolving power of approximately 60 (achievable with most contemporary IM instruments), detection of a comparable number of metabolomic features is achieved when compared with LC-MS.[146] Thus, further improvements in IM resolution will directly benefit the utility of IM-MS for high-throughput metabolomics of complex samples, such as blood.

With altered metabolic dysregulation being a hallmark of cancer, surgical MS techniques can support the molecular classification of tumors and assist with development of personalized medical therapies. To this end, DESI has led the way as the original ambient ionization system implemented in surgical settings. The latest iteration of ambient ionization, MasSpec Pen and the intelligent knife (iKnife), are designed to accurately assess and diagnose tissues during cancer surgery.[147, 148] While not yet widely adopted in surgical settings, these ambient ionization techniques can both be easily coupled with IM. Thus, it may be reasonable to anticipate IM supporting applications in human health by improving the separation and detection of metabolites implicated in diseases and disorders.

1.6.3 Environmental and Forensics Analysis

Environmental applications of IM include monitoring small molecules which assess the quality of air, water, and soil.[129] In these applications, the high sensitivity and compact design of DMS has demonstrated usefulness as a remote sensor for monitoring indoor and outdoor air quality.[149] Gas chromatography (GC)-DMS has been utilized within smoke detectors capable of analyzing the chemical composition of vapor from burning fiber.[150] With the potential to diminish the quality of life for both marine animals and humans, aquatic pollutants resulting from industrial sewage and groundwater contaminants are a genuine concern. IM-MS platforms have been utilized for detection of oxidized organic molecules in atmospheric gas and aerosol species.[151] With straightforward, rapid sampling methods, commercial off-the-shelf (COTS) IM systems that operate without MS analysis ("stand-alone" IM) have been employed for successful identification of phenylarsine oxide (a chemical warfare agent precursor), pesticides, and polycyclic aromatic hydrocarbons (PAHs) in environmental water samples.[152, 153, 154] High sensitivity and fast analysis times make COTS IM amenable to security applications involving detection of drugs and explosives.[129] COTS IM are designed with programmable settings simplifying use for non-technical users. Continued expansion of metabolomic detection capabilities is conceivable through advancements in programmable information such as unique spectral features of fentanyl and its analogues.[155] Figure 10.5(b) shows the IM spectra of benzoylfentanyl at varied concentrations detectable by COTS IM. The primary product ion is presented at 0.98 cm2V-2s-1 and is detectable with as little as 8.4 ng of sample. However, COTS IM are operable in "technical user" mode which allows for the detection of substances not yet programmed, broadening the detection capabilities.[156] COTS IM are particularly suited for drug and explosive analyses with non-intrusive sampling techniques such as rapid screening of hair and swabs. Using ESI-IM-MS, the Hill group detected nanomolar concentrations of caffeine and methamphetamine in hair.[157]

1.6.4 Foodomics

With a need to sustain a growing global population in combination with a continued recognition of diet impact on human health, food safety and quality analysis is more imperative than ever. Modern food safety analysis targets both natural and human-derived toxic contaminants. Food analysis aims to better understand interactions between food and the environment, including the consequences of large-scale production, organic production, food processing, packaging, and effects on the consumer. Numerous in-depth reviews of IM implementation for food analysis are available.[158, 159, 160, 161] Although currently a very limited body of work, established COTS IM systems serve as rapid and sensitive techniques for detection of small molecules, such as sugar alcohol sweeteners. Unique IM signatures for erythritol, pentaerythritol, xylitol, inositol, sorbitol, mannitol, and maltitol were evaluated and examined for recognition in commercial gum and artificial sweeteners.[162] Figure 10.5(c) displays representative IM spectra for commercial products containing different sugar alcohols. For 5® gum and Truvia®, the principal ingredients were determined by IM to be sorbitol and erythritol.[163, 164] Coupled with GC for an added dimension of separation pre-mobility, the quality characterization of virgin olive oil is achievable through identification of compounds with desirable and undesirable attributes. Of 26 identified volatile metabolites, 18 were separated and detected with GC-IM alone, totaling a classification percentage of 92% of total VOCs for virgin olive oil.[165] Because volatile aromatic compounds significantly impact food flavor, GC-IM provides a high-throughput approach aimed at non-destructive food flavoring analyses.[166] Headspace GC-IM metabolomics analysis has also been used for discrimination between winter and sapium honey.[167] With the ease of use, IM has an important role to play in food safety via non-invasive small molecule analysis.

1.7 Conclusions

Metabolomics holds enormous potential for early diagnosis, real-time therapy monitoring, identification of novel drug targets, and broadened understanding of many diseases. The expansive evolution of the metabolomics field in the past decade is in-part attributed to the adoption of ion mobility separations into MS-based workflows. IM integration efforts have been directed at reducing MS spectral complexity, increasing separations of isobaric species, improving metabolomic annotation, and obtaining gas-phase molecular structure combined with computational interpretation. With the ever expanding repertoire of next generation of IM instruments, the future for metabolomics is favorable and the application space is ever expanding.

1.8 Acknowledgements

E. Zlibut would like to thank Vanderbilt University, the Institute of Chemical Biology, and the Fisk-Vanderbilt Master's to PhD Bridge program for financial support. Thanks are also given to Jennifer Michelle Quinde for her contributions in preparation of this book chapter. This work was supported in part using the resources of the Center for Innovative Technology (CIT) at Vanderbilt University. Financial support for aspects of this work was provided by the U.S. Department of Energy, Office of Science (DOE SC) under award number DE-SC0019404. The views and conclusions contained in this document are those of the authors and should not be interpreted as representing the official policies, either expressed or implied, of the U.S. Government.

CHAPTER 2

ENANTIOMER DIFFERENTIATION OF SMALL MOLECULES BY IM-MS[1]

2.1 Introduction

While isomers differ marginally in their spatial orientation, chemical and biological activity can vary substantially. [38] Therefore, analytical strategies capable of separating small chiral molecules have a growing importance in pharmacology and biological sciences.[168] The separation of L-isoleucine and L-leucine in biological samples via liquid chromatography has been a challenge, even unattainable on normal C18 columns. Methods for LC-MS differentiation of these isomeric AAs have required sample derivatization and/or column chromatography such as HILIC.[169, 170, 171, 172] These strategies necessitate more sample preparation steps, longer analytical run times due to intensive column conditioning, and can complicate MS spectra in untargeted methods. Among emerging analytical techniques, mass spectrometry (MS) based approaches for isomer differentiation without chromatography provide advantages in versatility, speed, and sensitivity.[173, 174]

The separation of small molecular isomers and, in particular, enantiomers, pose a contemporary challenge for mass spectrometry-base analytical techniques. Historically, chiral differentiation by MS has been achieved with an enantiomer-specific tandem mass (MS/MS) dissociation technique developed by Cooks and coworkers known as the kinetic method. [49, 50, 51] In the kinetic method, metal-bound isomer complexes are formed in the presence of a chiral reference compound (chiral selector, CS) and are then dissociated to probe isomer-specific fragmentation thresholds. The CS forms complexes with the dielectric metals that are capable of interacting enantio-selectively with small molecule isomers. Since the dissociation rates amongst complexes are stereospecific, different product ion branching is observed and used to quantify enantiomeric excess.[49] Detection and quantification of enantiomeric excess of atenolol, DOPA, ephedrine, pseudoephedrine, isoproterenol, norepinephrine, and propanol drug mixtures have been successfully measured with samples containing less than 5% enantiomeric contamination. The kinetic method has also demonstrated utility with α-hydroxy acids and amino acids with various dielectric metals and chiral selectors.[52, 53, 54]

More recently, IM-MS has been utilized to differentiate chiral molecules.[175, 40] MS separates ions based on intrinsic mass, whereas IM provides separation of ions based primarily on differences in size and shape, thus, IM-MS is considered a structurally selective analytical technique. While the direct resolution of

---

[1] Parts of this chapter have been adapted from "Enantiomer Differentiation of Amino Acid Stereoisomers by Structural Mass Spectrometry Using Noncovalent Trinuclear Copper Complexes", published in *Journal of the American Society for Mass Spectrometry* and has been reproduced with the permission of the publisher

chiral isomers is generally not attainable with the resolving power accessible by current IM-MS instrumentation (< 100), ion complexation strategies have been used to impart measurable structural differences in these systems.[42, 62] Ion complexation strategies are currently the only known reproducible approaches for conducting IM-MS chiral separations. Notably, cyclodextrin inclusion complexes have demonstrated measurable structural differences between enantiomers when analyzed by IM-MS, although these strategies rely on the analyte being sufficiently small to incorporate within the cyclodextrin cavity.[176, 177, 178] Utilizing varying IM-MS techniques, differentiation of enantiomeric species has been demonstrated via copper and nickel metal complexes.[56, 59] Recently, binuclear complexes incorporating two coordinating copper cations have been demonstrated to impart significant structural differences between enantiomeric amino acids which are measurable by IM-MS.[61]

In this work, trinuclear copper complexes are investigated for their ability to amplify minor structural differences between small molecule chiral enantiomers, allowing several amino acid enantiomers to be directly resolvable by a conventional resolution drift tube IM-MS. Copper is explored in this study because of prior success using this metal in other isomer-differentiation studies, which results in part from the high affinity for copper to bind with aromatic rings in comparison to other divalent metals such as Zn^{+2} and Ni^{+2}.[179, 180, 181] Specifically, this allows copper to bind to the ring in histidine to form a stereoselective complex. Direct CCS determination on these complexes are used in conjunction with computational results guided by tandem MS/MS data to correlate the IM-MS measurements to candidate molecular structures. These findings collectively suggest a chirally-selective structure of the form $[(Cu^{2+})_3(^{D/L}AA)_3(^{L}CS)_2 - 5H]^+$ in which the complex is centrally bridged by three coppers can provide significant selectivity in the differentiation of chiral amino acids.[179, 180, 181]

2.2 Experimental Methods

2.2.1 Standards and Chemicals

Optically pure chiral amino acids were sourced from various vendors, summarized in Table B.1. Copper acetate was obtained from Sigma Aldrich. High purity (Optima Grade) methanol and water were obtained from Fisher Scientific. All chemicals were used as received.

2.2.2 Sample Preparations

Amino acids and copper acetate were dissolved in 1 mg/mL and then diluted to 500μM stock solutions in water. Samples prepared for IM-MS analysis contained 20μM amino acid, 20μM of a chiral selector (see below), and 20μM of $Cu(OAc)_2$ in 50:50 methanol/water. Molar concentrations of varying sample components (3-fold change for each component) and solvent compositions (0-90% water) were explored.

The sample conditions described are based on high complexation abundance.

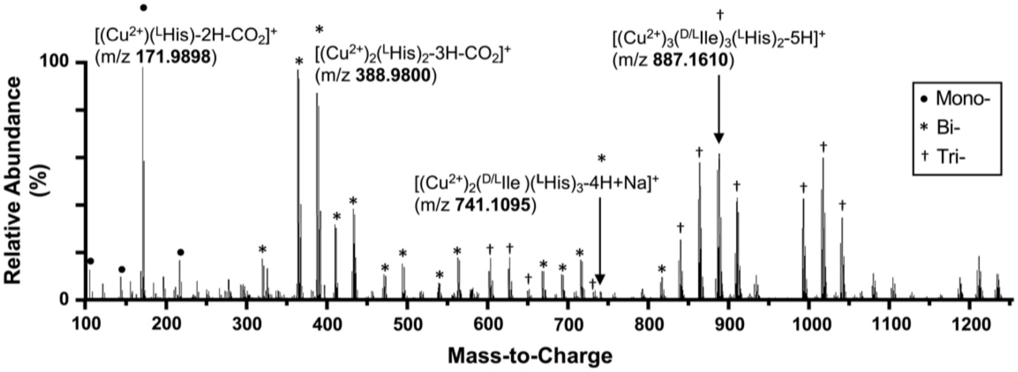

Figure 2.1: Isoleucine, l-histidine, and copper acetate mass spectra.

(A) Exemplary mass spectrum for a solution of copper acetate and L-histidine (chiral selector) added to a mixture of D- and L-isoleucine, yielding numerous noncovalent metal ion complexes. Copper-containing cluster ions are annotated with symbols, and include mononuclear, binuclear, and trinuclear copper complexes.

2.2.3 Instrument Parameters

Samples were directly infused at 10μL/min into a thermally-assisted electrospray ionization source (ESI, Jet Stream, Agilent Technologies, Santa Clara, CA) coupled to a drift tube ion mobility-quadrupole time-of-flight MS (6560 IM-QTOF, Agilent). The instrument was operated in positive ionization mode, with the QTOF tuned for standard mass range (m/z 50-1700 mode) analysis. ESI source conditions utilized a drying gas temperature of 325 °C and flow rate of 13 L/min. The ion transfer capillary entrance voltage was held at 4000 V and the focusing nozzle set to 2000 V. IM separations were performed at uniform field in the 78.1 cm drift tube operated with high purity nitrogen drift gas regulated to 3.95 ± 0.01 Torr at room temperature (≈300 K). Ion mobility parameters were adjusted to maximize the transmission of the noncovalent copper complexes, namely a higher longitudinal DC voltage (funnel delta) in the high-pressure funnel, a higher confining RF voltage in the ion funnel trap, and higher trap entrance grid potentials during both the trap filling (grid low) and confining (grid delta) sequences. These and other instrument parameters are summarized in Figure B.1.

2.2.4 Experimental CCS Calculations

A standardized stepped-field CCS measurement technique was used to determine drift tube collision cross section values in nitrogen gas (^{DT}CCS$_{N2}$) from first principles theory.[96, 85] Briefly, the voltage applied across the drift tube was varied across 7 increments from 550 to 1550 V (7.0 to 19.8 V/cm) and linear regression analysis of the arrival times was used to determine the time ions reside outside of the drift region. The corrected drift times and instrument conditions (pressure and temperature) were then used to obtain CCS values based on the fundamental low field IM equation (Mason-Schamp relationship). From these CCS measurements, the CCS arrival time relationship was determined and subsequently used to project the IM spectra in CCS space.

2.2.5 Assessment of Separation

The difference in CCS (ΔCCS), as well as the peak-to-peak resolution (R$_{p-p}$), were used to quantify the extent of chiral differentiation for enantiomer pairs. R$_{p-p}$ was calculated from the IM arrival time measurements using equation (1).[55, 81]

equation 1. $R_{p-p} = 1.18 * (t_D - t_L/W_D + W_L)$

Where t$_L$ and t$_D$ refer to the drift times of the D- and L- enantiomers obtained from the centroid of the IM arrival time distributions, and W_L and W_D refer to their corresponding peak widths measured at half the peak height (full width at half maximum). The coefficient of 1.18 results from the relationship between the standard deviation, σ, to the half-height width ($2.355\sigma/2$). Typically, a larger ΔCCS corresponds to a higher R_{p-p} for diastereomeric ions, however, R_{p-p} also accounts for the peak width which increases with the ion drift time (via diffusion) and when sampling unresolved ion structures. For context, an R_{p-p} of 0.6 corresponds to ≈50% overlap between two neighboring peaks (half-height separation), $R_{p-p} = 1.0$ represents ≈10% overlap, and an $R_{p-p} \geq 2.0$ indicates baseline separated peaks with no overlap.[55]

2.2.6 Computational Modeling and Theoretical CCS.

Chemical structures for the most abundant trinuclear ion complex observed, $[(Cu^{2+})_3(^{D/L}Ile)_3(^{L}His)_2 - 5H]^+$ were constructed and energy minimized using MM2 force field optimization. MM2 parameters for Cu-His and Cu-Ile bond stretching and atom types were input from density functional theory (DFT) optimization of Cu-His and Cu-Ile structures. DFT optimization and harmonic frequency analysis were performed using Gaussian 16 program package with unrestricted B3LYP level and a double- 6-31++G(d,p) basis set. Theoretical CCS values for energy-minimized $[(Cu_3^{2+}(^{D/L}Ile)_3(^{L}His)_2 - 5H]^+$ structures were obtained using both the trajectory method (TM) with revised parameters for nitrogen drift gas, and the projected superposition approximation (PSA).[116, 117, 111, 112] Using the same molecular interactions, D- and L- trinuclear copper complexes for leucine, valine, and lysine with L-histidine chiral selectors were also constructed, and theoretical CCS values were calculated from the structures following MM2 optimization.

2.3 Results and Discussion

2.3.1 Ion Detection

The ESI IM-MS analysis of a sample mixture of D/L-isoleucine, L-histidine, and copper acetate (1:1:1) yielded numerous ion signals for mononuclear, binuclear $[(Cu^{+2})_2(AA)(CS) - 4H - Na]^+$, and trinuclear $[(Cu_3^{+2}(AA)_3(CS)_2 - 5H]^+$ copper-bound clusters (Figure 1). While complex, the added peak capacity of the IM-MS spectra allowed for discrete cluster ions to be isolated. Thus, the majority of the CS and AA containing complexes were stoichiometrically identified by accurate mass measurement (±5 ppm) and isotopic envelope matching (Table B.2, Figure B.2).

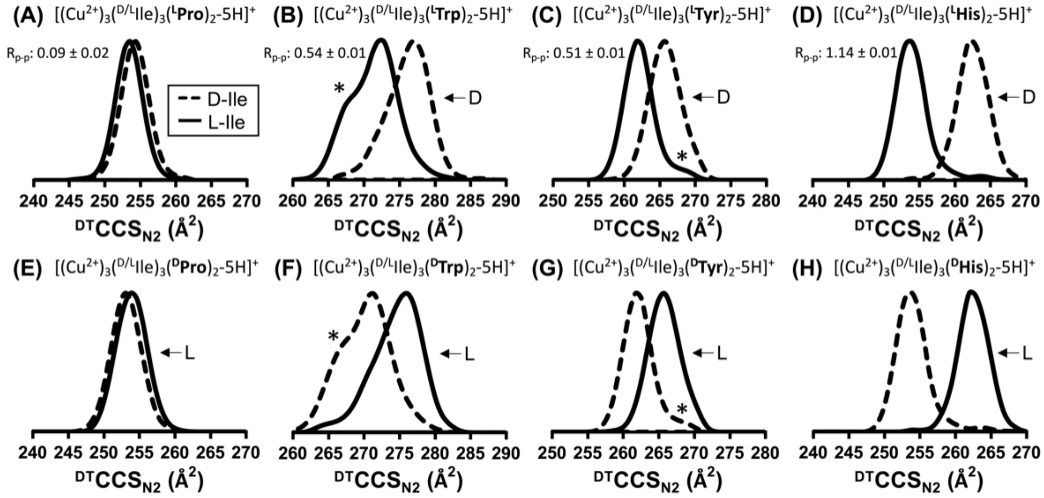

Figure 2.2: Chiral selector effects on IM separations.

Ion mobility spectra for D- or L-isoleucine trinuclear copper complexes incorporating the chiral selectors, proline, tryptophan, tyrosine, and histidine. For the different chiral selectors investigated, proline (A and E) demonstrated a low degree of enantiomeric selectivity for isoleucine, whereas tryptophan (B and F) and tyrosine (C and G) both exhibited relatively higher enantiomeric selectivity for differentiating D- and L-isoleucine, with histidine resulting in the highest degree of differentiation (D and H). In all of these results, changing the chirality of the selector resulted in an inverted ordering of CCS values, but did not change the profile of the IM distributions observed. The asterisks (*) denote reproducible secondary features of the peak profiles.

2.3.2 Enantiomer Separation

Protonated AA enantiomers and diastereomeric dimers and trimers that form with Cu and AAs are not sufficiently distinct in structure to achieve separation via IM-MS at conventional resolving powers (ca. 50). Binuclear copper clusters, which are a larger assembly of analytes, chiral selectors, and metal ions, exhibited a greater difference in CCS between enantiomers and thus, better chiral discrimination, as previously reported.[61] Here, IM-MS analysis of binuclear copper bound tetramers exhibited good chiral discrimination between charged and polar AAs, but appeared to exhibit limited IM-MS separation between hydrophobic AA enantiomers. Trinuclear copper-bound complexes, on the other hand, demonstrated a high degree of chiral discrimination for hydrophobic AAs and was the focus of additional study. Proline, histidine, tryptophan, tyrosine, and glutamine were investigated as potential CSs and the isoleucine enantiomers were chosen as an evaluation case.[42] The degree of AA enantiomeric differentiation, observed in this study was found to be affected by the identity of the CS. Of the CSs investigated, proline and glutamine exhibited a lower degree of differentiation selectivity with all AAs tested, in comparison to aromatic ring-containing CSs such as histidine, tyrosine, and tryptophan. This would suggest that the aromatic ring has an important role in forming chiral-specific ion complexes of the nature explored in this study. The observed differentiation for isoleucine isomers in combination with varying aromatic chiral selectors L-tyrosine (Figure 2c), L-tryptophan (Figure 2b), and L-proline (Figure 2a) was found to be lower than the resolution observed using an L-histidine chiral selector (Figure 2d). The highest resolution observed for the D/L-isoleucine mixture ($R_{p-p} \approx 1.14$) was achieved with an L-histidine CS. Published work on the kinetic method demonstrated improved analyte differentiation when using D-chiral selectors. Here, varying the chiral identity of the CS did not significantly improve differentiation though interestingly, the chiral identity of the CS did affect the arrival time order of ions in the IM spectra. As shown in Figure 2a-d, L-isoleucine (black solid trace) has a smaller CCS than D-isoleucine (black dotted trace) when an L- CS is used, suggesting a more compact conformation is formed with L-isoleucine in each case. However, the reverse is observed with a D- CS (Figure 2e-h). This phenomenon reproducibly occurs with each CS investigated and not only is the elution order reversed for D- vs L- CSs, but the profile of the IM-MS distributions also remained virtually identical regardless of CS chiral identity. For example, the observed ‘shoulder’ and ‘tail’ features (denoted by ‘*’ in Figure 2) are preserved between both D- and L- CSs, suggesting the complexes have highly conserved gas-phase structures. Among the CSs investigated, L-histidine yielded the highest degree of differentiation with all 16 AA enantiomer pairs investigated in this work.

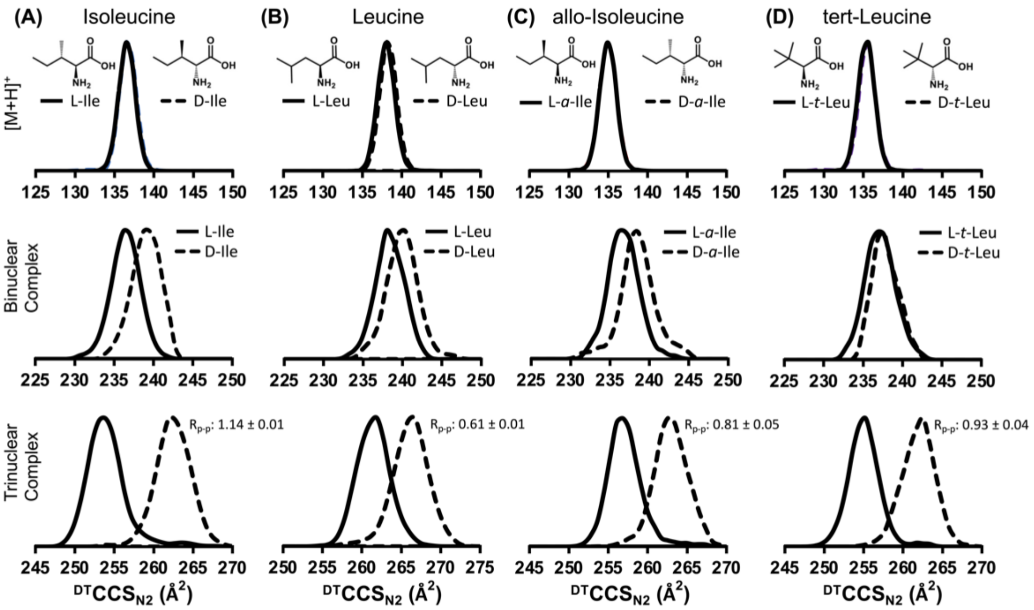

Figure 2.3: Isoleucine IM separations.

Ion mobility spectra for isomers (A) D/L-leucine, (B) D/L-isoleucine, (C) D/L-allo-isoleucine, and (D) D/L-tert-leucine. Top row: spectra for the protonated ions of each isomer (m/z 132.1024), showing no measurable CCS differences between the enantiomer (D/L) pairs. Middle row: IM spectra for the binuclear ion complexes, $[(Cu^{+2})_2(AA)(CS)-4H-Na]^+$, demonstrate some degree of chemical selectivity between enantiomers. Bottom row: the trinuclear complexes, $[(Cu^{2+})_3({}^{D/L}Ile)_3({}^{L}His)_2-5H]^+$, exhibited a relatively high degree of chiral selectivity, with better than half-height separation of individual IM distributions observed for all enantiomeric pairs.

The IM results for eight AA isomers sharing the same chemical formula (D/L forms of isoleucine, leucine, allo-isoleucine, and tert-leucine; $C_6H_{13}NO_2$) are shown in Figure 3. D/L enantiomer pair results for the pronated ion as well as the binuclear and trinuclear copper complex are shown for each isomer. As expected, the quasi-molecular ion form of the enantiomer pairs ($[M+H]^+$, m/z 132.1024) exhibit no measurable CCS differences. Binuclear copper complexes which incorporate a single CS show some structural selectivity by IM, however these complexes are not resolvable in a mixture. The largest CCS differences between enantiomers were found with the trinuclear copper complexes incorporating 3 CSs, with greater than half-height separation ($R_{p-p} > 0.6$) observed in all cases. These trinuclear ion adducts exhibited CCSs that span approximately 26 $\AA^2$, higher than both the quasi-molecular ions and binuclear cluster ions which span approximately 10 $\AA^2$ and 15 $\AA^2$, respectively. All empirically-measured CCS values for AA enantiomers forming trinuclear copper complexes in the presence of an L-histidine CS are plotted with respect to their mass-to-charge ratio in Figure 4. Linear fits for L- and D- AAs establish that the complexes incorporating L- enantiomers typically have a smaller CCS than those incorporating D- enantiomers in the presence of an L-histidine CS. Exceptions include lysine which formed the trinuclear complex but exhibited minimal CCS differences, and the D-asparagine complex which had a smaller CCS value than expected based on the structural trends. Not included are, Met, Ser, Cys, Glu, and Asp amino acids, which did not form high abundance trinuclear complexes using a histidine chiral selector, though we note here that other chiral selectors were not explored for these amino acids. For all complexes incorporating an L-histidine CS, the ΔCCS and R_{p-p} values for AA enantiomers which exhibit $R_{p-p} \geq 0.6$ are summarized in Table B.3. Because these trinuclear ion complexes incorporate three AAs, it was found that the empirically measured R_{p-p} from pure L- or D- samples does not always precisely represent the degree of separation observed within a mixture.

This is thought to be a result of mixed stoichiometries of D- and L- enantiomers being incorporated into overlapping trivalent complexes, which result in additional, unresolved IM features that may overlap in the separation window of the pure enantiomer forms. Figure B.3 includes mobility spectra for mixtures containing isoleucine, leucine, and tert-leucine trinuclear copper complexes. This added spectral congestion may, in turn, limit the accuracy of quantitative efforts which seek to calculate the enantiomeric excess using these copper binding strategies. Nonetheless, even with the modest resolving powers available on first-generation IM platforms ($\approx$50), trinuclear complexes allow for measurable structural differences which can be used to detect the presence of enantiomers.

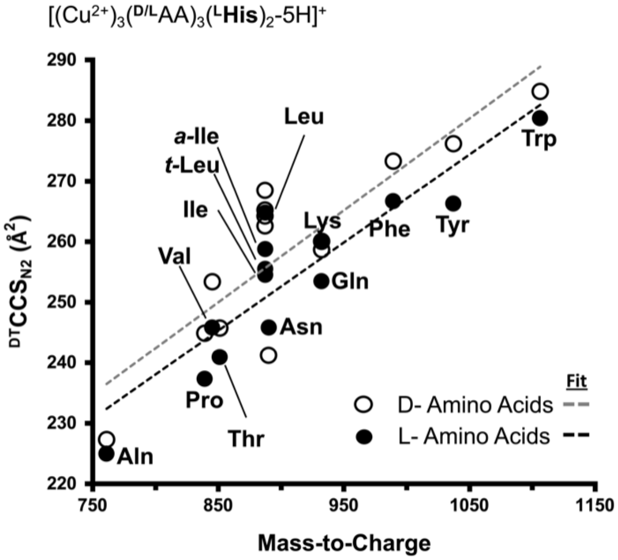

Figure 2.4: Trinuclear AA CCS measurements.
Empirically measured CCS data points plotted as a function of mass-to-charge for AA-containing trinuclear copper clusters in the presence of an L-histidine CS.

2.3.3 Structural Insight from Theory

A limited body of work exists on implementing computational techniques for structural modeling of multi-metal systems due to the associated computation costs of these systems. Tandem MS/MS experimental results were used to guide the assembly of the structures used for computation modeling. MS/MS results for the isoleucine-containing trinuclear complex, $[(Cu^{+2})_3(Ile)_3(His)_2 - 5H]^+$, are shown in Figure B.4. With major ion fragments listed in Table B.4. The first dissociation channels observed are the loss of all isoleucines from the $[(Cu^{2+})_3(Ile)_3(^LHis)_2 - 5H]^+$ (m/z 887.1610) ion complex, suggesting this analyte experiences weaker guest interactions with a more stable copper-histidine host assembly (Figure B.4). Fragment ion relative intensities as a function of collision voltage are summarized in Figure B.5. At higher collision energies, two ion fragments containing both copper and histidine, $[(Cu^{2+})_2(^LHis)_2 - 2H]^+$ (m/z 433.37) and $[(Cu^{2+})_2(^LHis)_2 - CO_2 - 3H]^+$ (m/z 388.98), remained intact. The loss of H2CO2 between m/z 433.37 and 388.98 complexes is characteristic of copper-amino acid complexes, and this observation suggests a strong affinity between Cu^{+2} and histidine ring/N amine group.[182] This informed the assembly of a copper-histidine core with a “pocket’ that incorporated the analytes. Once assembled, these trial structures were subjected to the computational workflow incorporating the ion mobility results (Figure B.6a). Energy minimized candidate structures for D- and L-isoleucine trinuclear copper complexes with an L-histidine CS are presented in Figure 5. In these structures, L-histidine preferentially binds to copper through the imidazole ring and amino group. A second copper is bound to L-histidine through the carboxylate anion. This base architecture interacts with L-isoleucine to favorably form a compact complex (Figure 5b). In contrast, when D-isoleucine is incorporated into the host assembly, the structure is forced into an extended alignment due to steric hindrance (Figure 5a).To correlate these computational findings with experimental results, the TM and PSA methods, were implemented.[123] The theoretical CCS values obtained from both methods were within 1.5% of the empirical CCS results, suggesting these low-energy computational structures are representative of the gas-phase conformations measured by the ion mobility experiment. Empirically measured CCS measurements D- Ile (264.2 $Å^2$) and L- Ile (255.5 $Å^2$) were reproducible to within 0.6% RSD (n $\geq$ 3).

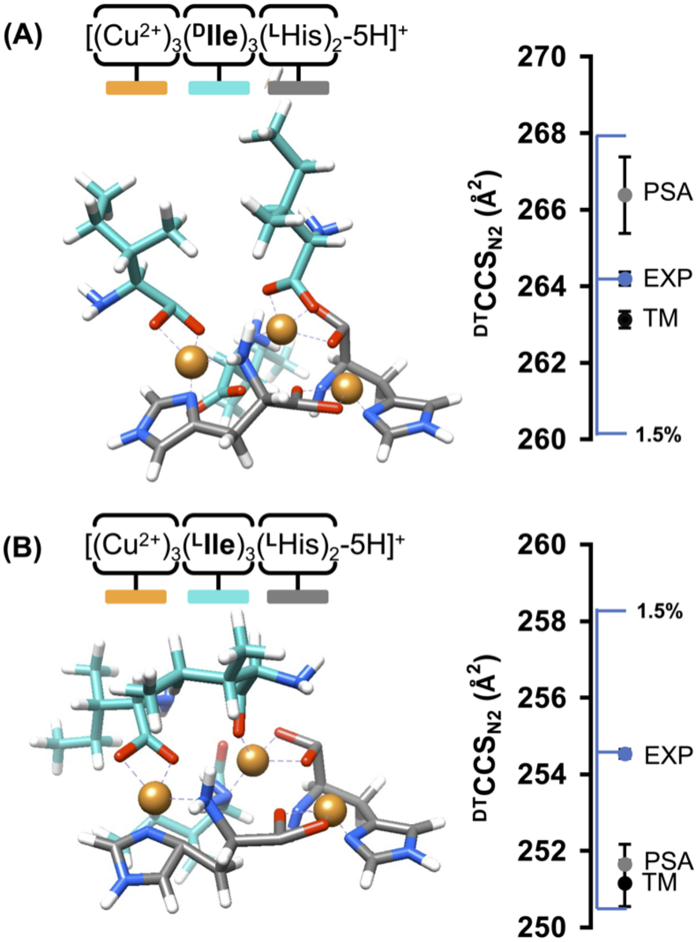

Figure 2.5: Isoleucine trinuclear theoretically predicted structures.
Predicted structures for (A) $[(Cu^{2+})+3(^{D}Ile)_3(^{L}His)+2-5H]^+$ and (B) $[(Cu^{2+})_3(^{L}Ile)_3(^{L}His)_2-5H]^+$ with experimental (EXP) and theoretical CCS value obtained from two methods (TM and PSA). Theoretical CCS values are within noted 1.5% error of experimental CCS.

Importance was also placed on the agreement between theoretical and empirical results in regard to the CCS differences. Theoretical and empirical differences (noted as CCS%) between trinuclear complexes incorporating AA enantiomeric forms of isoleucine, leucine, valine, and lysine are shown in Figure B.6b. Empirically, isoleucine, leucine, and valine exhibited differentiation with $R_{p-p} > 0.6$, and therefore a larger CCS% difference, whereas lysine exhibited no measurable IM-MS separation for its corresponding trinuclear copper complex in the presence of an L-histidine CS. Theoretical separation trends for optimized isoleucine, leucine, valine, and lysine complexes are in good agreement with empirical observations. Optimized leucine, valine, and lysine structures are shown in Figure B.7. An overlay of D- and L- trinuclear complexes (three coppers visually aligned) for isoleucine (R_{p-p}= 1.14) and lysine (R_{p-p}= 0.01) are shown in Figure B.8. Modeled isoleucine trinuclear complexes (highest degree of differentiation) contain a conserved histidine-copper core between L- and D- conformations while lysine tri-nuclear complex (lowest degree of differentiation) exhibit less simulations of the core structure across the overlays. In comparing modeled structural overlays of isoleucine, leucine, valine, and lysine, the degree of differentiation is positively correlated with a preserved histidine-copper core between enantiomers. The lack of a conserved histidine-copper core appears to reduce stereoselectivity resulting in complexes with similar CCS values for both L- and D- AA. These findings suggest future efforts which focus on designing an aromatic diamino bridge with less molecular flexibility (increased conservation of the stereoselective histidine-copper core). A conserved core would increase stereoselectivity and may help expand the utility of trinuclear complexes to differentiating a wider range of analyte enantiomers, such as drug and drug-like compounds.

2.4 Conclusions and Future Directions

Trinuclear copper complexes incorporating amino acids demonstrated measurable gas-phase CCS differences which allowed for the differentiation of hydrophobic AA enantiomers and leucine constitutional isomers, including their enantiomeric pairs. Computational modeling was used to provide insight into the structural differences between enantiomers that were resolved via IM-MS. Candidate structures of the trinuclear complex with the experimentally-observed stoichiometry (3 coppers, 2 histidines, 3 AAs) were assembled in silico using guidance from tandem MS/MS ion fragmentation data. The theoretical structures which correlated closely to the experimentally measured CCS values (within 1.5%) suggest that a central histidine-copper core is formed which enables the assembly of a chirally-selective inclusion complex for binding AA enantiomers. As demonstrated in this work, direct IM-MS analysis of trinuclear copper complexes provides new avenues for chiral differentiation of amino acids. While not a focus of this current work, the quantitative determination of enantiomeric excess is of interest, and should be accessible as long as peak areas can be accurately determined (i.e., R_{p-p} of 0.6 or greater). The measurable differences in CCS across the various isomers suggests that quantitative determination of enantiomeric excess can be achieved using higher resolution ion mobility separations. The applications of this copper complexation strategy for resolving other small molecule isomers, such as drug enantiomers, are currently the subject of future work.

2.5 Acknowledgements

E.Z. would like to thank Jennifer M. Quinde, Berkley Ellis, Katrina Leaptrot, and Bailey Rose for their intellectual contributions. This work was supported in part using the resources of the Center for Innovative Technology at Vanderbilt University. Financial support for aspects of this work was provided by the National Institutes of Health (NIH R01GM107978), the Vanderbilt University College of Arts and Sciences, and the Fisk-Vanderbilt Masters to Ph.D. Bridge program.

CHAPTER 3

GAS-PHASE CONFORMATIONAL ANALYSIS[1]

3.1 Introduction

Included in chapter 1 was a general overview of computational modeling. The following chapter contains a more detailed description of the approach developed and utilized in the McLean lab. As noted, previous McLean lab studies have utilized our workflow on singly cation charge gas phase ions. [30, 127, 31] While this technique has not be yet been published with multiply charge systems, in the following study we demonstrate the utility of this workflow with such systems. However, some additional considerations and developments were necessary for expanding the workflow to model protonated species and multiply charge ions in the gas phase. In a case of multiply charge species, cations tend to drift apart as the energy of the system increases through a temperature gradient that takes place during a simulated annealing dynamics. Therefore, when modeling multiple cations in a simulation, a distance constraint must be placed on the cations to prevent too great a drift that the cations are unable to interact with the target molecules as the systems cools. Without restriction, many of the final structures would be representative of species that are not observed experimentally.

Even more computationally expensive to model is the case of protonated species. Alkali metal cations are introduced into the system as a free-floating charge and tends to localize in the most energetically favorable positions during the molecularly dynamics simulations. However, protonation cannot be introduced as a free-floating charge and instead needs a pre-defined interaction site with the molecule. The challenge with modeling protonated species with defined protonation sites is the need to identifying the most energetically favorable. This can be achieved in two steps, (1) running DFT QM energy minimization of the neutral structure to identify the most basic molecular sites and (2) running MD simulations for each of the most likely protonation site.

Computational models have been used to provide structural insight into the gas-phase conformations of polymeric species and Nonapeptides observed in experimental CCS measurements. MD simulations are used to compute theoretical structures representing the energy profile, or the conformational landscape, of a given molecule. The calculated CCS values of the generated conformations provide insight into the structure of the observed local energy minima of an ion within experimental IM measurements. The following instigation encompasses multiply charged Polyurethanes (PURS) and Nonapeptides to demonstrate the modeling

---

[1] Parts of this chapter have been adapted from “Mass Spectrometry and Ion Mobility Study of Poly (ethylene glycol)-based Polyurethane Oligomers”, published in *Rapid Communications in Mass Spectrometry* and has been reproduced with the permission of the publisher

approach. Gas-phase structural variance of three isomeric PUR oligomers formed from Methylene diphenyl diisocyanate (MDI) and PEG having one MDI (M)and 12 polyols (PEGs) were initially investigated (Figure C.1). One PUR oligomer is the symmetrical (PEG)6-M-(PEG)6 oligomer (6-M-6); and the other two are (PEG)4-M-(PEG)8 (4-M-8) and (PEG)2-M- (PEG)10 (2-M-10). The different polymeric sequence was reported to result in unique CCS measurements when doubly sodium adducted. [125] The published experimentally measured CCS values for these isomeric PUR oligomers serve as a metric for comparison with theoretical results.

An oligopeptide formed from nine amino acids (Figure C.2), vasopressin is a biologically relevant hormone responsible for regulating tonicity of body fluids. [183] IM-MS reports on protonated L-vasopressin uniquely exhibited two gas-phase conformations with comparable probability of formation. [40] Preliminary computational models have suggested the two peak distributions is a result of Vasopressin's tail existing in both a folded and extended conformation. To better understand this structural property of Vasopressin, pressinoic acid (Vasopressin peptide ring absent of peptide tail) is explored by IM-MS and computational modeling approaches in the following study. In addition, protonated L-vasopressin with the addition of various cations is explored as a tactic of shifting the gas-phase structure to favor one conformation over the other. An understanding

Lastly, the additional IM resolving power and tandem IMS capabilities of the cyclic IM-MS is explored as a means of understanding the energy threshold necessary for inter-conversion between the two conformations. [184, 185, 186]

3.2 Methods

3.2.1 Standards and Chemicals and Sample Preparations

Vasopressin, pressinoic acid, and chloride salts were obtained from Sigma Aldrich. High purity (Optima Grade) methanol and water were obtained from Fisher Scientific. All chemicals were used as received. 100 uL of sample was prepared in water with 100 mol excess chloride salt (LiCl, NaCl, KCl). Samples were shipped to Waters for analysis on cyclic-IM-MS.

3.2.2 Instrumental Parameters

Samples were directly infused at 10 µL/min into a thermally-assisted electrospray ionization source (ESI, Jet Stream, Agilent Technologies, Santa Clara, CA) coupled to a drift tube ion mobility-quadrupole time-of-flight MS (6560 IM-QTOF, Agilent). The instrument was operated in positive ionization mode, with the QTOF tuned for standard mass range (m/z 50-3200 mode) analysis. ESI source conditions utilized a drying gas temperature of 325 °C and flow rate of 13 L/min. The ion transfer capillary entrance voltage was held at

4000 V and the focusing nozzle set to 2000 V. IM separations were performed at uniform field in the 78.1 cm drift tube operated with high purity nitrogen drift gas regulated to 3.95 ± 0.01 Torr at room temperature (300 K). Ion mobility parameters were adjusted to maximize the transmission.

3.2.3 Computational Method

Insights into the gas-phase conformation of IM-MS results were supplemented with computational studies. Computation modeling included a two-step approach: (1) sampling conformational space and (2) obtaining CCS values for the generated conformations. A geometry optimization at the Hartree-Fock level with a 6-31G* basis set was performed with Gaussian 09 for each of the PEG-PUR oligomers and Nonapeptides separately. Partial charges were derived from ab initio electrostatic potential calculations using a 6-31G* basis set. Appropriate cations or protonation was added post-optimization and partial charge computations with tLeap. Conformational sampling was accomplished using a simulated annealing protocol implemented in AMBER. In multi-cation simulations, cations were restricted to 20 Å distance from a central carbon for the entirety of the simulation. For each simulations, a molecular dynamic (MD) simulation began by heating the molecule from 0 K to 800K over 250 ps, followed by a maintained temperature of 800K for 9000 ps. With continuous temperature at 800 K, a structural snapshot was acquired every 16,667 steps, and a total of 3000 structural snapshots were saved. These 3000 high-energy structures were then cooled to 300 K during a 15 ps MD simulation. Theoretical CCS values for the resulting 3000 conformations were determined using MOBCAL software. Projection approximation (PA) was used to generate helium CCS values. [123, 111, 114] For comparison to nitrogen experimental measurements, nitrogen PA CCS values were determined for a set of conformations spanning the entire CCS range using the projected superposition approximation (PSA). These values were used to create a linear trend and obtain nitrogen CCS values for the remaining conformations. [187, 188]

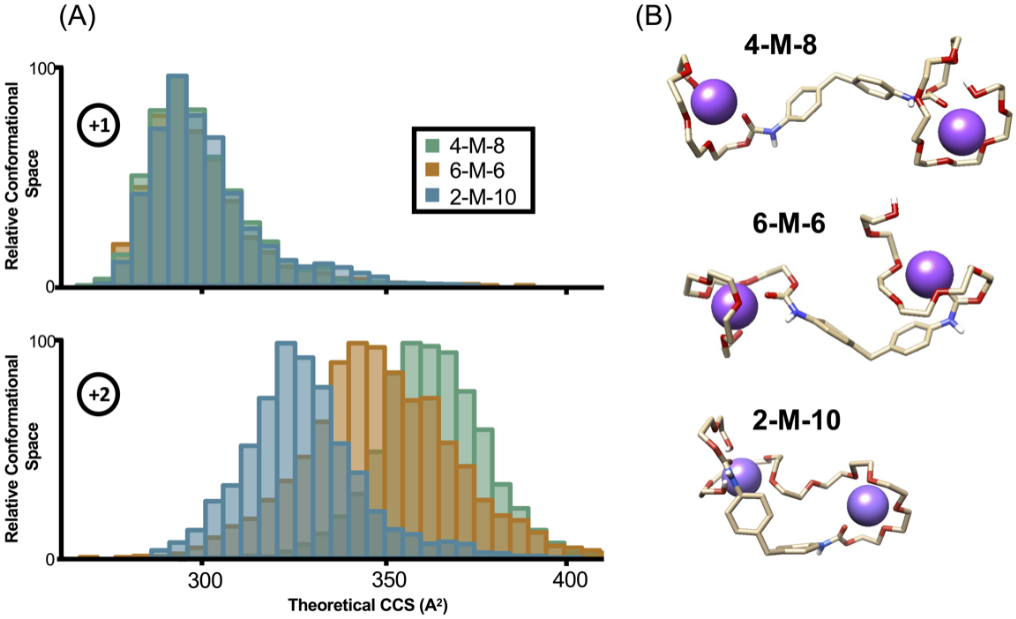

Figure 3.1: Theoretically modeled PEG oligomers.
Theoretical results of 2-M-10, 4-M-8, and 6-M-6 oligomers. (A) Singly and doubly sodiated CCS histogram distributions and (B) lowest energy structures of doubly sodiated oligomers.

3.3 Results

3.3.1 Polyurethanes

Figure 3.1(A) include the CCS distributions of 3000 theoretically generate structures of singly and doubly sodium-adducted. Similar CCS distributions were observed for single sodium-adducted ions, while unique CCS distributions were noted in the presence of a second sodium ion. Gas-phase structure of doubly sodium-adducted PEG-PUR oligomers resulted in a sequence dependent shifted in CCS spaces. Theoretical CCS values obtained were within a 5% difference of the experimental measurement, and there is good agreement between experimental and theoretical distributions. Experimental CCS measurements and distributions used for comparison were collected by Harris and collogues. [125] Theoretical CCS calculations show the lowest conformational density for the doubly sodium-adducted 2-M-10 oligomer, followed by the 6-M-6, and then the 4-M-8 oligomers. Structural analyses suggest that 2-M-10 oligomer coordinates both sodium cations on the larger polymeric arm with 10 monomers, which could be the cause of the observed more compact gas-phase conformation, as shown in Figure 3.1(B). The larger CCS density of the 6-M-6 and 4-M-8 species is attributed to each arm of the polymer coordinating a sodium cation yielding a more extended structure. The conformational density from tentative CCS values reflects the observed size separation from experimental measurements.

3.3.2 Nonopeptides

Shown in Figure C.3, protonated L-vasopressin exhibits two unique peaks in the mobility distributions indicative of two gas-phase conformations. This is distinct to L-vasopressin as only a single peak is observed with D-vasopressin. However, it is important to note that a slight shoulder is observed for protonated pressinoic acid. Figure C.4 are the mobility distributions of D- and L- vasopressin [M+H+X]+2 adducts (where X = Li, Na, or K). Single distributions are observed for L-vasopressin with the addition of cations. However, in the presence of a Li cation, a slight shoulder is observed. This is also corroborated with [M+X]+1 adducts (where X = Li, Na, or K). With D-vasopressin, single distributions are observed for Li and Na, but two peaks occur in the presence of K cation.

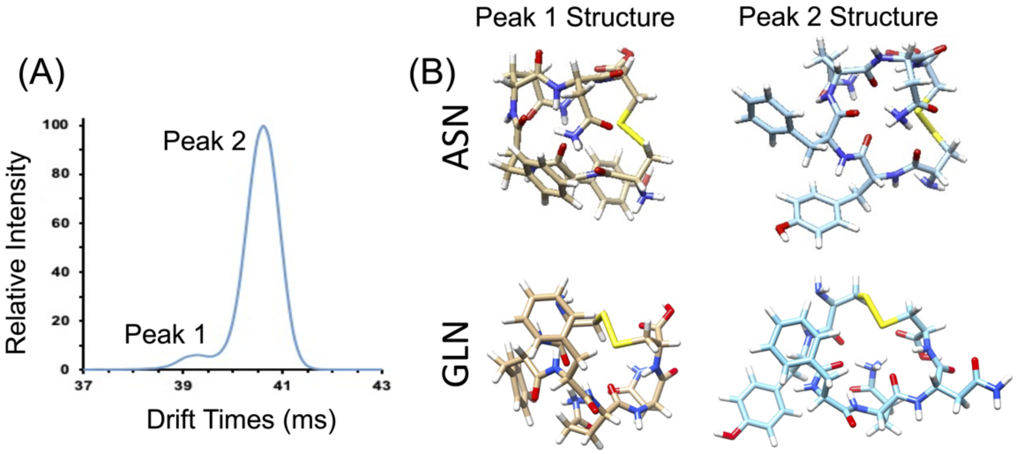

Figure 3.2: IM-MS structural analysis of pressinoic acid
Pressinoic $[M+H]^+$ (A) IM-MS distributions and (B) lowest energy theoretical structures with ASN and GLN protonation sites

Multiple confirmations also observed with protonated vasopressin (contains the pressinoic acid ring structure). Important to note that the addition of a D-Vasopressin tail leads to one confirmation. Water cyclic IMS instrument is unique capable of tandem cIMS experiments, allowing for the storing of ion packets "sliced" from either peak in the L-vasopressin distributions, clearing of cyclic mobility chamber, and then reintroduction of store ion packets. A single observed peak after a second IMS experiment on the stored ion packets would suggest two distinct gas-phase conformations for L-vasopressin. An observation of two peaks signifies gas-phase inter-conversion between the two conformations. Ejection of pre-stored 1st and 2nd distributions of L-vasopressin are shown in Figure C.5. Two conformers were observed after a single pass with either peak of L-Vasopressin and these conformers continue to inter-convert. The "sliced" ion exhibits higher intensity but continue to equilibrate with increasing number of passes. While in solutions, proteins and metabolites may experience many conformations through exchange of hydrogen ions with acid solutions, but protonation studies suggest that protonation sites are "locked-in" during ESI process and transitioning into vacuum. [189, 190] This observed inter-conversion lessens the likelihood that the two peaks observed for l-vasopressin are due to two equally favorable protonation sites. The two distributions are instead conformational changes. Interestingly "slicing" the two main peaks in the pressinoic acid distributions, Figure C.6, for tandem IMS analysis similarly results in redistribution suggesting once again inter-conversion is taking place of the ring itself. This would suggest that the vasopressin tail folding may not be the only aspect contributing to the two gas-phase conformations. The collapse of the "ring" structure may also be causative.

Cys, Asn, and Gln, were each investigated as likely protonation sites of pressinoic acid. CCS and relative energy distributions for 3000 theoretical structures for each protonation site are shown in Figure C.7. CCS for each of the simulations fall within a similar CCS window in good agreement with experimentally measured CCS values. Based on these results, an Asn protonation is the most energetically favorable, with Cys and Gln sites having similar energetics. The lowest energy structures of pressinoic acid that correspond with "Peak 1" and "Peak 2" with Asn and Gln protonation site are shown in Figure 3.2(B). Because the distribution labeled "Peak 2" in Figure 3.2(A) forms in high abundance, it would suggest that it should be more energetically favorable. While Asn is theoretically the most energetically favorable, with an Asn, protonation site energetic landscape it would be expected that "Peak 1" is in highest abundance. Gln protonation site's energetic landscape of theoretically derived structures is thoroughly in agreement with measure distribution. While gas phase energetics favor Asn protonation site, solution conditions may contribute to favoring the formation of Gln protonation ions.

Figure C.8 includes the experimental (in red) and theoretical distributions of [L-Vasopressin + H + X]$^{+2}$ (where X is Li or Na). With a lithium charge, a strong shoulder is observed that is less present with sodium. From theoretical structural analysis (Figure C.9), the charges preferentially localize at the ring with both Na and Li cations. The two conformations observed with Li are a result of conformational change of the amino acid tail from a collapsed conformation into an extended conformation. This structural change however is not observed with a Na cation suggesting that the larger cation provides greater stabilization for a closed conformation. This may be due to the larger size of Na cation allowing for stronger interactions with the triamino tail.

3.4 Conclusion

IM-MS structural analysis has been used to demonstrate the potential of developing IM-MS approaches for PEG polymer sequencing and characterizing gas-phase conformational inter-conversion. Unique CCS measurements of PEG oligomers (2-M-10, 4-M-8, and 6-M-6) were a result of differing sodium-PEG chain interactions. The longer PEG chain of the most compact conformation, 2-M-10, retained both sodium cations. Future studies should explore if this sequencing property is unique to PEG subunits or if this approach is applicable to alternative polymer classes.

Two IM-MS distributions were observed for pressinoic acid, suggesting two gas-phase conformations for the ring structure or the presence of protomers. The inter-conversion of ”sliced” peaks suggests conformational change is more likely.

3.5 Acknowledgements

Thank you to Waters for providing access to a cIMS platform to perform tandem IMS experiments.

CHAPTER 4

DEVELOPMENT OF AN IM-MS/MS WORKFLOW TO STUDY NON-COVALENT GUEST-HOST COMPLEXATION STABILITY AND DRUG INCLUSION[1]

4.1 Introduction

Since its isolation in 1972 by Nobel laureate, Tu Youyou, artemisinin has had a long history as a viable antimalarial agent.[191, 192] Artemisinin (ART) is a natural sesquiterpene lactone originally extracted from Artemisia annua, a common herb found in most parts of the world. The endoperoxide bridge in the ART structure (Figure 1A) is a chemically-rare linkage that is essential for its antimalarial activity which rapidly kills nearly all asexual stages of parasite development in the blood, however, to date the precise mechanism of action has remained controversial.[193] Because artemisinin and its derivatives are poorly water-soluble and eliminated rapidly after administration, ART-based combination therapies have become standard delivery systems to help increase therapeutic agent potency and efficacy.[194] Continued advancements in host-guest combination delivery systems of ART have been essential to maintaining potency against the growing number of observed therapeutic agentresistant malaria strains.[195, 196] In addition, there has been growing interest in repurposing the anti-malaria drug for other disease applications, including SARS-CoV-2 and cancer.[197, 198, 199] One of the ART-host complexes of interest and the focus of this study is ART-dextrin therapies.

An approved ingredient in more than 30 different medications, cyclodextrins (CDs) are a family of oligosaccharides consisting of a macrocyclic ring, with the most common natural CDs, α-, β-, and γ-CD containing 6, 7, and 8 glucose subunits, respectively (Figure 1B-D).[200] Due to differing primary and secondary hydroxyl groups on each end of the molecule, CDs are tubular with a larger and smaller opening exposed to the solvent. This arrangement provides and non-hydrophobic interior able to host hydrophobic molecules. Their amphiphilic properties offer the potential for CDs to improve the stability, solubility, and bioavailability of compounds through the formation of host-guest inclusion complexes via hydrophobic and/or polar interactions. The utility of CDs spans broad use cases and has been studied for applications of orally administered medications, cancer treatments, and improving plant bioactive compounds.[201, 202, 203, 204] Specific to ART-dextrin therapeutic combinations, ART inclusion complexes with β- and γ-CD increased the rate and extent of ART absorption in comparison to reference ART preparation.[205] ART encapsulated by βCD increased solubility and inhibited methicillin-resistant Staphylo-coccus aureus (MRSA) bacterial activity by 99.94% after 4 days.[206] More recently, CD derivatives have also been explored to further expand ART so-

---

[1] Parts of this chapter have been adapted from "Noncovalent Host-Guest Complexes of Artemisinin with α-, β-, and γ- Cyclodextrin Examined by Structural Mass Spectrometry Strategies", submitted for publication in *Analytical Chemistry*

lution stability for increased antimicrobial activity upon absorption.[207] Thermal analysis and spectroscopy utilized for ART:CD analysis suggested inclusion complexes with increased thermal stability of ART when in complex verse pure compound.[208]

With a growing focus on host-guest complexes, there has been interest in the advancement of efficient and reliable analytical methods that assist with elucidating host-guest drug complexation. Tandem MS measurements of small molecule-dextrin complexes have been used to compare the stability of gas-phase conformations.[176, 209] Utilizing tandem MS, gas phase ion clusters has been shown to reflect their solution phase stability.[210] In this current study, we offer possible insights to determine host-guest complexes through direct measurements by ion mobility-mass spectrometry (IM-MS). IM is a gas-phase electrophoretic separation technique which discriminates based on differences in ion charge, size, and shape. Coupled with mass spectrometry (MS), IM provides an additional dimension of separation and a molecular descriptor complimenting the MS mass-to-charge measurement differentiation of ions.[211] Gas-phase ion collision cross section (CCS) values can be determined from IM measurements with high CCS reproducibility (relative standard deviations, RSDs, $<$0.3%).[212] The curation and expansion of CCS databases are important steps toward the development of chemical class prediction models and increased identification confidence providing a more detailed description of a molecule or complex.[213, 17]

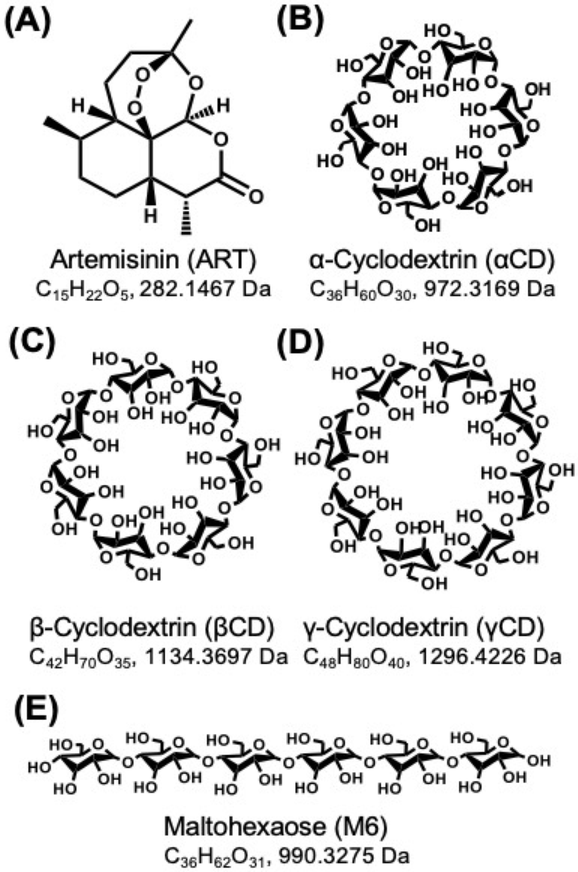

Artemisinin (ART)
$C_{15}H_{22}O_5$, 282.1467 Da

α-Cyclodextrin (αCD)
$C_{36}H_{60}O_{30}$, 972.3169 Da

β-Cyclodextrin (βCD)
$C_{42}H_{70}O_{35}$, 1134.3697 Da

γ-Cyclodextrin (γCD)
$C_{48}H_{80}O_{40}$, 1296.4226 Da

Maltohexaose (M6)
$C_{36}H_{62}O_{31}$, 990.3275 Da

Figure 4.1: Artemisinin and dextrin structures.
Structures of (A) artemisinin (ART) and the oligosaccharides, (B) α-cyclodextrin (α-CD), (C) β-cyclodextrin (β-CD), (D) γ-cyclodextrin (γ-CD), and (E) maltohexaose (M6).

As a structurally selective method, IM-MS techniques can help understand structures of molecular self-assemblies, host-guest complexes, and metallosupramolecular complexes.[214, 215, 216] Based on bioavailability needs, this technique can serve as a high-throughput method to screen guest or host variants effect on solution-phase stability. An IM-MS study by Smith and coworkers demonstrated stereoselective binding of chiral CD derivatives with amino acids through successful amino acid enantiomer differentiation.[68] Few individual studies exist of artemisinin and cyclodextrins explored by IM-MS.[217, 218] This is the first report, of which we are aware, utilizing IM-MS for structural studies of ART:CD combination therapies. In addition to IM-MS measurements, computational modeling has been used to investigate theoretically derived gas-phase structural conformations of molecules using several developed CCS calculation algorithms to interpret the IM-MS derived structural data.[187, 188, 111, 112] Examples of the molecular diversity investigated through a combination of theoretical and IM-MS approaches include small molecules, synthetic polymer isomers, metal complexes, and nonapeptides.[123, 30, 219, 125, 40, 127, 31, 220] High-level theoretical models have been used to model individual CDs with various cations.[221, 222, 223] These studies demonstrate cation preference to orient at the narrower opening of the CD cavity. Therefore, the cation preference for each CD is limited to the size of the narrower opening. Single cation orientation has been shown to remain the same even with drug incorporation such as penicillamine enantiomers encapsulated by βCD.[224]

In this study, we investigate the noncovalent host-guest interactions between α-, β-, γ-CDs, and maltohexaose (M6) with the poorly water-soluble drug artemisinin, by ion mobility-mass spectrometry (IM-MS) analyses, tandem MS/MS, and theoretical modeling approaches. Due to poor ionization in acidic environments, various alkali metal cations were explored as charge carriers to facilitate the ionization and detection of these host-guest complexes. This investigation aims to identify the most stable ART:dextrin arrangement and provide a comprehensive body of work establishing the inclusion and orientation of ART into the CD cavity.

4.2 Experimental Methods

4.2.1 Standards and Chemicals.

Artemisinin (ART), maltohexaose (M6), α-cyclodextrin (αCD), β-cyclodextrin (βCD), and γ-cyclodextrin (γCD) were obtained from Millipore-Sigma. Acetate salts of lithium, sodium, potassium, rubidium, and cesium as well as high purity (Optima Grade) methanol and water were obtained from Fisher Scientific. All chemicals were used as received.

4.2.2 Sample Preparation.

0.01M stock solutions of each dextrin were prepared in water and 0.05M standard stock solutions of ART were prepared in methanol. A volume of 18.8 μL of ART standard stock solution was added to a microcentrifuge tube and dried with nitrogen to evaporate the methanol. After drying, 0.01M dextrin stock solution was added and used to dilute the sample to 1mL. Sample solutions of the four dextrins (αCD, βCD, γCD, and M6) with artemisinin were mixed in a molar ratio of 1:10:10 (artemisinin:dextrin:acetate salt) to a final concentration of 10 μM in 1:9 methanol:water for IM-MS analysis. Varying molar concentrations of sample components, including acetate salt of group I alkali metals (Li, Na, K, Rb, and Cs), solvent compositions (0-100% methanol), sample heating, and filtration were explored. It was found that methanol improved overall signal, with no significant change in the measured CCS values (Figure D.1), however, a minimum amount of methanol (10%) was used for subsequent analyses to assist with ionization while reducing possible solution chemistry alterations. The sample preparation described is based on sample conditions yielding the highest abundance of non-covalently coordinated drug-dextrin complexes.

4.2.3 Instrument Parameters.

Samples were directly infused at 10 μL/min into a thermally assisted electrospray ionization source (ESI, Jet Stream, Agilent Technologies, Santa Clara, CA) coupled to a drift tube ion mobility-quadrupole time-of-flight MS (6560 IM-QTOF, Agilent). The instrument was operated in positive ionization mode, with the QTOF tuned for standard mass range (m/z 50-3200 mode) analysis. ESI source conditions utilized a drying gas temperature of 325 °C and flow rate of 5 L/min. The ion transfer capillary entrance voltage was 3800 V and the focusing nozzle was 2000 V. IM measurements were performed using a uniform field drift tube with either high purity nitrogen or helium drift gas at 4 Torr and an ambient temperature of 300 K. Instrument parameters were adjusted to maximize the transmission of the artemisinin-cyclodextrin complexes, namely a higher trap funnel RF. For trapped ion mobility spectrometry (TIMS) experiments, the samples were infused at a flow rate of 3 μL/min into a Bruker TIMS-TOF Pro (Bruker Daltonics, Bremmen, Germany) fitted with an electrospray ionization source. The samples were ionized using a capillary voltage of 4.2 kV, a nebulizer pressure of 0.5 bar, a drying gas flow rate of 4.0 L/min, and a drying temperature of 150 °C. TIMS measurements were taken over a $1/K_o$ range of 0.72-1.87 $V \times s/cm^2$ with a 900 ms ramp time and a m/z 50-3500 scan range. The TIMS drift gas was nitrogen. Detailed TIMS-TOF instrument parameters are included in Table D6.

4.2.4 Experimental CCS Calculations.

A single-field method derived from first principles theory was used to determine drift tube collision cross section values from the measured ion mobility arrival times as established in an interlaboratory study.[212] Reference CCS values of the tuning mixture obtained in either nitrogen or helium were used for the single-field calibration.[16] Replicate measurements were obtained on separate days and across different sample preparation conditions, which were found to minimally affect the measured IM arrival times. TIMS calibrations were performed using an MS tuning mixture (ESI-L tune mix, Agilent). TIMS ${}^{TR}\mathrm{CCS}_{N_2}$ values were generated via conversion of elution voltage values after calibration.

4.2.5 Tandem MS/MS.

Individual oligosaccharides and oligosaccharides bound to artemisinin were isolated for analysis via IM-MS/MS using the inclusion list feature of the IM-QTOF. The singly and doubly-lithium bound ion forms of both the individual oligosaccharides ($[\mathrm{dextrin} + \mathrm{Li}]^{+}$) and noncovalently coordinated drug-dextrin complexes ($[\mathrm{ART{:}dextrin} + \mathrm{Li}]^{+}$, and $[\mathrm{ART{:}dextrin} + 2\mathrm{Li}]^{+2}$) were quadrupole mass selected with an m/z = 4 isolation window. and subjected to collision-induced dissociation (CID) in the hexapole collision cell (nitrogen) at incremental collision energies ranging from 0 to 35 eV. Energy-resolved fragmentation data was converted to survival yield curves for relative energy comparisons.[225] Survival yield (SY) curves were generated using the following equation,

equation 1. $SY = (I_p/I_0)$

where Ip is the intensity of the precursor ion at a given laboratory voltage and I0 is the intensity at zero laboratory voltage. Plotting the SY as a function of collision energy provides fragmentation curves of precursor ions.

The maximum amount of kinetic energy accessible for conversion to the internal energy of the molecule through a single collision is given by

equation 2. $E_{com} = (m_g/m_g + m_p) * E_{lab}$

Where E_{com} is the center-of-mass energy, mg is the mass of the neutral gas, mp is the mass of the primary ion, and E_{lab} corresponds to the laboratory collision energy. $E_{com_{50}}$ is the center of mass energy where the survival yield is 50%, which is a reflection of the amount of kinetic energy transferred to the internal energy of the primary molecule resulting in 50% dissociation. $E_{com_{50}}$ can be regarded as stability characteristic of a molecule or complex dependent on the structure and noncovalent interactions.[226, 225]

4.2.6 Computational Modeling and Theoretical CCS.

Computational modeling analyses were used to interpret IM-MS structural measurements. The computational studies include two steps: (1) computationally sampling of conformational space and (2) theoretical determination of CCS values for the generated conformations. Insightful atomic-level structural information is attained through inspection of generated conformations that align with experimental CCS values. Many methods exist for both conformational sampling and theoretical determination of CCS values. The computational workflow used here is shown in Figure D.2. Specifically, a geometry optimization at the Hartree-Fock level with a 6-31G* basis set was performed with Gaussian 16 for neutral β-cyclodextrin and artemisinin. Partial charges for each molecule were derived from ab initio electrostatic potential calculations using a 6-31G* basis set. These partial charges were then fitted using the restrained electrostatic potential (RESP) program in AMBER.[227] Cations (Li^+, Na^+, K^+, Rb^+, and Cs^+) are added using AMBER. For each simulation, short energy minimization was performed in AMBER followed by a 10 ps molecular dynamic simulation to heat the molecule to 800 K. Then, a long molecular dynamic simulation was run at 800 K for 9,000 ps. Structural snapshots were saved every 16,667 steps during the simulation, resulting in 3,000 structural snapshots. These high-energy structural snapshots were then cooled to 300 K over 15 ps.[30, 31] MOBCAL software was used for theoretical CCS measurements of the 3,000 resulting conformations. CCS measurements were generated using projection approximation in helium.[115] Due to the large number of theoretical structures generated through the utilized conformational sampling approach, projection approximation is a quick and relatively accurate method for CCS calculations in helium.[111] For MOBCAL, ${}^{PA}\text{CCS}_{He}$ calculations of K^+, Rb^+, and Cs^+, Na^+ parameters were used with appropriate mass components updated for each cation. Na^+ parameters were fitting potentials derived from mobility data by Viehland for Na^+ interactions with helium drift gas.[228] Li^+ parameters were adapted from carbon atomic parameters with appropriate mass components updated for the cation. Theoretical CCS simulations for Li^+, K^+, Rb^+, and Cs^+ are included for a comprehensive cation energetics understanding. The conformational space plots were then overlayed with the experimental ${}^{DT}\text{CCS}_{He}$ values and associated measurement error.

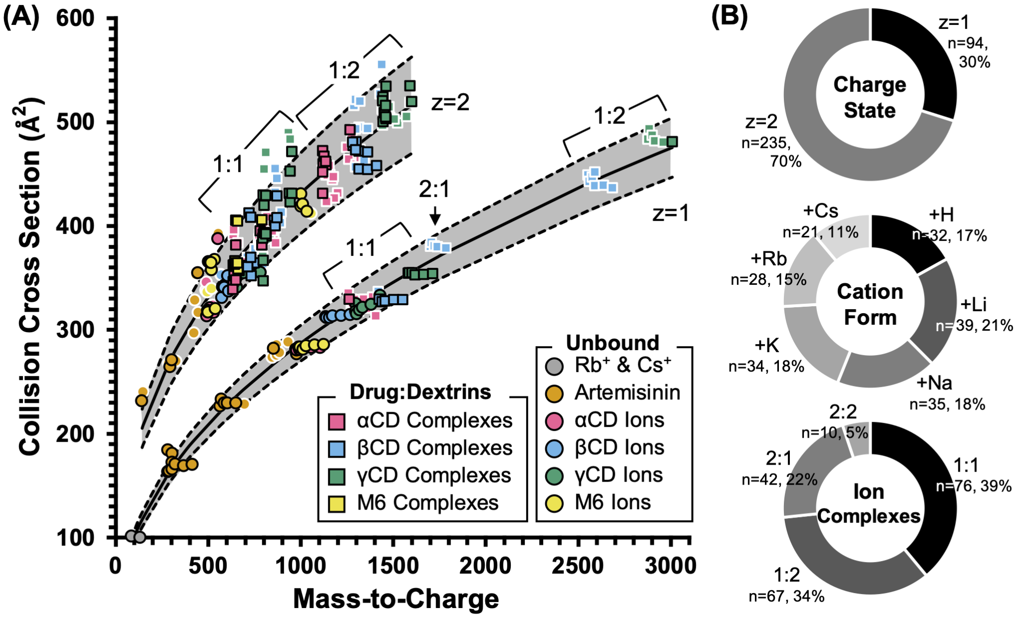

Figure 4.2: CCS space plot and distrubution of ions complexes.

(A) Measured CCS values of artemisinin, oligosaccharides, and their corresponding noncovalent ion complexes. Measurements from low abundance signals (<1,000 counts) are indicated with white outlines. Error bars (n≥3) are within the size of the data points. (B) The distribution of CCS measurements by charge state, cation, and stoichiometry of the ion complexes observed in the spectra.

4.3 Results and Discussion

4.3.1 Ion Detection and CCS Measurements.

Positive mode ESI IM-MS spectra for artemisinin with αCD, βCD, γCD, M6, and lithium acetate are shown in Figures D.3-D.6. Each spectrum is annotated with m/z peaks corresponding to artemisinin and oligosaccharide monomers, dimers, and trimers observed in high abundance across all four samples. The predominate species are unbound analytes, while the bound ART:dextrin complexes appear at 10% of the total abundance. Low ionization efficiency of drug:CD complexes is not uncommon, but seems to vary greatly between drug;CD complexes.[229, 230] Overlapping isobaric signals are prevalent in these datasets and complicate spectral interpretation, however, the empirical charge state trends apparent in IM-MS analysis can be used to confirm molecular assignments. This charge state mapping is shown in the mass-mobility plot in Figure 2A where powerlaw fits to the data (shaded regions) are used to define the empirically observed z=1 and z=2 charge state regions. $^{DT}\mathrm{CCS}_{N_2}$ measurements corresponding to the larger alkali cations, Rb$^+$ and Cs$^+$, are used to constrain the lower bounds of the z=1 power fit. Artifactual signals (such as post-mobility dissociation of noncovalent complexes, shown in Figures D.3-D.6) fall outside of these empirical charge state regions. After filtering these artifactual measurements, the resulting IM-MS analysis yields 327 $^{DT}\mathrm{CCS}_{N_2}$ values (interday $n \geq 3$, av erage n=7.4) of which the majority (72%) exhibited an RSD $\leq 1\%$ (Tables D.1 and D.2). As $^{DT}\mathrm{CCS}_{N_2}$ measurement reproducibly strongly correlates to the ion abundance (Figure D.7), signals below ca. 1,000 counts (RSDs typically $>1\%$) are omitted for further analyses. Higher charge states were observed for unbound dextrins, however, adducts of ART:dextrin complexes of higher charge states were no reproducibility measured within these experiments.

Distribution breakdowns of the $^{DT}\mathrm{CCS}_{N_2}$ measurement survey are included in Figure 2B and individual measurements are tabulated in Tables D.1 and D.2. The most common ion species observed were Li$^+$ coordinated. Among the ART:dextrin complexes, the 1:1 coordinated complexes were most common, whereas 1:2, 2:1, and 2:2 ART:dextrin ions were also present at low abundance (¡0.05% relative abundance, or ¡1,000 counts). As expected, the $^{DT}\mathrm{CCS}_{N_2}$ values characteristically increase with the increasing mass of the analyte. In addition to uniform field $^{DT}\mathrm{CCS}_{N_2}$ measurements, trapped ion mobility spectrometry (TIMS) $^{TR}\mathrm{CCS}_{N_2}$ measurements were collected in this study to corroborate observed complexes. Similar relative ion abundances were observed for ART:βCD complexes between the two IM-MS platforms with an averaged CCS difference of 1.5% (Figure D.8 and Table D.3).

Dextrin	$^{\mathrm{DT}}\mathrm{CCS}_{\mathrm{N2}}$[a]	$^{\mathrm{DT}}\mathrm{CCS}_{\mathrm{N2}}$ of complex[b]	ΔCCS[c]
αCD	280.3 Å^2	329.6 Å^2	16%
βCD	311.8 Å^2	329.8 Å^2	6%
γCD	315.5 Å^2	355.4 Å^2	12%
M6	283.1 Å^2	326.3 Å^2	14%

[a] Lithium-ion form. [b] Oligosaccharide bound to artemisinin. [c] Difference in CCS relative to the averaged value.

Table 4.1: Increase in oligosaccharide CCS upon binding to artemisinin.

A summary of the relative abundances and $^{DT}\text{CCS}_{N_2}$ trends observed for each of the four ART:dextrin complexes (z=1) across different cations is shown in Figure 3. The corresponding ART:CD complexes preferentially formed with Li and Na charge carriers for βCD and αCD, whereas the larger γCD-containing complexes prefer forming with the larger alkali metals, K, Rb, and Cs. In contrast, very weak signals were observed for the drug bound to the linear oligosaccharide, M6, indicating that this complex does not form favorably. Regarding the cation $^{DT}\text{CCS}_{N_2}$ trends, the oligosaccharides exhibited an expected increase in measured $^{DT}\text{CCS}_{N_2}$ that corresponded to the increasing size of the cation. However, $^{DT}\text{CCS}_{N_2}$ trends were not linear but rather showed slight compaction of the $^{DT}\text{CCS}_{N_2}$ value when bound to Li and Na (Figure 3A), which is consistent with what is reported in the literature (Figure D.9) and similarly observed $^{TR}\text{CCS}_{N_2}$ (Figure D.10).[218, 211] In contrast, very little to no increase in measured $^{DT}\text{CCS}_{N_2}$ value with cation size is observed for the 1:1 drug:dextrin complexes (Figure 3B), which suggest similar structures for all complexes irrespective of cation as would be expected from host-guest inclusion complexes. However, this may also result from the cation alone being incorporated into the CD cavity, reducing its contribution to the $^{DT}\text{CCS}_{N_2}$ of the overall complex.[176] While $^{DT}\text{CCS}_{N_2}$ comparisons across the different cations are largely inconclusive, a relative comparison of the change in $^{DT}\text{CCS}_{N_2}$ offers clues as to the structural nature of these complexes. Specifically, for αCD, γCD, and M6, binding to ART increases their $^{DT}\text{CCS}_{N_2}$ values by 12-16%, whereas βCD increases by only 6% when in the ART:dextrin complex form (Table 4.1).

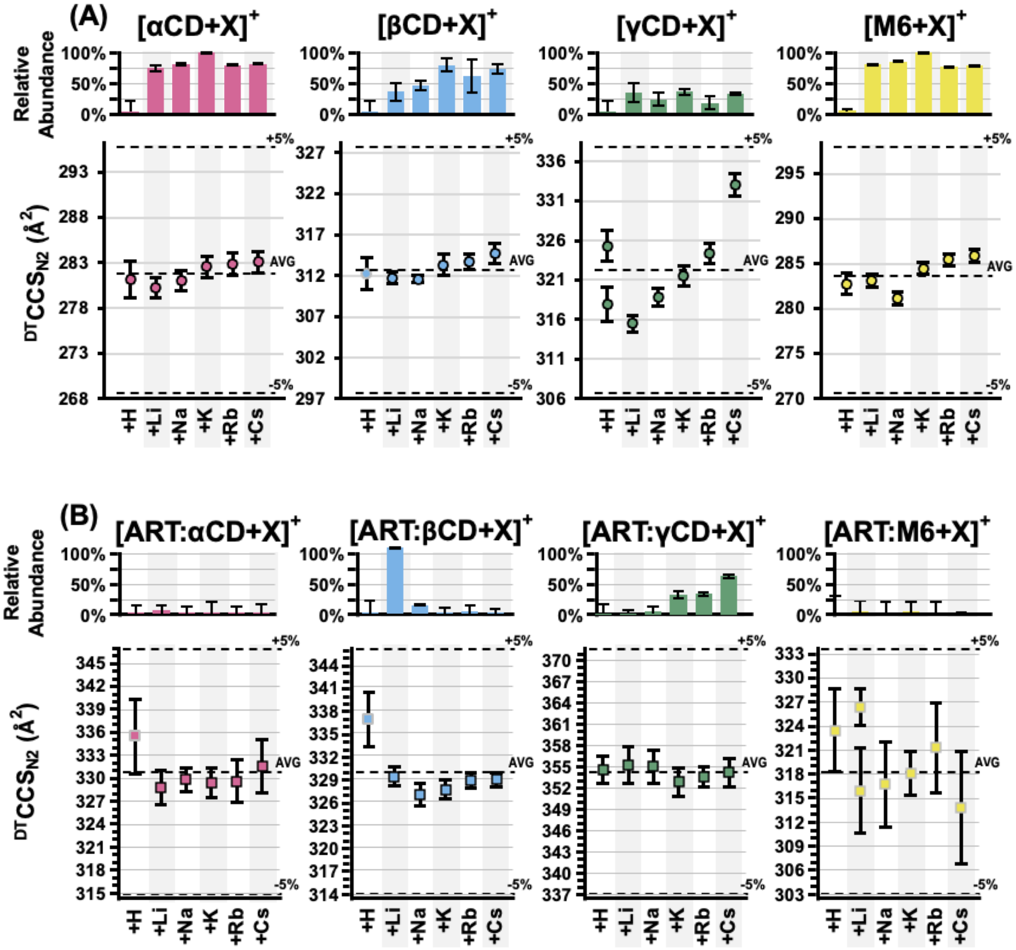

Figure 4.3: Noncovalent complex signal abundances comparison.

(A) Measured CCS values of artemisinin, oligosaccharides, and their corresponding noncovalent ion complexes. Measurements from low abundance signals (<1,000 counts) are indicated with white outlines. Error bars (n≥3) are within the size of the data points. (B) The distribution of CCS measurements by charge state, cation, and stoichiometry of the ion complexes observed in the spectra.

The smaller increase in gas-phase size of the ART:βCD coordination complex is consistent across all cations (Table D.4). This suggests that a more compact gas-phase structure is adopted when ART coordinates with βCD than with the other oligosaccharides investigated. In addition to the smaller than expected gas-phase ^{DT}CCS$_{N_2}$, the ART:βCD complex was also found in significantly higher abundance than the other complexes, notably for the lithium-adducted ion form (Figure 3B). The strong preference for binding to lithium was confirmed in cation competition experiments where the ART and βCD sample was introduced to an equimolar mixture of the alkali metal acetates (Figure D.11), and thus the [ART:βCD + Li]$^+$ ion became a focal point for further investigation.

4.3.2 Tandem MS/MS.

Gas-phase complex stability was investigated through precursor ion survival yield (SY) plots, which have been used in previous host-guest studies to measure the relative binding of noncovalent complexes.[176] Figure D.12 includes tandem MS spectra of [ART:βCD + Na]$^+$ ion. The mobility spectra exhibit two mobility-aligned ion signals which appear after quadrupole isolation (at 25 ms and 40 ms), with the lower drift time ion series exhibiting signal artifacts including nondiagnostic peaks and signals appearing at higher m/z than the precursor. Here, the IM dimension is used to filter out these artifactual signals originating from nonspecific cluster dissociation which allows a more accurate representation of the MS/MS fragment ion abundances. Figure D.13 includes a full spectra of [ART:βCD + Li]$^+$, at 0, 5, and 15 eV. The precursor ion is completely depleted at 15 eV. Precursor fragmentation yields only a single product ion corresponding to cyclodextrin, [βCD + Li]$^+$, indicating that the lithium does not associate with artemisinin. Tandem MS/MS SY curves of the [ART:βCD + X]$^+$ ion (X = H, Li, Na, or K) indicated a decreased stability of the complex in relationship to cation size (Figure D.14). Similar complex stability is observed for z=2 species regardless of cation, [ART:βCD + X]$^{+1}$ ion (X = Li, Na). However, tandem MS/MS breakdown curves of [ART:βCD + 2Na]$^{+2}$ and [ART:βCD + 2Li]$^{+2}$ ions demonstrated the formation of differing secondary ions contingent on charge carrier (Figure D.15). As the [ART:βCD + 2Li]$^{+2}$ ion is fragmented, CD preferentially maintains both lithium charges with no observed [ART + Li]$^+$ species, however, breakdown of [ART:βCD + 2Na]$^{+2}$ forms both [ART + Na]$^+$ and [βCD + Na]$^{+1}$ species. Considering ART has no observed lithium adducts during tandem MS, the lithium-containing complex is interpreted as being more representative of the ART-dextrin interaction stability.

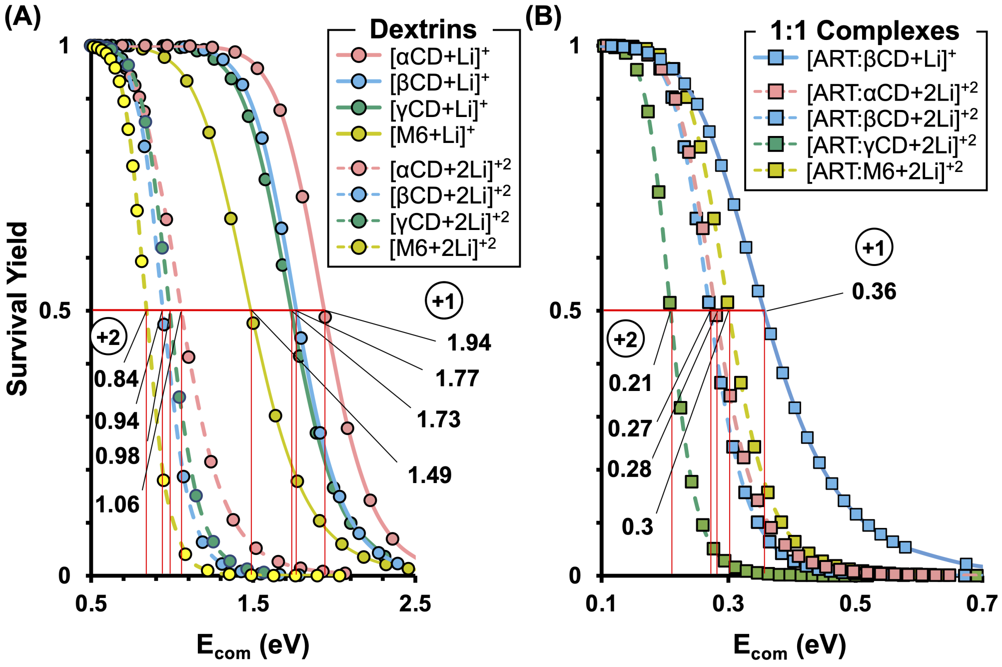

Figure 4.4: Tandem MS/MS SY plots.

Survival yield curves plotted against E_{com} for (A) unbound dextrins, and (B) dextrins complexed with artemisinin. $E_{com_{50}}$ are indicated for each curve.

The low abundance of the 1:1 ART:CD complexes limited direct comparisons of the stability of the singly-charged complexes, however, these CDs exhibit a strong preference for adducting multiple charge carriers, which allowed the doubly charged cation forms ([ART:dextrin + 2Li]$^{+2}$) to be investigated by selected-ion dissociation. Survival yield plots are shown in Figure 4 for the dextrins and the ART:dextrin complexes. Based on the corresponding $E_{com_{50}}$ signal depletion (SY-50 values), the z=1 and z=2 unbound dextrins (Figure 4A) exhibited a gas-phase stability relationship consistent with their relative size (αCD >> βCD > γ CD >> M6), with the small, linear analog (M6) demonstrating the lowest stability. The ART:dextrin (z = 2) complexes (Figure 4B) showed similar breakdown relationship in comparison to unbound dextrins. However, comparable stability was observed between αCD, βCD, and the linear M6, with ART:M6 being the most stable. ART:dextrin stability decreases with increasing dextrin glucose subunits, (M6 > αCD > βCD >> γ CD). Based on these SY plots, the ART inclusion into the cyclodextrin ring is not much more stable than non-specific linear M6 binding. This suggest while ART:CD is an inclusion complex, the depth of ART inclusion within the CDs tubular structure does not completely shield the drug forming a weak interaction. The effect of non-specific electrostatic interactions has been demonstrated as contributing to stabilizing gas-phase ion complexes, which complicates the direct structural interpretation of SY data for indicating the presence of specific analyte inclusion.[231, 232, 233] It is worth noting that [ART:βCD + Li]$^{+1}$ is the only z=1 complex that formed in high abundance suggesting a highly stable complex and therefore indicative of a favored complex formation.

4.3.3 Structural Insight from Theory.

The unbound [artemisinin + X]$^{+}$ and [βCD + X]$^{+}$ ions (X= Li, Na, K, Rb, and Cs) were used to evaluate a theoretical workflow for gaining atomistic structural insights into the gas-phase conformations measured from IM-MS. Drift tube CCS measurements in helium drift gas (^{DT}CCS$_{He}$) have previously demonstrated a good correlation to theory and were subsequently used for comparison to theoretical CCS values obtained from the He-parameterized projection approximation on an ensemble of 3000 energy-minimized structures (Figure D.16, Figure D.17, Table D.5). Results for ART are summarized in Figure D.17 and exhibit good agreement between experiment and theory for the small cations of interest, Li and Na, with values correlating to within 2% for the lowest energy structures. The large cations (K, Rb, Cs) exhibited less agreement with the experimental measurements (5-8%), however, these cations were also not present among the parameterized ions in the original trajectory method and were instead parameterized separately as part of this work. Therefore, some additional disagreement with these larger cations is expected. For βCD (Figure D.17), the CCS of all cation forms exhibited better agreement between experiment and theory (within 2%), despite the lack of good parameters for the larger cations. This more favorable result for βCD suggests that the larger size of βCD relative to artemisinin (1134 Da vs 282 Da) provides a more significant contribution to the measured gas-phase cross section than does the corresponding charge carrier, which serves to minimize the CCS contribution of the charge carrier. Taken together, these initial results provided some indication that the correlation between experiment and theory would be sufficient (within 2%) to structurally interpret the IM-MS measurements of the noncovalent ART:dextrin complexes.

Applying this computational workflow to the noncovalent ART:dextrin ion complexes requires an accurate configuration of the host-guest starting structure as well as placement of the cation. The results are summarized in Figure 5 for ART:βCD with lithium. To allow theory to guide these results, several hypothetical starting structures are constructed with ART restricted to different distances from the center of the βCD cavity (no restriction, 10, and 6 angstroms) without restrictions to the cation to allow motion to different locations of the complex. As the drug molecule is restricted closer to the center of the cyclodextrin, two important observations are noted: (1) the distribution of theoretical structures narrows and shifts to lower CCS, while simultaneously, (2) the relative energies of these predicted structures shift to being more energetically favorable. The lowest-energy structures predict an ART:βCD inclusion complex whereby the theoretical CCS values agree to within a few percent (1-3%) of the empirical CCS measurements. Top- and side-views of the lowest energy structure are shown in Figure 5D and agree with the results of published works investigating βCD with alternative drugs and computational methods.[221, 177] The 5 lowest energy lithium conformations within the experimental measurement deviation are summarized in Figure D.18 and all predict complete artemisinin inclusion into the βCD cavity. Results for the other cations support these findings (Figure D.19). The candidate structures inform two distinct ART orientations for inclusion: one in which artemisinin is positioned with the ketone towards the βCD cavity, whereas the second group of structures predicts the ketone group orients towards the wider opening of the βCD ring. The lithium cation then either positions itself at the smaller opening of the βCD or shares the top opening with the drug molecule. Structures in which the cation occupies the smaller CD opening are the lowest energy and correspond to the results from Yang et al.[224] Additional theoretical results for the double-lithium ion form of the complex ($[\text{ART:}\beta\text{CD + 2Li}]^{+2}$) also correlate well with the experimental CCS measurements and suggest both charge carriers share the wider opening of the cyclodextrin with ART (Figures D.20 and D.21). These doubly coordinated cation systems exhibit prominent ion signals in the IM-MS spectra and appear to be characteristic of CD-containing systems in general (Figure D.22).

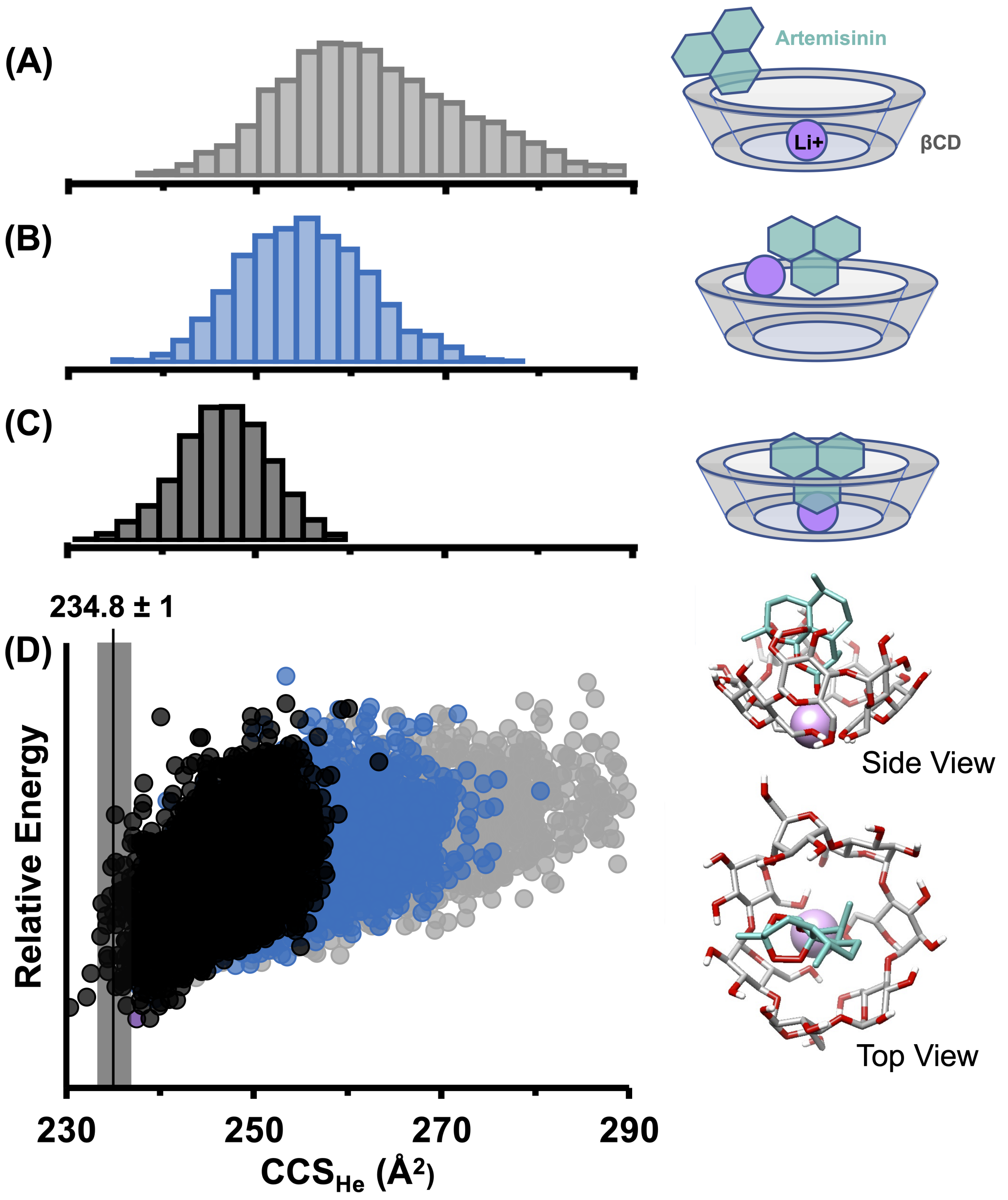

Figure 4.5: Theoretical modeling of [ART:βCD + Li]$^+$
Histogram distribution (bin size = 2 $\AA^2$) of theoretical structures CCS values for [ART:βCD + Li]$^+$ species with (A) no restriction, (B) a 10 angstrom restriction of ART to the center of βCD, and (C) a 6 angstrom restriction of ART to the center of βCD. (D) Conformational space plots of each simulation with experimental CCS overlayed. Top- and side-view of lowest energy structure shown.

4.4 Conclusion

In this investigation, optimal sample preparation and instrument parameterization resulted in the transmission and tentative identification of 1:1-4 and 2:1 ART:CD complexes. Over 300 CCS values with high reproducibility were measured and submitted for addition to the growing Unified CCS Compendium.[17] IM-MS experiments showed that ART:CD complexes preferentially formed with Li and Na charge carriers for α- and βCDs, whereas γCD formation favored larger K, Rb, and Cs cations. Measured abundance and cation competition experiments confirm the preference for the formation of the ART:βCD complex. In general, measured CCS values for the dextrins increased with cation size, whereas the ART:CD complexes tended to express similar CCS values regardless of cation, with the ART:βCD CCS values notably lower than expected based on the other observed changes in CCS upon binding to artemisinin. Tandem MS/MS results for the [ART:βCD + X]$^{+1}$ ion (X = Li, Na, K) showed a decreased stability of the ion complex with increasing cation size, with Li forming the most stable ion complex at reproducibly high abundance. All findings were similarly observed in good agreement on both uniform field drift tube and trapped ion mobility platforms. The computational results for the complexes yielded theoretically generated structures with predicted CCS values in good agreement with empirically measured CCS values in helium drift gas. CCS trends, tandem MS/MS, and corresponding theoretical structures of simulated host-guest complex [ART:βCD + Li]$^{+1}$ were broadly interpreted and suggested complete artemisinin inclusion into the βCD cavity. Similar to published literature, theoretical models show the cation preferentially interacts with the narrower opening of the CD ring, even with the presence of ART. However, through ART inclusion, a second, slightly less energetically favorable orientation was observed where the ART ketone group points away from the CD, This second orientation corresponds to the cation localizing to the wider ring opening and becomes the most energetically favorable structure when the complex accommodates a second cation, which was also the most abundant experimentally measured adduct of the ART:βCD complex. This suggests ART inclusion likely exists in at least two conformational orientations in solution. Collectively, the results from structural measurement of CCS by ion mobility, survival yield curves by tandem MS, and computational modeling point to an inclusion complex for the ART: βCD complex which is retained from solution during transfer to the gas-phase.

4.5 Acknowledgements

Pfizer would like to acknowledge the contributions of Rameez Kagdi and Brandon Showalter. This work was supported in part using the resources of the Center for Innovative Technology at Vanderbilt University and Pfizer, Inc. Financial support for aspects of this work was provided by the National Institutes of Health (NIH R03CA222452), the Vanderbilt University College of Arts and Sciences, the Fisk-Vanderbilt Masters to Ph.D. Bridge program, and Pfizer, Inc.

CHAPTER 5

SUMMARY AND FUTURE DIRECTIONS

5.1 Summary

Metabolites are small molecule intermediates or end products of metabolism with various functions in the body, including fuel, cellular structure and signaling, stimulatory and inhibitory effects on enzymes, and defense. Dysregulation of metabolism through small molecule exposure comes in the forms of environmental factors such as food ingestion, pesticides, and pharmaceutical drugs, which in many cases have been shown through numerous studies to have an internal effect on human metabolism.

Due to speed, sensitivity, and reproducibility, MS has been utilized as prevalent analytical strategy for the quantitative analysis of small molecules ($m/z < 3200$). [234, 235, 236, 237] As an additional molecular descriptor that is easily integrated alongside MS analysis, there has been persistent interest in the development of IM-MS techniques for small molecule analysis. [159, 238] The combination and integrations of many analytical techniques is often necessary for collective coverage and molecule identification confidence. In addition to mass measurement this combined theoretical modeling approach delivers a detailed structural depiction of small molecules and complexes in the gas-phase.

The separation and detection of small molecular isomers and, in particular, enantiomers, pose a fundamental contemporary challenge for chemical analysis techniques. Mass spectrometry methods provide high- throughput and high sensitivity, yet are not selective to isomers. Ion mobility combined with mass spectrometry (IM-MS) provides additional separation capabilities based on chemical structure, but have not demonstrated selectivity to enantiomers. Adapted Figure E.1, highlights the resolving powers necessary for the separation different isomeric classes.[42] While constitutional and cis/trans isomers are within the separation capabilities of next generations IM instrumentation, to date, enantiomers continue to remain out of reach. Even with greater resolving powers, it is yet to be demonstrated if enantiomers are separable using IM alone. In Chapter 2, we demonstrate a straightforward chemical strategy generating stereoselective trinuclear copper complexes which can be used to directly resolve constitutional isomers and enantiomer pairs in mixtures using IM-MS analyses. We illustrate the effectiveness of this noncovalent chemical approach by differentiating between several leucine constitutional isomers as well as (D/L)-amino acid enantiomer pairs. Finally, we explore our empirical findings using structural trend analysis correlated to ion fragmentation data and computational modeling to propose likely structures for these chirally-selective gas-phase complexes. A highly conserved core is imperative for stereoselectivite complexes and informative for refining the utility of trinuclear complexes to differentiating a broad range of analyte enantiomers, such as drug and drug-like compounds.

PEG isomer oligomers (2-M-10, 4-M-8, 6-M-6) and nonapeptides were investigated by dift tube IM-MS, cyclic IM-MS, and theoretical modeling. Our approach to theoretically sampling gas phase conformational space of multiply charge ions is described in Chapter 3. Theoretical structural analysis supported characterization of the gas-phase structural changes contributing IM-MS CCS measurements.

Cyclodextrins (CDs) are a family of macrocyclic oligosaccharides with amphiphilic properties which can improve the stability, solubility, and bioavailability of therapeutic compounds. There has been growing interest in the advancement of efficient and reliable analytical methods that assist with elucidating CD host-guest drug complexation. In Chapter 4, we investigate the non-covalent ion complexes formed between naturally occurring dextrins (αCD, βCD, γCD, and maltohexaose) with the poorly water-soluble anti-malarial drug, artemisinin, using a combination of ion mobility-mass spectrometry (IM-MS), tandem MS/MS, and theoretical modeling approaches. This study aimed to determine if the drug can complex within the core dextrin cavity forming an inclusion complex or nonspecifically binds to the periphery of the dextrins. We explored the use of group I alkali earth metal additives to promote the formation of various noncovalent ion complexes with various drug:dextrin stoichiometries (1:1, 1:2, 1:3, 1:4 and 2:1). Broad IM-MS collision cross section (CCS) mapping ($n>300$) and power-law regression analysis were used to confirm the stoichiometric assignments. The 1:1 drug:αCD and drug:βCD complexes exhibit strong preferences for Li+ and Na+ charge carriers, whereas drug:γCD complexes preferred forming adducts with the larger alkali metals, K^+, Rb^+, and Cs^+. Although the ion measured CCS increased with cation size for the unbound artemisinin and CDs, the 1:1 drug:dextrin complexes exhibit near-identical CCS values regardless of cation, suggesting these are inclusion complexes. Tandem MS/MS survival yield curves of the [artemisinin:βCD + X]$^+$ ion (X = H, Li, Na, K) showed a decreased stability of the ion complex with increasing cation size. Empirical CCS measurements of the [artemisinin:βCD + Li]$^+$ ion correlated with predicted CCS values from the low-energy theoretical structures of the drug incorporated within the βCD cavity, providing further evidence that gas-phase inclusion complexes are formed in these experiments.

Overall, the strategies developed through this work enable the integration of IM CCS measurements and theoretical modeling strategies for structural characterization of gas-phase molecules and complexes. The added structural characterization from integration of IM-MS/MS into small molecule analysis will allow for discrimination of chiral species, relative structural stability trends, and inter-conversion energetics.

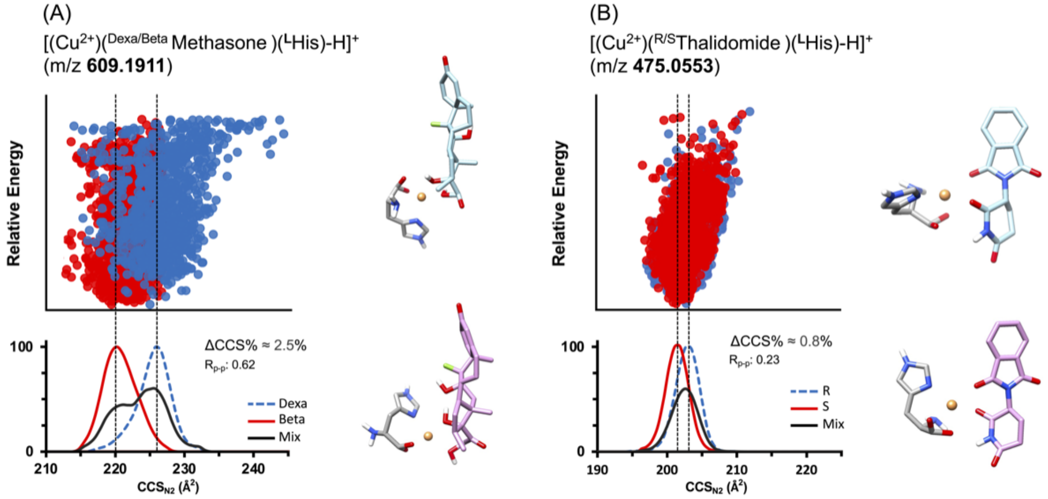

Figure 5.1: Mononuclear copper complexes of drug isomers

IM-MS experimentally measured distributions and theoretical modeling results of mononuclear copper complexes with and L-histidine chiral of (A) dexa/beta-methasone and (B) R/S-thalidomide

5.2 Future Directions

5.2.1 Isomer Separations IM-MS

Trinuclear copper complexes have been demonstrated as an approach for differentiation between AA enantiomers. However, as shown in Figure E.2, the utilization of second generation high-resolving power IM-MS platforms are necessary for baseline separation. Even with the second generation platform, the additional signals from intermixing of enantiomers within the complex complicates data processing.

The formation of trinuclear copper complexes has not been observed by IM-MS with pharmaceutical drugs, most likely due to the larger size of most pharmaceutical drugs in comparison to AAs. Continued enantiomer separation IM-MS experiments primarily target mono- and bi-nuclear copper complexes forming with a single analyte of interest. This simplifies IM-MS measurement interpretation by limiting complex formation with a single enantiomers without the possibility of intermingling. Preliminary findings are shown in Figure 5.1. For dexa/betamethasone and R-/S- thalidomide, the copper-histidine complexing agents stereoselectively interacts with the chiral center resulting in measurable CCS differences between isomers. L-histidine is positioned parallel alongside the drug for the complex contributing to the smaller CCS distributions. For the larger CCS distributions, the copper-histidine core is either positioned perpendicular or extending the length of the drug. The investigations of additional chiral selectors and use of high-resolving power IM-MS instrumentation remain to be explored.

5.2.2 Guest-host Complexation Investigations

The McLean lab and collaborators envision future guest-host complex investigations with CDs to be explored with additional drug molecules that contain varying functional groups utilizing the workflow described in chapter 4. The breakdown curve approach, also used for protein structural stability, currently serves as a means of comparing relative gas-phase stability. How these relative stability curves translate to solution phase thermochemistry remains to be investigated. This may be addressed by utilizing similar complexes with well understood solution phase thermochemistry as tandem MS calibrants. However, identifying similar well studied complexes to utilize as calibrants is a challenge. The combination of IM-MS and theoretical modeling approaches will explore drug inclusions into CD. Theoretical modeling will be insightful as to the specific drug orientations. This would allow for the guiding drug designing in ways that do not alter inclusions orientation/stability.

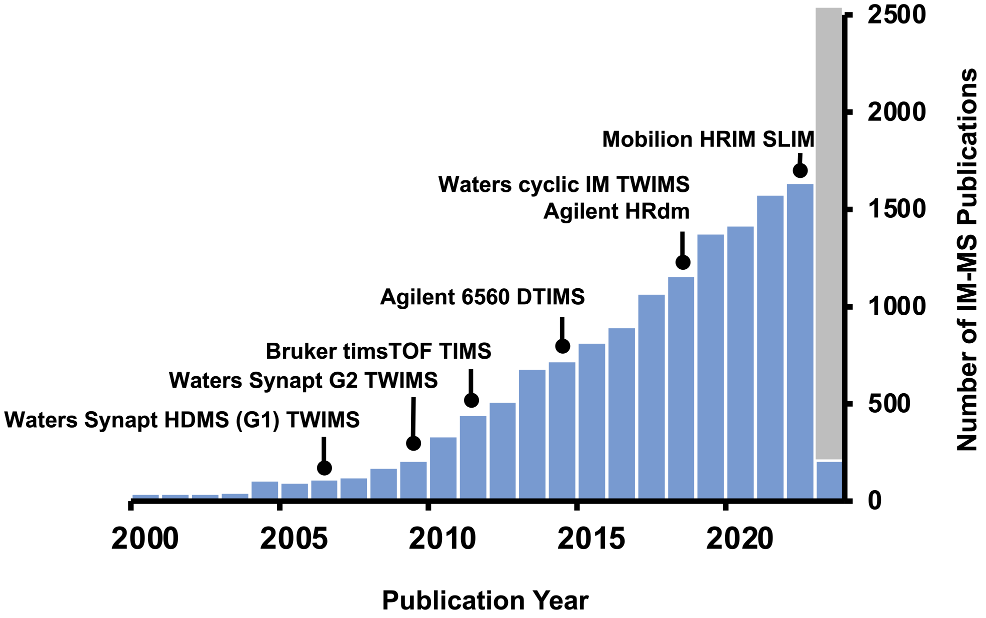

Figure 5.2: ”IM-MS” Publications History

Yearly ”IM-MS” publications count from 2000 to present.

5.3 Concluding Remarks and Outlook

It has been an exciting time to be part of the IM-MS field. Year after year there has been a growing number of publications in the field as shown in, Figure 5.2 which includes the ”IM-MS publication count from 2000 to present. A total of 211, publications were published January 2023. With continuation of that publications rate, projected is an estimated 2500 publications for 2023. Instrument commercialization has also trended alongside increasing number of publications. With mostly proprietary software dependant on the MS platform of the user, MS data processing of small molecules studies is not yet standardized. The addition of IM dimension adds another layer of data complexity that remains for the most part a manual analysis with custom analysis tools. Continued adoption of IM analysis in less niche analytical settings may be catalyzed with the development of streamline data handling software and informatic tools.

The standardization of IM-MS analysis and expansion of CCS databases will help address this challenge of increasing confidence in molecular identifications of untargeted analysis. However, because CCS values are experimentally measured, a limitation of data construction and expansion is the availability of standards. The use of interlaboratory standardization has been fundamental in attaining highly reproducible CCS measurements across many labs. In addition, the exploration of standards-free machine learning approaches to generate predictive models may play an important role in advancing the field. Even with the advancement of everything mentioned above, high confidence in MS feature identifications will continue to pose a contemporary challenge for MS untargeted analysis due to the abundance of small molecule isomers. The exploration of HRIM-MS, alternative drift gas/gas mixtures, and/or solution phase sample additives is an essential step for addressing molecular isomers. It may be that a combination of these approaches are necessary to address this challenge. As of writing this, Bruker, Waters, and Mobilion commercialized second generations HRIM-MS platforms each with a unique approach to achieving high resolution. Important for adoption is the development of structurally inclusive approaches and streamline workflows for isomer detection.

Even more niche, combining theoretical modeling with IM-MS analysis for the structural characterization of gas-phase ions consists of two main phases (1) structural simulation and (2) calculating the CCS of the optimized structure. Computational modeling approaches for completing step 1 have been well established through many years of extensive exploration and development with orthogonal techniques. However, there is not yet a standardized approach for generating gas-phase ions observed by IM-MS. Competing approaches are used to obtain optimized structures depending on research lab (user expertise) or molecular class. For step 2, algorithms for accurate and reproducible CCS calculations of molecules are quite novel. While trajectory method calculations are considered the most accurate, the computational cost limits the utility for large structural data sets. The trade-off with developed alternative high-throughput approaches is that they are optimized for a small subset of chemical classes. Of the developed algorithms for high-throughput analysis, majority of theoretical modeling work has focused on proteins with a less significant focus on small molecule analysis. No one high-throughput CCS calculation package has been extensively optimized with many diverse chemical classes. This would be addressed overtime with continued utilization in theoretical IM-MS studies and expanding body of work. Standardization of theoretical modeling workflows with CCS calculation optimization to meet the field needs can be developed. To-date, a limited number of atoms are properly parameterized for all working algorithms. Proper parameterization to include additional atoms would increase confidence in theoretically investigates of more chemical classes and ion species. At the moment, the theoretical CCS calculations of negative mode species is not accounted for, limiting the utility of theoretical studies to positive mode. A number of molecular classes do not ionize well in positive mode reducing the molecular species that can be studied.

This work described in this dissertation aims to move the field towards greater adoptions of theoretical IM-MS analyses for structural characterization small molecules and complexes they form.

References

[1] Stephen Barnes, H. Paul Benton, Krista Casazza, Sara J. Cooper, Xiangqin Cui, Xiuxia Du, Jeffrey Engler, Janusz H. Kabarowski, Shuzhao Li, Wimal Pathmasiri, Jeevan K. Prasain, Matthew B. Renfrow, and Hemant K. Tiwari. Training in metabolomics research. i. designing the experiment, collecting and extracting samples and generating metabolomics data. *Journal of Mass Spectrometry*, 51(November 2015):461–475, 2016.

[2] Cui Liang, Haitao Lu, and Yie Hou Lee. Challenges and emergent solutions for lc-ms based untargeted metabolomics (invited review, 2nd revision). *Mass spectrometry reviews*, 37(May 2017):772–792, 2018. Untargeted metabolomics challenges.

[3] Sastia Putri and Eiichiro Fukusaki. Metabolomics in a nutshell. *Mass Spectrometry-Based Metabolomics*, page 1–8, 2014.

[4] Brett C. Covington, John A. McLean, and Brian O. Bachmann. Comparative mass spectrometry-based metabolomics strategies for the investigation of microbial secondary metabolites. *Natural Product Reports*, 34(1):6–24, 2017.

[5] Warwick B. Dunn and David I. Ellis. Metabolomics: Current analytical platforms and methodologies. *Trends in Analytical Chemistry*, 24(4):285–294, 2005.

[6] Nathaniel G. Mahieu and Gary J. Patti. Systems-level annotation of a metabolomics data set reduces 25 000 features to fewer than 1000 unique metabolites. *Analytical Chemistry*, 89(19):10397–10406, 2017.

[7] Jody C May and John A McLean. ”ion mobility-mass spectrometry:time-dispersive instrumentation”. *Analytical Chemistry*, 87:1422–1436, 2015.

[8] James N. Dodds and Erin S. Baker. Ion mobility spectrometry: Fundamental concepts, instrumentation, applications, and the road ahead. *Journal of the American Society for Mass Spectrometry*, 30(11):2185–2195, 2019.

[9] Hongli Li, Kevin Giles, Brad Bendiak, Kimberly Kaplan, William F. Siems, and Herbert H. Hill. Resolving structural isomers of monosaccharide methyl glycosides using drift tube and traveling wave ion mobility mass spectrometry. *Analytical Chemistry*, 84(7):3231–3239, 2012.

[10] Matthew F. Bush, Zoe Hall, Kevin Giles, John Hoyes, Carol V. Robinson, and Brandon T. Ruotolo. Collision cross sections of proteins and their complexes: A calibration framework and database for gas-phase structural biology. *Analytical Chemistry*, 82(22):9557–9565, 2010.

[11] Kelly M. Hines, Jody C. May, John A. McLean, and Libin Xu. Evaluation of collision cross section calibrants for structural analysis of lipids by traveling wave ion mobility-mass spectrometry. *Analytical Chemistry*, 88(14):7329–7336, 2016.

[12] Tom W. Knapman, Joshua T. Berryman, Iain Campuzano, Sarah A. Harris, and Alison E. Ashcroft. Considerations in experimental and theoretical collision cross-section measurements of small molecules using travelling wave ion mobility spectrometry-mass spectrometry. *International Journal of Mass Spectrometry*, 298(1–3):17–23, 2010.

[13] Edward A. Mason and Homer W. Schamp. Mobility of gaseous lons in weak electric fields. *Annals of Physics*, 4(3):233–270, 1958.

[14] Cameron N. Naylor, Tobias Reinecke, Mark E. Ridgeway, Melvin A. Park, and Brian H. Clowers. Validation of calibration parameters for trapped ion mobility spectrometry. *Journal of the American Society for Mass Spectrometry*, 30(10):2152–2162, 2019.

[15] Brandon T Ruotolo, Justin L P Benesch, Alan M Sandercock, Suk-Joon Hyung, and Carol V Robinson. Ion mobility-mass spectrometry analysis of large protein complexes. *Nat. Protoc.*, 3(7):1139–1152, 2008.

[16] Caleb B. Morris, Jody C. May, Katrina L. Leaptrot, and John A. McLean. Evaluating separation selectivity and collision cross section measurement reproducibility in helium, nitrogen, argon, and carbon dioxide drift gases for drift tube ion mobility–mass spectrometry. *Journal of The American Society for Mass Spectrometry*, 30(6):1059–1068, 2019.

[17] Jaqueline A. Picache, Bailey S Rose, Andrzej Balinski, Katrina L Leaptrot, Stacy D Sherrod, Jody C May, and John A McLean. Collision cross section compendium to annotate and predict multi-omic compound identities. *Chemical Science*, 10(4):983–993, 2019.

[18] Jody C. May, Caleb B. Morris, and John A. McLean. Ion mobility collision cross section compendium. *Analytical Chemistry*, 89(2):1032–1044, 2017.

[19] Adam B. Hall, Stephen L. Coy, Amol Kafle, James Glick, Erkinjon Nazarov, and Paul Vouros. Extending the dynamic range of the ion trap by differential mobility filtration. *Journal of the American Society for Mass Spectrometry*, 24(9):1428–1436, 2013.

[20] Asiri S. Galhena, Glenn A. Harris, Mark Kwasnik, and Facundo M. Fernández. Enhanced direct ambient analysis by differential mobility-filtered desorption electrospray ionization-mass spectrometry. *Analytical Chemistry*, 82(22):9159–9163, 2010.

[21] Clara L. Feider, Natalia Elizondo, and Livia S. Eberlin. Ambient ionization and faims mass spectrometry for enhanced imaging of multiply charged molecular ions in biological tissues. *Analytical Chemistry*, 88(23):11533–11541, 2016.

[22] Zhidan Chen, Stephen L. Coy, Evan L. Pannkuk, Evagelia C. Laiakis, Albert J. Fornace, and Paul Vouros. Differential mobility spectrometry-mass spectrometry (dms-ms) in radiation biodosimetry: Rapid and high-throughput quantitation of multiple radiation biomarkers in nonhuman primate urine. *Journal of the American Society for Mass Spectrometry*, 29(8):1650–1664, 2018.

[23] Rian L. Griffiths, Alex Dexter, Andrew J. Creese, and Helen J. Cooper. Liquid extraction surface analysis field asymmetric waveform ion mobility spectrometry mass spectrometry for the analysis of dried blood spots. *Analyst*, 140(20):6879–6885, 2015.

[24] Ying Chen Huang, Hsin Hsiang Chung, Ewelina P. Dutkiewicz, Chih Lin Chen, Hua Yi Hsieh, Bo Rong Chen, Ming Yang Wang, and Cheng Chih Hsu. Predicting breast cancer by paper spray ion mobility spectrometry mass spectrometry and machine learning. *Analytical Chemistry*, 92(2):1653–1657, 2020.

[25] Kristin R. McKenna, Li Li, Ramanarayanan Krishnamurthy, Charles L. Liotta, and Facundo M. Fernández. Organic acid shift reagents for the discrimination of carbohydrate isobars by ion mobility-mass spectrometry. *The Analyst*, 2020.

[26] James N. Bull, Neville J.A. Coughlan, and Evan J. Bieske. Protomer-specific photochemistry investigated using ion mobility mass spectrometry. *The Journal of Physical Chemistry A*, 121(32):6021–6027, 2017.

[27] Athula B. Attygalle, Hanxue Xia, and Julius Pavlov. Influence of ionization source conditions on the gas-phase protomer distribution of anilinium and related cations. *Journal of the American Society for Mass Spectrometry*, 28(8):1575–1586, 2017.

[28] Priscila M. Lalli, Bernardo A. Iglesias, Henrique E. Toma, Gilberto F. De Sa, Romeu J. Daroda, Juvenal C. Silva Filho, Jan E. Szulejko, Koiti Araki, and Marcos N. Eberlin. Protomers: Formation, separation and characterization via travelling wave ion mobility mass spectrometry. *Journal of Mass Spectrometry*, 47(6):712–719, 2012.

[29] Jasper Boschmans, Sam Jacobs, Jonathan P. Williams, Martin Palmer, Keith Richardson, Kevin Giles, Cris Lapthorn, Wouter A. Herrebout, Filip Lemière, and Frank Sobott. Combining density functional theory (dft) and collision cross-section (ccs) calculations to analyze the gas-phase behaviour of small molecules and their protonation site isomers. *Analyst*, 141(13):4044–4054, 2016.

[30] Jay G Forsythe, Sarah M Stow, Hartmut Nefzger, Nicholas W Kwiecien, Jody C May, John A McLean, and David M Hercules. Structural characterization of methylenedianiline regioisomers by ion mobility-mass spectrometry, tandem mass spectrometry, and computational strategies: I. electrospray spectra of 2-ring isomers. *Analytical chemistry*, 86(9):4362–4370, 2014.

[31] Sarah M. Stow, Tiffany M. Onifer, Jay G. Forsythe, Hartmut Nefzger, Nicholas W. Kwiecien, Jody C. May, John A. McLean, and David M. Hercules. Structural characterization of methylenedianiline regioisomers by ion mobility-mass spectrometry, tandem mass spectrometry, and computational strategies. 2. electrospray spectra of 3-ring and 4-ring isomers. *Analytical Chemistry*, 87(12):6288–6296, 2015.

[32] Christopher Kune, Cédric Delvaux, Jean R.N. Haler, Loïc Quinton, Gauthier Eppe, Edwin De Pauw, and Johann Far. A mechanistic study of protonated aniline to protonated phenol substitution considering tautomerization by ion mobility mass spectrometry and tandem mass spectrometry. *Journal of the American Society for Mass Spectrometry*, 30(11):2238–2249, 2019.

[33] A. Kaufmann, P. Butcher, K. Maden, S. Walker, and M. Widmer. Does the ion mobility resolving power as provided by commercially available ion mobility quadrupole time-of-flight mass spectrometry instruments permit the unambiguous identification of small molecules in complex matrices? *Analytica Chimica Acta*, 1107:113–126, 2020.

[34] Michael McCullagh, Kevin Giles, Keith Richardson, Sara Stead, and Martin Palmer. Investigations into the performance of travelling wave enabled conventional and cyclic ion mobility systems to characterise protomers of fluoroquinolone antibiotic residues. *Rapid Communications in Mass Spectrometry*, 33(S2):11–21, 2019.

[35] Silas W. Smith. Chiral toxicology: It's the same thing only different. *Toxicological Sciences*, 110(1):4–30, 2009.

[36] Mei Wu, Xiang Jun Zhou, Ryuichi Konno, and Yong Xiang Wang. D-dopa is unidirectionally converted to l-dopa by d-amino acid oxidase, followed by dopa transaminase. *Clinical and Experimental Pharmacology and Physiology*, 33(11):1042–1046, 2006.

[37] Gilbert Mellin and Michael Katzenstein. The saga of thalidomide — neuropathy to embryopathy, with case reports of congenital anomalies. *The New England journal of medicine*, 267(24):1238–1243, 1962.

[38] Steve K. Teo, Wayne A. Colburn, William G. Tracewell, Karin A. Kook, David I. Stirling, Markian S. Jaworsky, Michael A. Scheffler, Steve D. Thomas, and Oscar L. Laskin. Clinical pharmacokinetics of thalidomide. *Clinical Pharmacokinetics*, 43(5):311–327, 2004.

[39] Charles M. Nichols, James N. Dodds, Bailey Rose, Jaqueline A Picache, Caleb B. Morris, Simona G Codreanu, Jody C. May, Stacy D. Sherrod, and John A. McLean. Untargeted molecular discovery in primary metabolism: Collision cross section as a molecular descriptor in ion mobility-mass spectrometry. *Analytical Chemistry*, 90(24):14484–14492, 2018.

[40] Shawn T. Phillips, James N. Dodds, Berkley M. Ellis, Jody C. May, and John A. McLean. Chiral separation of diastereomers of the cyclic nonapeptides vasopressin and desmopressin by uniform field ion mobility mass spectrometry. *Chemical Communications*, 54(1):9398–9401, 2018.

[41] Xueyun Zheng, Noor A. Aly, Yuxuan Zhou, Kevin T. Dupuis, Aivett Bilbao, Vanessa L. Paurus, Daniel J. Orton, Ryan Wilson, Samuel H. Payne, Richard D. Smith, and Erin S. Baker. A structural examination and collision cross section database for over 500 metabolites and xenobiotics using drift tube ion mobility spectrometry. *Chemical Science*, 8(11):7724–7736, 2017.

[42] James N. Dodds, Jody C. May, and John A. McLean. Investigation of the complete suite of the leucine and isoleucine isomers: Toward prediction of ion mobility separation capabilities. *Analytical Chemistry*, 89(1):952–959, 2016.

[43] Arnold Beckett. Chirality and its importance in drug development: A synthetic chemist's perspective. *Biochemical Society Transactions*, 19(2):443–446, 1991.

[44] Timothy J. Ward and Karen D. Ward. Chiral separations: A review of current topics and trends. *Analytical Chemistry*, 84(2):626–635, 2012.

[45] Timothy J Ward and Beth Ann Baker. Chiral separations 2008. *Analytical chemistry*, 80(12):4363–72, 2008.

[46] Jeffrey R. Enders and John A. McLean. Chiral and structural analysis of biomolecules using mass spectrometry and ion mobility-mass spectrometry. *Chirality*, 21:E253–E264, 2009.

[47] C. A. Srebalus Barnes, A. E. Hilderbrand, S. J. Valentine, and D. E. Clemmer. Resolving isomeric peptide mixtures: A combined hplc/ion mobility-tofms analysis of a 4000-component combinatorial library. *Analytical Chemistry*, 74(1):26–36, 2002.

[48] Ching Wu, William F. Siems, and Herbert H. Hill. Secondary electrospray ionization ion mobility spectrometry/mass spectrometry of illicit drugs. *Analytical Chemistry*, 72(2):396–403, 2000.

[49] W. A. Tao, F. C. Gozzo, and R. G. Cooks. Mass spectrometric quantitation of chiral drugs by the kinetic method. *Analytical Chemistry*, 73(8):1692–1698, 2001.

[50] W. Andy Tao, Duxi Zhang, Feng Wang, Peter D. Thomas, and R. Graham Cooks. Kinetic resolution of d,l-amino acids based on gas-phase dissociation of copper(ii) complexes. *Analytical Chemistry*, 71(19):4427–4429, 1999.

[51] Lianming Wu, W. Andy Tao, and R. G. Cooks. Kinetic method for the simultaneous chiral analysis of different amino acids in mixtures. *Journal of Mass Spectrometry*, 38(4):386–393, 2003.

[52] Sangeeta Kumari, Sripadi Prabhakar, Mariappanadar Vairamani, Chebrolu Lavanya Devi, Gunturu Krishna Chaitanya, and Kotamarthi Bhanuprakash. Chiral discrimination of d- and l-amino acids using iodinated tyrosines as chiral references: Effect of iodine substituent. *Journal of the American Society for Mass Spectrometry*, 18(8):1516–1524, 2007.

[53] W. Andy Tao, Rebecca L. Clark, and R. Graham Cooks. Quotient ratio method for quantitative enantiomeric determination by mass spectrometry. *Analytical Chemistry*, 74(15):3783–3789, 2002.

[54] Lianming Wu, Andy W. Tao, and R. Cooks. Ligand and metal-ion effects in metal-ion clusters used for chiral analysis of α-hydroxy acids by the kinetic method. *Analytical and Bioanalytical Chemistry*, 373(7):618–627, 2002.

[55] James N. Dodds, Jody C. May, and John A. McLean. Correlating resolving power, resolution, and collision cross section: Unifying cross-platform assessment of separation efficiency in ion mobility spectrometry. *Analytical Chemistry*, 89(22):12176–12184, 2017.

[56] Virginie Domalain, Marie Hubert-Roux, Vincent Tognetti, Laurent Joubert, Catherine M. Lange, Jacques Rouden, and Carlos Afonso. Enantiomeric differentiation of aromatic amino acids using traveling wave ion mobility-mass spectrometry. *Chem. Sci.*, 5(8):3234–3239, 2014.

[57] Anna R. M. Hyyryläinen, Jaana M. H. Pakarinen, Enik Forró, Ferenc Fülöp, and Pirjo Vainiotalo. Chiral differentiation of some cyclic β -amino acids by kinetic and fixed ligand methods ´ b ferenc f ul ¨ b. *Journal of Mass Spectrometry*, 45:198–204, 2010.

[58] R. Karthikraj, S. Prabhakar, and M. Vairamani. Differentiation of enantiomeric drugs by iodo-substituted l-amino acid references under electrospray ionization mass spectrometric conditions. *Rapid Communications in Mass Spectrometry*, 26(11):1385–1391, 2012.

[59] Axel Mie, Magnus Jörntén-Karlsson, Bengt Olof Axelsson, Andrew Ray, and Curt T. Reimann. Enantiomer separation of amino acids by complexation with chiral reference compounds and high-field asymmetric waveform ion mobility spectrometry: Preliminary results and possible limitations. *Analytical Chemistry*, 79(7):2850–2858, 2007.

[60] Chengyi Xie, Qidi Wu, Shulei Zhang, Chenlu Wang, Wenqing Gao, Jiancheng Yu, and Keqi Tang. Improving glycan isomeric separation via metal ion incorporation for drift tube ion mobility-mass spectrometry. *Talanta*, 211(120719):1–8, 2020.

[61] Xiangying Yu and Z.-P. Yao. Chiral differentiation of amino acids through binuclear copper bound tetramers by ion mobility mass spectrometry. *Analytica Chimica Acta*, 981:62–70, 2017.

[62] Prabha Dwivedi, Ching Wu, Laura M. Matz, Brian H. Clowers, William F. Siems, and Herbert H. Hill. Gas-phase chiral separations by ion mobility spectrometry. *Analytical Chemistry*, 78(24):8200–8206, 2006.

[63] Maíra Fasciotti, Gustavo B. Sanvido, Vanessa G. Santos, Priscila M. Lalli, Michael McCullagh, Gilberto F. De Sá, Romeu J. Daroda, Martin G. Peter, and Marcos N. Eberlin. Separation of isomeric disaccharides by traveling wave ion mobility mass spectrometry using co2 as drift gas. *Journal of Mass Spectrometry*, 47(12):1643–1647, 2012.

[64] Eunji Cho, Eleanor Riches, Martin Palmer, Kevin Giles, Jakub Ujma, and Sunghwan Kim. Isolation of crude oil peaks differing by m/z ~ 0.1 via tandem mass spectrometry using a cyclic ion mobility-mass spectrometer. *Analytical Chemistry*, 91:14268–14274, 2019.

[65] Liulin Deng, Yehia M. Ibrahim, Erin S. Baker, Noor A. Aly, Ahmed M. Hamid, Xing Zhang, Xueyun Zheng, Sandilya V.B. Garimella, Ian K. Webb, Spencer A. Prost, Jeremy A. Sandoval, Randolph V. Norheim, Gordon A. Anderson, Aleksey V. Tolmachev, and Richard D. Smith. Ion mobility separations of isomers based upon long path length structures for lossless ion manipulations combined with mass spectrometry. *ChemistrySelect*, 1(10):2396–2399, 2016.

[66] Thomas Kenderdine, Reza Nemati, Andrew Baker, Martin Palmer, Jakub Ujma, Molly FitzGibbon, Limin Deng, Maksim Royzen, James Langridge, and Daniele Fabris. High-resolution ion mobility spectrometry-mass spectrometry of isomeric/isobaric ribonucleotide variants. *Journal of Mass Spectrometry*, 55(2):1–11, 2020.

[67] Kristin R. McKenna, Li Li, Andrew G. Baker, Jakub Ujma, Ramanarayanan Krishnamurthy, Charles L. Liotta, and Facundo M. Fernández. Carbohydrate isomer resolution: Via multi-site derivatization cyclic ion mobility-mass spectrometry. *Analyst*, 144(24):7220–7226, 2019.

[68] Gabe Nagy, Christopher D. Chouinard, Isaac K. Attah, Ian K. Webb, Sandilya V.B. Garimella, Yehia M. Ibrahim, Erin S. Baker, and Richard D. Smith. Distinguishing enantiomeric amino acids with chiral cyclodextrin adducts and structures for lossless ion manipulations. *Electrophoresis*, 39(24):3148–3155, 2018.

[69] Gabe Nagy, Dusan Veličković, Rosalie K. Chu, Alyssa A. Carrell, David J. Weston, Yehia M. Ibrahim, Christopher R. Anderton, and Richard D. Smith. Towards resolving the spatial metabolome with unambiguous molecular annotations in complex biological systems by coupling mass spectrometry imaging with structures for lossless ion manipulations. *Chemical Communications*, 55(3):306–309, 2019.

[70] Xiangying Yu, Man Chu Chau, Wai Kit Tang, Chi Kit Siu, and Zhong Ping Yao. Self-assembled binuclear cu(ii)-histidine complex for absolute configuration and enantiomeric excess determination of naproxen by tandem mass spectrometry. *Analytical Chemistry*, 90(6):4089–4097, 2018.

[71] Jody C. May and John A. McLean. The influence of drift gas composition on the separation mechanism in traveling wave ion mobility spectrometry: Insight from electrodynamic simulations. *International Journal for Ion Mobility Spectrometry*, 16(2):85–94, 2013.

[72] Eric J. Davis, Prabha Dwivedi, Maggie Tam, William F. Siems, and Herbert H. Hill. High-pressure ion mobility spectrometry. *Analytical Chemistry*, 81(9):3270–3275, 2009.

[73] M. Groessl, S. Graf, and R. Knochenmuss. High resolution ion mobility-mass spectrometry for separation and identification of isomeric lipids. *Analyst*, 140(20):6904–6911, 2015.

[74] Glenn A. Harris, Asiri S. Galhena, and Facundo M. Fernández. Ambient sampling/ionization mass spectrometry: Applications and current trends. *Analytical Chemistry*, 83(12):4508–4538, 2011.

[75] G. Reid Asbury and Herbert H. Hill. Using different drift gases to change separation factors (a) in ion mobility spectrometry. *Analytical Chemistry*, 72(3):580–584, 2000.

[76] Kendra J. Adams, Natalie F. Smith, Cesar E. Ramirez, and Francisco Fernandez-Lima. Discovery and targeted monitoring of polychlorinated biphenyl metabolites in blood plasma using lc-tims-tof ms. *International Journal of Mass Spectrometry*, 427:133–140, 2018.

[77] Anna Baglai, Andrea F.G. Gargano, Jan Jordens, Ynze Mengerink, Maarten Honing, Sjoerd van der Wal, and Peter J. Schoenmakers. Comprehensive lipidomic analysis of human plasma using multidimensional liquid- and gas-phase separations: Two-dimensional liquid chromatography–mass spectrometry vs. liquid chromatography–trapped-ion-mobility–mass spectrometry. *Journal of Chromatography A*, 1530:90–103, 2017.

[78] F. A. Fernandez-Lima, D. A. Kaplan, and M. A. Park. Note: Integration of trapped ion mobility spectrometry with mass spectrometry. *Review of Scientific Instruments*, 82(126106):1–3, 2011.

[79] Elizabeth Kathleen Neumann, Lukasz Migas, Jamie Allen, Richard Caprioli, Raf Van de Plas, and Jeffrey Spraggins. Spatial metabolomics of the human kidney using maldi trapped ion mobility imaging mass spectrometry. *Analytical Chemistry*, page 1–14, 2020.

[80] Mark Schroeder, Sven W. Meyer, Heino M. Heyman, Aiko Barsch, and Lloyd W. Sumner. Generation of a collision cross section library for multi-dimensional plant metabolomics using uhplc-trapped ion mobility-ms/ms. *Metabolites*, 10(13):1–17, 2020.

[81] Jody C. May, Richard Knochenmuss, John C. Fjeldsted, and John A. McLean. Resolution of isomeric mixtures in ion mobility using a combined demultiplexing and peak deconvolution technique. *Analytical Chemistry*, 92:9482–9492, 2020.

[82] Lloyd W. Sumner, Alexander Amberg, Dave Barrett, Michael H. Beale, Richard Beger, Clare A. Daykin, Teresa W.M. Fan, Oliver Fiehn, Royston Goodacre, Julian L. Griffin, Thomas Hankemeier, Nigel Hardy, James Harnly, Richard Higashi, Joachim Kopka, Andrew N. Lane, John C. Lindon, Philip Marriott, Andrew W. Nicholls, Michael D. Reily, John J. Thaden, and Mark R. Viant. Proposed minimum reporting standards for chemical analysis: Chemical analysis working group (cawg) metabolomics standards initiative (msi). *Metabolomics*, 3(3):211–221, 2007.

[83] Alexandra C Schrimpe-rutledge, Simona G Codreanu, Stacy D Sherrod, and John A McLean. Untargeted metabolomics strategies — challenges and emerging directions. *Journal of The American Society for Mass Spectrometry*, 27:1897–1905, 2016.

[84] Vanessa Hinnenkamp, Julia Klein, Sven W. Meckelmann, Peter Balsaa, Torsten C. Schmidt, and Oliver J. Schmitz. Comparison of ccs values determined by traveling wave ion mobility mass spectrometry and drift tube ion mobility mass spectrometry. *Analytical Chemistry*, 90(20):12042–12050, 2018.

[85] Sarah M. Stow, Tim Causon, Xueyun Zheng, Ruwan Thushara Kurulugama, Teresa Mairinger, Jody C. May, Emma E. Rennie, Erin Shammel Baker, Richard D. Smith, John A. McLean, Stephan Hann, and John C. Fjeldsted. An interlaboratory evaluation of drift tube ion mobility - mass spectrometry collision cross section measurements. *Analytical Chemistry*, 89(17):9048–9055, 2017.

[86] Carlos Guijas, J. Rafael Montenegro-Burke, Xavier Domingo-Almenara, Amelia Palermo, Benedikt Warth, Gerrit Hermann, Gunda Koellensperger, Tao Huan, Winnie Uritboonthai, Aries E. Aisporna, Dennis W. Wolan, Mary E. Spilker, H. Paul Benton, and Gary Siuzdak. Metlin: A technology platform for identifying knowns and unknowns. *Analytical Chemistry*, 90(5):3156–3164, 2018.

[87] Colin A Smith, Grace O?? Maille, Elizabeth J Want, Chuan Qin, Sunia A Trauger, Theodore R Brandon, Darlene E Custodio, Ruben Abagyan, and Gary Siuzdak. Metlin. *Therapeutic Drug Monitoring*, 27(6):747–751, 2005.

[88] David S. Wishart, Timothy Jewison, An Chi Guo, Michael Wilson, Craig Knox, Yifeng Liu, Yannick Djoumbou, Rupasri Mandal, Farid Aziat, Edison Dong, Souhaila Bouatra, Igor Sinelnikov, David Arndt, Jianguo Xia, Philip Liu, Faizath Yallou, Trent Bjorndahl, Rolando Perez-Pineiro, Roman Eisner, Felicity Allen, Vanessa Neveu, Russ Greiner, and Augustin Scalbert. Hmdb 3.0-the human metabolome database in 2013. *Nucleic Acids Research*, 41(D1):801–807, 2013.

[89] David S. Wishart, Dan Tzur, Craig Knox, Roman Eisner, An Chi Guo, Nelson Young, Dean Cheng, Kevin Jewell, David Arndt, Summit Sawhney, Chris Fung, Lisa Nikolai, Mike Lewis, Marie Aude Coutouly, Ian Forsythe, Peter Tang, Savita Shrivastava, Kevin Jeroncic, Paul Stothard, Godwin Amegbey, David Block, David D. Hau, James Wagner, Jessica Miniaci, Melisa Clements, Mulu Gebremedhin, Natalie Guo, Ying Zhang, Gavin E. Duggan, Glen D. MacInnis, Alim M. Weljie, Reza Dowlatabadi, Fiona Bamforth, Derrick Clive, Russ Greiner, Liang Li, Tom Marrie, Brian D. Sykes, Hans J. Vogel, and Lori Querengesser. Hmdb: The human metabolome database. *Nucleic Acids Research*, 35(SUPPL. 1):521–526, 2007.

[90] Cody R. Goodwin, Larissa S. Fenn, Dagmara K. Derewacz, Brian O. Bachmann, and John A. McLean. Structural mass spectrometry: Rapid methods for separation and analysis of peptide natural products. *Journal of Natural Products*, 75(1):48–53, 2012.

[91] Kelly M. Hines, Dylan H. Ross, Kimberly L. Davidson, Matthew F. Bush, and Libin Xu. Large-scale structural characterization of drug and drug-like compounds by high-throughput ion mobility-mass spectrometry. *Analytical Chemistry*, 89(17):9023–9030, 2017.

[92] Giuseppe Paglia, Peggi Angel, Jonathan P. Williams, Keith Richardson, Hernando J. Olivos, J. Will Thompson, Lochana Menikarachchi, Steven Lai, Callee Walsh, Arthur Moseley, Robert S. Plumb, David F. Grant, Bernhard O. Palsson, James Langridge, Scott Geromanos, and Giuseppe Astarita. Ion mobility-derived collision cross section as an additional measure for lipid fingerprinting and identification. *Analytical Chemistry*, 87(2):1137–1144, 2015.

[93] Giuseppe Paglia, Jonathan P Williams, Lochana Menikarachchi, J Will Thompson, Richard Tyldesley-worster, Ottar Rolfsson, Arthur Moseley, David Grant, James Langridge, Bernhard O Palsson, and Giuseppe Astarita. Ion mobility derived collision cross sections to support metabolomics applications. 86:3985–3993, 2014.

[94] Laura Righetti, Andreas Bergmann, Gianni Galaverna, Ottar Rolfsson, Giuseppe Paglia, and Chiara Dall'Asta. Ion mobility-derived collision cross section database: Application to mycotoxin analysis. *Analytica Chimica Acta*, 1014:50–57, 2018.

[95] Zhiwei Zhou, Xiaotao Shen, Jia Tu, and Zheng Jiang Zhu. Large-scale prediction of collision cross-section values for metabolites in ion mobility-mass spectrometry. *Analytical Chemistry*, 88(22):11084–11091, 2016.

[96] Valérie Gabelica, Alexandre A. Shvartsburg, Carlos Afonso, Perdita Barran, Justin L.P. Benesch, Christian Bleiholder, Michael T. Bowers, Aivett Bilbao, Matthew F. Bush, J. Larry Campbell, Iain D.G. Campuzano, Tim Causon, Brian H. Clowers, Colin S. Creaser, Edwin De Pauw, Johann Far, Francisco Fernandez-Lima, John C. Fjeldsted, Kevin Giles, Michael Groessl, Christopher J. Hogan, Stephan Hann, Hugh I. Kim, Ruwan T. Kurulugama, Jody C. May, John A. McLean, Kevin Pagel, Keith Richardson, Mark E. Ridgeway, Frédéric Rosu, Frank Sobott, Konstantinos Thalassinos, Stephen J. Valentine, and Thomas Wyttenbach. Recommendations for reporting ion mobility mass spectrometry measurements. *Mass Spectrometry Reviews*, 38(3):291–320, 2019.

[97] Jaqueline A. Picache, Jody C. May, and John A. McLean. Crowd-sourced chemistry: Considerations for building a standardized database to improve omic analyses. *ACS Omega*, 5:980–985, 2020.

[98] Dylan H. Ross, Jang Ho Cho, and Libin Xu. Breaking down structural diversity for comprehensive prediction of ion-neutral collision cross sections. *Analytical Chemistry*, 92(6):4548–4557, 2020.

[99] Jaqueline A. Picache, Jody C. May, and John A. McLean. Chemical class prediction of unknown biomolecules using ion mobility-mass spectrometry and machine learning: Supervised inference of feature taxonomy from ensemble randomization. *Analytical Chemistry*, 92:10759–10767, 2020.

[100] Pier-Luc Plante, Élina Francovic-Fontaine, Jody C. May, John A. McLean, Erin S. Baker, François Laviolette, Mario Marchand, and Jacques Corbeil. Predicting ion mobility collision cross-sections using a deep neural network: Deepccs. *Analytical Chemistry*, 91(8):5191–5199, 2019.

[101] Zhiwei Zhou, Jia Tu, Xin Xiong, Xiaotao Shen, and Zheng Jiang Zhu. Lipidccs: Prediction of collision cross-section values for lipids with high precision to support ion mobility-mass spectrometry-based lipidomics. *Analytical Chemistry*, 89(17):9559–9566, 2017.

[102] Zhiwei Zhou, Xin Xiong, and Zheng Jiang Zhu. Metccs predictor: A web server for predicting collision cross-section values of metabolites in ion mobility-mass spectrometry based metabolomics. *Bioinformatics*, 33(14):2235–2237, 2017.

[103] Pablo Echenique and J. L. Alonso. A mathematical and computational review of hartree-fock scf methods in quantum chemistry. *Molecular Physics*, 105(23–24):3057–3098, 2007.

[104] D. Moncrieff and S. Wilson. On the accuracy of the algebraic approximation in molecular electronic structure calculations: Viii. matrix hartree-fock and many-body perturbation theory applied to a negative molecular ion. *Journal of Physics B: Atomic, Molecular and Optical Physics*, 32(9):2195–2202, 1999.

[105] E. J. Baerends and O. V. Gritsenko. Quantum chemical view of density functional theory. *Journal of Physical Chemistry A*, 101(30):5383–5403, 1997.

[106] Robert G. Parr and Yang Yang Weitao. Density-functional theory. *Oxford University Press*, page 47–69, 1994.

[107] J. W. McIver and A. Komornicki. Rapid geometry optimization for semi-empirical molecular orbital methods. *Chemical Physics Letters*, 10(3):303–306, 1971.

[108] Omar Hamad Shihab Al-Obaidi. Binuclear cu(ii) and co(ii) complexes of tridentate heterocyclic shiff base derived from salicylaldehyde with 4-aminoantipyrine. *Bioinorganic Chemistry and Applications*, 2012:1–7, 2012.

[109] Lianming Wu, Eduardo Cesar Meurer, and R. Graham Cooks. Chiral morphing and enantiomeric quantification in mixtures by mass spectrometry. *Analytical Chemistry*, 76(3):663–671, 2004.

[110] William L. Jorgensen and Julian Tirado-Rives. Monte carlo vs molecular dynamics for conformational sampling. *Journal of Physical Chemistry*, 100(34):14508–14513, 1996.

[111] M. F. Mesleh, J. M. Hunter, A. A. Shvartsburg, G. C. Schatz, and M. F. Jarrold. Structural information from ion mobility measurements: Effects of the long-range potential. *Journal of Physical Chemistry*, 100(40):16082–16086, 1996.

[112] Alexandre A. Shvartsburg, George C. Schatz, and Martin F. Jarrold. Mobilities of carbon cluster ions: Critical importance of the molecular attractive potential. *Journal of Chemical Physics*, 108(6):2416–2423, 1998.

[113] Tianyang Wu, Joseph Derrick, Minal Nahin, Xi Chen, and Carlos Larriba-Andaluz. Optimization of long range potential interaction parameters in ion mobility spectrometry. *Jornal of Chemical Physics*, 148(074102):1–11, 2018.

[114] Alexandre A. Shvartsburg and Martin F. Jarrold. An exact hard-spheres scattering model for the mobilities of polyatomic ions. *Chemical Physics Letters*, 261(1–2):86–91, 1996.

[115] Thomas Wyttenbach, Joseph Batka, Douglas Carlat, and Michael Bowers. Effect of the long-range potential on ion mobility measurements. *American Society for Mass Spectrometry*, 8(3):275–282, 1997.

[116] Christian Bleiholder, Stephanie Contreras, Thanh D Do, and Michael T Bowers. International journal of mass spectrometry a novel projection approximation algorithm for the fast and accurate computation of molecular collision cross sections (ii). model parameterization and definition of empirical shape factors for proteins. *International Journal of Mass Spectrometry*, 345–347:89–96, 2013.

[117] Christian Bleiholder, Thomas Wyttenbach, and Michael T Bowers. International journal of mass spectrometry a novel projection approximation algorithm for the fast and accurate computation of molecular collision cross sections (i). method. *International Journal of Mass Spectrometry*, 308(1):1–10, 2011.

[118] Simon A. Ewing, Micah T. Donor, Jesse W. Wilson, and James S. Prell. Collidoscope: An improved tool for computing collisional cross-sections with the trajectory method. *Journal of the American Society for Mass Spectrometry*, 28(4):587–596, 2017.

[119] Chi Kit Siu, Yuzhu Guo, Irine S. Saminathan, Alan C. Hopkinson, and K. W Michael Siu. Optimization of parameters used in algorithms of ion-mobility calculation for conformational analyses. *Journal of Physical Chemistry B*, 114(2):1204–1212, 2010.

[120] Thomas Wyttenbach, Christian Bleiholder, and Michael T. Bowers. Factors contributing to the collision cross section of polyatomic ions in the kilodalton to gigadalton range: Application to ion mobility measurements. *Analytical Chemistry*, 85(4):2191–2199, 2013.

[121] Timothy M Allison, Perdita Barran, Sarah Cianfe, Matteo T Degiacomi, Rita Grandori, Erik G Marklund, Thomas Menneteau, Lukasz G Migas, Argyris Politis, Michal Sharon, Frank Sobott, Konstantinos Thalassinos, and Justin L P Benesch. Computational strategies and challenges for using native ion mobility mass spectrometry in biophysics and structural biology . 92:10872–10880, 2020.

[122] Cris Lapthorn, Frank S Pullen, Babur Z Chowdhry, Patricia Wright, George L Perkins, and Yanira Heredia. with ion mobility mass spectrometry for ‘ small molecule ’ ion mobility collision cross-sections? †. 140:6814–6823, 2015.

[123] Iain Campuzano, Matthew F. Bush, Carol V. Robinson, Claire Beaumont, Keith Richardson, Hyungjun Kim, and Hugh I. Kim. Structural characterization of drug-like compounds by ion mobility mass spectrometry: Comparison of theoretical and experimentally derived nitrogen collision cross sections. *Analytical Chemistry*, 84(2):1026–1033, 2012.

[124] Tawnya G. Flick, Iain D.G. Campuzano, and Michael D. Bartberger. Structural resolution of 4-substituted proline diastereomers with ion mobility spectrometry via alkali metal ion cationization. *Analytical Chemistry*, 87(6):3300–3307, 2015.

[125] Rachel A. Harris, Jaqueline A. Picache, Ian D. Tomlinson, Emanuel Zlibut, Berkley M. Ellis, Jody C. May, John A. McLean, and David M. Hercules. Mass spectrometry and ion mobility study of poly (ethylene glycol)-based polyurethane oligomers. *Rapid Communications in Mass Spectrometry*, (8662):1–8, 2019.

[126] Dylan H. Ross, Ryan P. Seguin, and Libin Xu. Characterization of the impact of drug metabolism on the gas-phase structures of drugs using ion mobility-mass spectrometry. *Analytical Chemistry*, 91:14498–14507, 2019.

[127] Sarah M. Stow, Cody R. Goodwin, Michal Kliman, Brian O. Bachmann, J. A. McLean, and Terry P. Lybrand. Distance geometry protocol to generate conformations of natural products to structurally interpret ion mobility-mass spectrometry collision cross sections. *Journal of Physical Chemistry B*, 118(48):13812–13820, 2014.

[128] Christopher D. Chouinard, Vinícius Wilian D. Cruzeiro, Christopher R. Beekman, Adrian E. Roitberg, and Richard A. Yost. Investigating differences in gas-phase conformations of 25-hydroxyvitamin d3 sodiated epimers using ion mobility-mass spectrometry and theoretical modeling. *Journal of the American Society for Mass Spectrometry*, 28(8):1497–1505, 2017.

[129] Gary A. Eiceman, Herbert H. Hill, Jr., and Zeev Karpas. Ion mobility spectrometry. *CRC Press LLC*, 3:418, 2013.

[130] Alain Schweitzer, Alfred Fahr, and Werner Niederberger. A simple method for the quantitation of 14c-whole-body autoradiograms. *International Journal of Radiation Applications and Instrumentation. Part*, 38(5):329–333, 1987.

[131] Shelley N. Jackson, Michael Ugarov, Thomas Egan, Jeremy D. Post, Denis Langlais, J. Albert Schultz, and Amina S. Woods. Maldi-ion mohility-tofms imaging of lipids in rat brain tissue. *Journal of Mass Spectrometry*, 42(8):1093–1098, 2007.

[132] John A. McLean, Whitney B. Ridenour, and Richard M. Caprioli. Profiling and imaging of tissues by imaging ion mobility-mass spectrometry. *Journal of Mass Spectrometry*, 42(8):1099–1105, 2007.

[133] Hang Li, Brian K. Smith, László Márk, Peter Nemes, Javad Nazarian, and Akos Vertes. Ambient molecular imaging by laser ablation electrospray ionization mass spectrometry with ion mobility separation. *International Journal of Mass Spectrometry*, 377(1):681–689, 2015.

[134] Jeffrey M. Spraggins, Katerina V. Djambazova, Emilio S. Rivera, Lukasz G. Migas, Elizabeth K. Neumann, Arne Fuetterer, Juergen Suetering, Niels Goedecke, Alice Ly, Raf Van De Plas, and Richard M. Caprioli. High-performance molecular imaging with maldi trapped ion-mobility time-of-flight (timstof) mass spectrometry. *Analytical Chemistry*, 91(22):14552–14560, 2019.

[135] Rachel V. Bennett, Chaminda M. Gamage, Asiri S. Galhena, and Facundo M. Fernández. Contrast-enhanced differential mobility-desorption electrospray ionization-mass spectrometry imaging of biological tissues. *Analytical Chemistry*, 86(8):3756–3763, 2014.

[136] Berkley M. Ellis, Caleb N. Fischer, Leroy B. Martin, Brian O. Bachmann, and John A. McLean. Spatiochemically profiling microbial interactions with membrane scaffolded desorption electrospray ionization-ion mobility-imaging mass spectrometry and unsupervised segmentation. *Analytical Chemistry*, 91(21):13703–13711, 2019.

[137] Margaux Fresnais, Alexander Muck, Marius Majewsky, Britta Statz, Sonja Krausert, Julia Benzel, David Castel, Ludivine Le Dret, Stefan Pfister, Walter E. Haefeli, Jürgen Burhenne, and Rémi Longuespée. Rapid and sensitive drug quantification in tissue sections using matrix assisted laser desorption ionization-ion mobility-mass spectrometry profiling. *Journal of the American Society for Mass Spectrometry*, 31(3):742–751, 2020.

[138] Paul J. Trim, Claire M. Henson, Jennie L. Avery, Andrew McEwen, Marten F. Snel, Emmanuelle Claude, Peter S. Marshall, Andrew West, Alessandra P. Princivalle, and Malcolm R. Clench. Matrix-assisted laser desorption/ionization-ion mobility separation-mass spectrometry imaging of vinblastine in whole body tissue sections. *Analytical Chemistry*, 80(22):8628–8634, 2008.

[139] Christopher D. Chouinard, Michael S. Wei, Christopher R. Beekman, Robin H.J. Kemperman, and Richard A. Yost. Ion mobility in clinical analysis: Current progress and future perspectives. *Clinical Chemistry*, 62(1):124–133, 2016.

[140] Daniel J.C. Berkhout, Hendrik J. Niemarkt, Peter Andriessen, Daniel C. Vijlbrief, Marije K. Bomers, Veerle Cossey, Christian V. Hulzebos, Anton H. Van Kaam, Boris W. Kramer, Richard A. Van Lingen, Alfian N. Wicaksono, James A. Covington, Mirjam M. Van Weissenbruch, Marc A. Benninga, Nanne K.H. De Boer, and Tim G.J. De Meij. Preclinical detection of non-catheter related late-onset sepsis in preterm infants by fecal volatile compounds analysis: A prospective, multi-center cohort study. *Pediatric Infectious Disease Journal*, 39(4):330–335, 2020.

[141] Elina Jokiniitty, Lauri Hokkinen, Pekka Kumpulainen, Yrjö Leskinen, Terho Lehtimäki, Niku Oksala, and Antti Roine. Urine headspace analysis with field asymmetric ion mobility spectrometry for detection of chronic kidney disease. *Biomarkers in Medicine*, 14(8):629–638, 2020.

[142] Tong Sun, Feng Chun Tian, Yu Tian Bi, Xiao Zheng Zhong, Jiao He, Tai Cong Yang, Qing Shan Guo, Ying Lei, Y. Lu, Lin Zeng, and Qing Hua He. Local warning integrated with global feature based on dynamic spectra for faims data analysis in detection of clinical wound infection. *Sensors and Actuators, B: Chemical*, 298, 2019.

[143] Minnie Jacob, Andreas L. Lopata, Majed Dasouki, and Anas M. Abdel Rahman. Metabolomics toward personalized medicine. *Mass Spectrometry Reviews*, 38(3):221–238, 2019.

[144] Charles M Nichols, Jody C May, Stacy D Sherrod, and John A McLean. Automated flow injection method for the high precision determination of drift tube ion mobility collision cross sections. *Analyst*, 143:1556–1559, 2018.

[145] Stacy D Sherrod and John A McLean. Systems-wide high-dimensional data acquisition and informatics using structural mass spectrometry strategies mini-reviews. *Clinical Chemistry*, 62(1):77–83, 2016.

[146] Prabha Dwivedi, Albert J. Schultz, and Herbert H. Hill. Metabolic profiling of human blood by high-resolution ion mobility mass spectrometry (im-ms). *International Journal of Mass Spectrometry*, 298(1–3):78–90, 2010.

[147] Karl Christian Schäfer, Júlia Dénes, Katalin Albrecht, Tamás Szaniszló, Júlia Balogh, Réka Skoumal, Mária Katona, Miklós Tóth, Lajos Balogh, and Zoltán Takáts. In vivo, in situ tissue analysis using rapid evaporative ionization mass spectrometry. *Angewandte Chemie - International Edition*, 48(44):8240–8242, 2009.

[148] Jialing Zhang, John Rector, John Q. Lin, Jonathan H. Young, Marta Sans, Nitesh Katta, Noah Giese, Wendong Yu, Chandandeep Nagi, James Suliburk, Jinsong Liu, Alena Bensussan, Rachel J. Dehoog, Kyana Y. Garza, Benjamin Ludolph, Anna G. Sorace, Anum Syed, Aydin Zahedivash, Thomas E. Milner, and Livia S. Eberlin. Nondestructive tissue analysis for ex vivo and in vivo cancer diagnosis using a handheld mass spectrometry system. *Science Translational Medicine*, 9(406):1–11, 2017.

[149] Beata M. Kolakowski and Zoltán Mester. Review of applications of high-field asymmetric waveform ion mobility spectrometry (faims) and differential mobility spectrometry (dms). *Analyst*, 132(9):842–864, 2007.

[150] Gary A Eiceman, A Tarassov, P Funk, R A Miller, Erkinjon G Nazarov, and E Hughes. Gc-pfaims as smart smoke alarm. identification of combustion sources by patterns of retention time and compensation voltage. *Int. J. Ion Mobil. Spec.*, 5(3):71–75, 2002.

[151] Jordan E. Krechmer, Michael Groessl, Xuan Zhang, Heikki Junninen, Paola Massoli, Andrew T. Lambe, Joel R. Kimmel, Michael J. Cubison, Stephan Graf, Ying Hsuan Lin, Sri H. Budisulistiorini, Haofei Zhang, Jason D. Surratt, Richard Knochenmuss, John T. Jayne, Douglas R. Worsnop, Jose Luis Jimenez, and Manjula R. Canagaratna. Ion mobility spectrometry-mass spectrometry (ims-ms) for on- and offline analysis of atmospheric gas and aerosol species. *Atmospheric Measurement Techniques*, 9(7):3245–3262, 2016.

[152] Sajad Asadi and Bozorgmehr Maddah. Rapid and high-sensitivity determination of phenylarsine oxide in environmental samples by a new technique: Solid-phase microextraction followed by corona discharge ion mobility spectrometry. *Analytical Methods*, 11(47):5969–5975, 2019.

[153] Tangqiang Sun, Di Wang, Yan Tang, Xuebin Xing, Jingcong Zhuang, Jiaxing Cheng, and Zhenxia Du. Fabric-phase sorptive extraction coupled with ion mobility spectrometry for on-site rapid detection of pahs in aquatic environment. *Talanta*, 195(May 2018):109–116, 2019.

[154] Kai Tuovinen, Heikki Paakkanen, and Osmo Hänninen. Detection of pesticides from liquid matrices by ion mobility spectrometry. *Analytica Chimica Acta*, 404(1):7–17, 2000.

[155] Hafid Zaknoun, Marie Josée Binette, and Maggie Tam. Analyzing fentanyl and fentanyl analogues by ion mobility spectrometry. *International Journal for Ion Mobility Spectrometry*, 22(1):1–10, 2019.

[156] Maggie Tam, Chad R. Maheux, Steven Lalonde, and Marie Josée Binette. Unleashing the power from commercial off-the-shelf ion mobility spectrometer. *International Journal for Ion Mobility Spectrometry*, 22(1):11–20, 2019.

[157] Prabha Dwivedi and Herbert H. Hill. A rapid analytical method for hair analysis using ambient pressure ion mobility mass spectrometry with electrospray ionization (esi-imms). *International Journal for Ion Mobility Spectrometry*, 11(1–4):61–69, 2008.

[158] Maykel Hernández-Mesa, Antoine Escourrou, Fabrice Monteau, Bruno Le Bizec, and Gaud Dervilly-Pinel. Current applications and perspectives of ion mobility spectrometry to answer chemical food safety issues. *TrAC - Trends in Analytical Chemistry*, 94:39–53, 2017.

[159] Maykel Hernández-Mesa, David Ropartz, Ana M. García-Campaña, Hélène Rogniaux, Gaud Dervilly-Pinel, and Bruno Le Bizec. Ion mobility spectrometry in food analysis: Principles, current applications and future trends. *Molecules*, 24(15):1–28, 2019.

[160] Zeev Karpas. Applications of ion mobility spectrometry (ims) in the field of foodomics. *Food Research International*, 54(1):1146–1151, 2013.

[161] Wolfgang Vautz, Dunja Zimmerman, Michelle Hartmann, Jörg Ingo Baumbach, Jürgen Nolte, and Johannes Jung. products to cite this version: r p fo r r w on ly. *Food Additive and Contaminants*, 23:1064–1074, 2011.

[162] Christopher A. Browne, Thomas P. Forbes, and Edward Sisco. Detection and identification of sugar alcohol sweeteners by ion mobility spectrometry. *Analytical Methods*, 8(28):5611–5618, 2016.

[163] Jianfeng Wang, Zhongxia Zhang, Zhenxia Du, and Wenjun Sun. Development of a rapid detection method for seven pesticides in cucumber using hollow fibre liquid phase microextraction and ion mobility spectrometry. *Analytical Methods*, 5(23):6592–6597, 2013.

[164] Jin Xiang Wang, Xiao Guang Gao, Jian Jia, Jian Ping Li, and Xiu Li He. Solid phase microextraction-ion mobility spectrometry for rapid determination of trace dichlorovos in tea drinks. *Chinese Journal of Analytical Chemistry*, 43(8):1193–1197, 2015.

[165] Rocío Garrido-Delgado, María Del Mar Dobao-Prieto, Lourdes Arce, and Miguel Valcárcel. Determination of volatile compounds by gc-ims to assign the quality of virgin olive oil. *Food Chemistry*, 187:572–579, 2015.

[166] Shuqi Wang, Haitao Chen, and Baoguo Sun. Recent progress in food flavor analysis using gas chromatography–ion mobility spectrometry (gc–ims). *Food Chemistry*, 315(126158):1–7, 2020.

[167] Xinran Wang, Shupeng Yang, Jinna He, Lanzhen Chen, Jinzhen Zhang, Yue Jin, Jinhui Zhou, and Yongxin Zhang. A green triple-locked strategy based on volatile-compound imaging, chemometrics, and markers to discriminate winter honey and sapium honey using headspace gas chromatography-ion mobility spectrometry. *Food Research International*, 119(January):960–967, 2019.

[168] H. D. Flack. Louis pasteurs discovery of molecular chirality and spontaneous resolution in 1848, together with a complete review of his crystallographic and chemical work. *Acta Crystallographica Section A: Foundations of Crystallography*, 65(5):371–389, 2009.

[169] Michael P. Frank and Robert W. Powers. Simple and rapid quantitative high-performance liquid chromatographic analysis of plasma amino acids. *Journal of Chromatography B: Analytical Technologies in the Biomedical and Life Sciences*, 852(1–2):646–649, 2007.

[170] Luning Sun, Huiwen Jiao, Beibei Gao, Qingyun Yuanzi, Hongwen Zhang, Yongqing Wang, Ning Ou, Zhengyu Yan, and Hongwen Zhou. Hydrophilic interaction liquid chromatography coupled with tandem mass spectrometry method for the simultaneous determination of l -valine, l - l eucine, l -isoleucine, l -phenylalanine, and l -tyrosine in human serum. *Journal of Separation Science*, 38(22):3876–3883, 2015.

[171] Hao Wang, Yvette R. McNeil, Tsin W. Yeo, and Nicholas M. Anstey. Simultaneous determination of multiple amino acids in plasma in critical illness by high performance liquid chromatography with ultraviolet and fluorescence detection. *Journal of Chromatography B: Analytical Technologies in the Biomedical and Life Sciences*, 940:53–58, 2013.

[172] Xiaoli Zhang, Tong Zhao, Ting Cheng, Xiaoyan Liu, and Haixia Zhang. Rapid resolution liquid chromatography (rrlc) analysis of amino acids using pre-column derivatization. *Journal of Chromatography B: Analytical Technologies in the Biomedical and Life Sciences*, 906:91–95, 2012.

[173] Xiaolei Chen, Yu Kang, and Su Zeng. Analysis of stereoisomers of chiral drug by mass spectrometry. *Chirality*, 30(5):609–618, 2018.

[174] Lianming Wu and Frederick G. Vogt. A review of recent advances in mass spectrometric methods for gas-phase chiral analysis of pharmaceutical and biological compounds. *Journal of Pharmaceutical and Biomedical Analysis*, 69:133–147, 2012.

[175] Christopher D. Chouinard, Christopher R. Beekman, Robin H.J. Kemperman, Harrison M. King, and Richard A. Yost. Ion mobility-mass spectrometry separation of steroid structural isomers and epimers. *International Journal for Ion Mobility Spectrometry*, 20(1–2):31–39, 2017.

[176] Yinjuan Chen, Zhicheng Zuo, Xinhua Dai, Peng Xiao, Xiang Fang, Xuefeng Wang, Wenning Wang, and Chuan Fan Ding. Gas-phase complexation of α-/β-cyclodextrin with amino acids studied by ion mobility-mass spectrometry and molecular dynamics simulations. *Talanta*, 186(March):1–7, 2018.

[177] Liancheng Gu, Fangling Wu, Shutong Yang, Fuxing Xu, Xinhua Dai, You Jiang, Xiang Fang, Shaoning Yu, and Chuan Fan Ding. Direct distinction of ibuprofen and flurbiprofen enantiomers by ion mobility mass spectrometry of their ternary complexes with metal cations and cyclodextrins in the gas phase. *Journal of Separation Science*, 44(12):2474–2482, 2021.

[178] Magdalena Zimnicka, Anna Troć, Magdalena Ceborska, Michał Jakubczak, Michał Koliński, and Witold Danikiewicz. Structural elucidation of specific noncovalent association of folic acid with native cyclodextrins using an ion mobility mass spectrometry and theoretical approach. *Analytical Chemistry*, 86(9):4249–4255, 2014.

[179] Christine L. Gatlin, František Tureček, and Tomáš Vaisar. Gas-phase complexes of amino acids with cu(ii) and diimine ligands. part i. aliphatic and aromatic amino acids. *Journal of Mass Spectrometry*, 30(11):1605–1616, 1995.

[180] Milan Remko, Daniel Fitz, Ria Broer, and Bernd Michael Rode. Effect of metal ions (ni 2+, cu 2+ and zn 2+) and water coordination on the structure of l-phenylalanine, l-tyrosine, l-tryptophan and their zwitterionic forms. *Journal of Molecular Modeling*, 17(12):3117–3128, 2011.

[181] Milan Remko, Daniel Fitz, and Bernd Michael Rode. Effect of metal ions (li+, na+, k+, mg2+, ca2+, ni2+, cu2+ and zn 2+) and water coordination on the structure and properties of l-histidine and zwitterionic l-histidine. *Amino Acids*, 39(5):1309–1319, 2010.

[182] Sharon J. Shields, Brian K. Bluhm, and David H. Russell. Fragmentation chemistry of [m + cu]+peptide ions containing an n-terminal arginine. *Journal of the American Society for Mass Spectrometry*, 11(7):626–638, 2000.

[183] Michelle Boone and Peter M.T. Deen. Physiology and pathophysiology of the vasopressin-regulated renal water reabsorption. *Pflugers Archiv European Journal of Physiology*, 456(6):1005–1024, 2008.

[184] Sunnie Myung, Ethan R. Badman, Young Jin Lee, and David E. Clemmer. Structural transitions of electrosprayed ubiquitin ions stored in an ion trap over 10 ms to 30 s. *Journal of Physical Chemistry A*, 106(42):9976–9982, 2002.

[185] Kevin Giles, Jakub Ujma, Jason Wildgoose, Steven Pringle, Keith Richardson, David Langridge, and Martin Green. A cyclic ion mobility-mass spectrometry system. *Analytical Chemistry*, 91(13):8564–8573, 2019.

[186] Jakub Ujma, David Ropartz, Kevin Giles, Keith Richardson, David Langridge, Jason Wildgoose, Martin Green, and Steven Pringle. Cyclic ion mobility mass spectrometry distinguishes anomers and open-ring forms of pentasaccharides. *Journal of the American Society for Mass Spectrometry*, page 1028–1037, 2019.

[187] Stanley E. Anderson, Christian Bleiholder, Erin R. Brocker, Peter J. Stang, and Michael T. Bowers. A novel projection approximation algorithm for the fast and accurate computation of molecular collision cross sections (iii): Application to supramolecular coordination-driven assemblies with complex shapes. *International Journal of Mass Spectrometry*, 330–332:78–84, 2012.

[188] Christian Bleiholder, Stephanie Contreras, and Michael T. Bowers. A novel projection approximation algorithm for the fast and accurate computation of molecular collision cross sections (iv). application to polypeptides. *International Journal of Mass Spectrometry*, 354–355(I):275–280, 2013.

[189] Shannon A. Raab, Tarick J. El-Baba, Arthur Laganowsky, David H. Russell, Stephen J. Valentine, and David E. Clemmer. Protons are fast and smart; proteins are slow and dumb: On the relationship of electrospray ionization charge states and conformations. *Journal of the American Society for Mass Spectrometry*, 32(7):1553–1561, 2021.

[190] Hanxue Xia and Athula B. Attygalle. Untrapping kinetically trapped ions: The role of water vapor and ion-source activation conditions on the gas-phase protomer ratio of benzocaine revealed by ion-mobility mass spectrometry. *Journal of the American Society for Mass Spectrometry*, 28(12):2580–2587, 2017.

[191] Youyou Tu. The discovery of artemisinin (qinghaosu) and gifts from chinese medicine. *Nature Medicine*, 17(10):1217–1220, 2011.

[192] Youyou Tu. Artemisinin—a gift from traditional chinese medicine to the world (nobel lecture). *Angewandte Chemie - International Edition*, 55(35):10210–10226, 2016.

[193] Dorothy H.J. Cheong, Daniel W.S. Tan, Fred W.S. Wong, and Thai Tran. Anti-malarial drug, artemisinin and its derivatives for the treatment of respiratory diseases. *Pharmacological Research*, 158(March):104901, 2020.

[194] Rob W. Van der Pluijm, Chanaki Amaratunga, Mehul Dhorda, and Arjen M. Dondorp. Triple artemisinin-based combination therapies for malaria – a new paradigm? *Trends in Parasitology*, 37(1):15–24, 2021.

[195] Betty Balikagala, Naoyuki Fukuda, Mie Ikeda, Osbert T. Katuro, Shin-Ichiro Tachibana, Masato Yamauchi, Walter Opio, Sakurako Emoto, Denis A. Anywar, Eisaku Kimura, Nirianne M.Q. Palacpac, Emmanuel I. Odongo-Aginya, Martin Ogwang, Toshihiro Horii, and Toshihiro Mita. Evidence of artemisinin-resistant malaria in africa. *New England Journal of Medicine*, 385(13):1163–1171, 2021.

[196] World Health Organization. Artemisinin and artemisinin-based combination therapy resistance. *Who*, (April):1–11, 2017.

[197] Guo Qing Chen, Fahad A. Benthani, Jiao Wu, Deguang Liang, Zhao Xiang Bian, and Xuejun Jiang. Artemisinin compounds sensitize cancer cells to ferroptosis by regulating iron homeostasis. *Cell Death and Differentiation*, 27(1):242–254, 2020.

[198] Fatih M. Uckun, Saran Saund, Hitesh Windlass, and Vuong Trieu. Repurposing anti-malaria phytomedicine artemisinin as a covid-19 drug. *Frontiers in Pharmacology*, 12(March):1–5, 2021.

[199] Yuyong Zhou, Kerry Gilmore, Santseharay Ramirez, Eva Settels, Karen A. Gammeltoft, Long V. Pham, Ulrik Fahnøe, Shan Feng, Anna Offersgaard, Jakob Trimpert, Jens Bukh, Klaus Osterrieder, Judith M. Gottwein, and Peter H. Seeberger. In vitro efficacy of artemisinin-based treatments against sars-cov-2. *Scientific Reports*, 11(1):1–14, 2021.

[200] Alice Gu and Nial J. Wheate. Macrocycles as drug-enhancing excipients in pharmaceutical formulations. *Journal of Inclusion Phenomena and Macrocyclic Chemistry*, 100(1–2):55–69, 2021.

[201] Lorena Almagro and María Ángeles Pedreño. Use of cyclodextrins to improve the production of plant bioactive compounds. *Phytochemistry Reviews*, 19(4):1061–1080, 2020.

[202] Paulo José Salústio, Patrícia Pontes, Claúdia Conduto, Inês Sanches, Catarina Carvalho, João Arrais, and Helena M.Cabral Marques. Advanced technologies for oral controlled release: Cyclodextrins for oral controlled release. *AAPS PharmSciTech*, 12(4):1276–1292, 2011.

[203] Vasanti Suvarna, Parul Gujar, and Manikanta Murahari. Complexation of phytochemicals with cyclodextrin derivatives – an insight. *Biomedicine and Pharmacotherapy*, 88:1122–1144, 2017.

[204] Dongjing Zhang, Pin Lv, Cheng Zhou, Yulin Zhao, Xiali Liao, and Bo Yang. Cyclodextrin-based delivery systems for cancer treatment. *Materials Science and Engineering C*, 96(October 2018):872–886, 2019.

[205] J. W. Wong and K. H. Yuen. Improved oral bioavailability of artemisinin through inclusion complexation with β- and -cyclodextrins. *International Journal of Pharmaceutics*, 227(1–2):177–185, 2001.

[206] Lin Lin, Xuefang Mao, Yanhui Sun, and Haiying Cui. Antibacterial mechanism of artemisinin / beta-cyclodextrins against methicillin-resistant staphylococcus aureus (mrsa). *Microbial Pathogenesis*, 118(February):66–73, 2018.

[207] Yao Hu, David Julian McClements, Xiaojing Li, Long Chen, Jie Long, Aiquan Jiao, Fei Xie, Jinpeng Wang, Zhengyu Jin, and Chao Qiu. Improved art bioactivity by encapsulation within cyclodextrin carboxylate. *Food Chemistry*, 384(October 2021):132429, 2022.

[208] Denisa Circioban, Adriana Ledeti, Gabriela Vlase, Dorina Coricovac, Alina Moaca, Claudia Farcas, Titus Vlase, Ionut Ledeti, and Cristina Dehelean. Guest–host interactions and complex formation for artemisinin with cyclodextrins: instrumental analysis and evaluation of biological activity. *Journal of Thermal Analysis and Calorimetry*, 134(2):1375–1384, 2018.

[209] Jae Ung Lee, Sung Sik Lee, Sungyul Lee, and Han Bin Oh. Noncovalent complexes of cyclodextrin with small organic molecules: Applications and insights into host–guest interactions in the gas phase and condensed phase. *Molecules*, 25(18), 2020.

[210] Papri Chakraborty, Ananya Baksi, Esma Khatun, Abhijit Nag, Atanu Ghosh, and Thalappil Pradeep. Dissociation of gas phase ions of atomically precise silver clusters reflects their solution phase stability. *Journal of Physical Chemistry C*, 121(20):10971–10981, 2017.

[211] Jody C May, Cody R Goodwin, Nichole M Lareau, Katrina L Leaptrot, Caleb B Morris, Ruwan T Kurulugama, Alex Mordehai, Christian Klein, William Barry, Ed Darland, Gregor Overney, Kenneth Imatani, George C Sta, John C Fjeldsted, and John A McLean. Conformational ordering of biomolecules in the gas phase: Nitrogen collision cross sections measured on a prototype high resolution drift tube ion mobility-mass spectrometer. 2014.

[212] Sarah M. Stow, Tim Causon, Xueyun Zheng, Ruwan Thushara Kurulugama, Teresa Mairinger, Jody C. May, Emma E. Rennie, Erin Shammel Baker, Richard D. Smith, John A. McLean, Stephan Hann, and John C. Fjeldsted. An interlaboratory evaluation of drift tube ion mobility - mass spectrometry collision cross section measurements. *Analytical Chemistry*, 89(17):9048–9055, 2017.

[213] Jaqueline A. Picache, Jody C. May, and John A. McLean. Chemical class prediction of unknown biomolecules using ion mobility-mass spectrometry and machine learning: Supervised inference of feature taxonomy from ensemble randomization. *Analytical Chemistry*, 92:10759–10767, 2020.

[214] Elina Kalenius, Michael Groessl, and Kari Rissanen. Ion mobility–mass spectrometry of supramolecular complexes and assemblies. *Nature Reviews Chemistry*, 3(1):4–14, 2019.

[215] Ina D. Kellner, Marc S. Von Gernler, Manolis D. Tzirakis, Michael Orfanopoulos, and Thomas Drewello. The influence of alkali metal cation size on the formation and dissociation of crown ether fullerene dimers in electrospray mass spectrometry. *Journal of Physical Chemistry C*, 120(1):786–792, 2016.

[216] Damilola S. Oluwatoba, Md Faizul Islam, Bozumeh Som, Ammon J. Sindt, Mark D. Smith, Linda S. Shimizu, and Thanh D. Do. Evaluating the effects of metal adduction and charge isomerism on ion-mobility measurements using m-xylene macrocycles as models. *Journal of the American Society for Mass Spectrometry*, 33(5):840–850, 2022.

[217] Glenn A. Harris, Stephan Graf, Richard Knochenmuss, and Facundo M. Fernández. Coupling laser ablation/desorption electrospray ionization to atmospheric pressure drift tube ion mobility spectrometry for the screening of antimalarial drug quality. *Analyst*, 137(13):3039–3044, 2012.

[218] Christian Klein, Stephanie M. Cologna, Ruwan T. Kurulugama, Paul S. Blank, Ed Darland, Alex Mordehai, Peter S. Backlund, and Alfred L. Yergey. Cyclodextrin and malto-dextrose collision cross sections determined in a drift tube ion mobility mass spectrometer using nitrogen bath gas. *Analyst*, 143(17):4147–4154, 2018.

[219] Brett Harper, Elizabeth K Neumann, Sarah M Stow, Jody C May, John A McLean, and Touradj Solouki. Analytica chimica acta determination of ion mobility collision cross sections for unresolved isomeric mixtures using tandem mass spectrometry and chemometric deconvolution. *Analytica Chimica Acta*, 939:64–72, 2016.

[220] Emanuel Zlibut, Jody C May, and John A McLean. Enantiomer differentiation of amino acid stereoisomers by structural mass spectrometry using noncovalent trinuclear copper complexes. *Journal of the American Society for Mass Spectrometry*, 33(6):996–1002, 2022.

[221] S. E. Angelova, V. K. Nikolova, and T. M. Dudev. Determinants of the host-guest interactions between α-, β- and -cyclodextrins and group ia, iia and iiia metal cations: A dft/pcm study. *Physical Chemistry Chemical Physics*, 19(23):15129–15136, 2017.

[222] Francisco Gámez, Paola Hurtado, Ana R. Hortal, Bruno Martínez-Haya, Giel Berden, and Jos Oomens. Cations in a molecular funnel: Vibrational spectroscopy of isolated cyclodextrin complexes with alkali metals. *ChemPhysChem*, 14(2):400–407, 2013.

[223] Anna Stachowicz, Anna Styrcz, Jacek Korchowiec, Ali Modaressi, and Marek Rogalski. Dft studies of cation binding by β-cyclodextrin. *Theoretical Chemistry Accounts*, 130(4–6):939–953, 2011.

[224] Shutong Yang, Fangling Wu, Fanzhen Yu, Liancheng Gu, Huanhuan Wang, Yiyi Liu, Yanqiu Chu, Fengyan Wang, Xiang Fang, and Chuan Fan Ding. Distinction of chiral penicillamine using metal-ion coupled cyclodextrin complex as chiral selector by trapped ion mobility-mass spectrometry and a structure investigation of the complexes. *Analytica Chimica Acta*, 1184:339017, 2021.

[225] Tzipporah M. Kertesz, Lowell H. Hall, Dennis W. Hill, and David F. Grant. Ce50: Quantifying collision induced dissociation energy for small molecule characterization and identification. *Journal of the American Society for Mass Spectrometry*, 20(9):1759–1767, 2009.

[226] Dennis W. Hill, Clive L. Baveghems, Daniel R. Albaugh, Tzipporah M. Kormos, Steven Lai, Hank K. Ng, and David F. Grant. Correlation of ecom 50 values between mass spectrometers: Effect of collision cell radiofrequency voltage on calculated survival yield. *Rapid Communications in Mass Spectrometry*, 26(19):2303–2310, 2012.

[227] Christopher I. Bayly, Piotr Cieplak, Wendy D. Cornell, and Peter A. Kollman. A well-behaved electrostatic potential based method using charge restraints for deriving atomic charges: The resp model. *Journal of Physical Chemistry*, 97(40):10269–10280, 1993.

[228] L.A. Viehland. Interaction potentials for the alkali ion-rare-gas systems. *Chemical Physics*, 85:291–304, 1983.

[229] Mihaela Silion, Adrian Fifere, Ana Lacramioara Lungoci, Narcisa Laura Marangoci, Sorin Alexandru Ibanescu, Radu Zonda, Alexandru Rotaru, and Mariana Pinteală. Mass spectrometry as a complementary approach for noncovalently bound complexes based on cyclodextrins. *Advances in experimental medicine and biology*, 1140:685–701, 2019.

[230] Jian Qiang Zhang, Kun Ming Jiang, Kun An, Si Hao Ren, Xiao Guang Xie, Yi Jin, and Jun Lin. Novel water-soluble fisetin/cyclodextrins inclusion complexes: Preparation, characterization, molecular docking and bioavailability. *Carbohydrate Research*, 418:20–28, 2015.

[231] Konstantin Barylyuk, Roman M. Balabin, Dan Grünstein, Raghavendra Kikkeri, Vladimir Frankevich, Peter H. Seeberger, and Renato Zenobi. What happens to hydrophobic interactions during transfer from the solution to the gas phase? the case of electrospray-based soft ionization methods. *Journal of the American Society for Mass Spectrometry*, 22(7):1167–1177, 2011.

[232] John B. Cunniff and Paul Vouros. False positives and the detection of cyclodextrin inclusion complexes by electrospray mass spectrometry. *Journal of the American Society for Mass Spectrometry*, 6(5):437–447, 1995.

[233] Valérie Gabelica, Nives Galic, and Edwin De Pauw. On the specificity of cyclodextrin complexes detected by electrospray mass spectrometry. *Journal of the American Society for Mass Spectrometry*, 13(8):946–953, 2002.

[234] Bin Zhou, Jun Feng Xiao, Leepika Tuli, and Habtom W. Ressom. Lc-ms-based metabolomics. *Molecular BioSystems*, 8(2):470–481, 2012.

[235] Tobias Kind and Oliver Fiehn. Advances in structure elucidation of small molecules using mass spectrometry. *Bioanalytical Reviews*, 2(1):23–60, 2010.

[236] Wenkui Li and Francis L.S. Tse. Dried blood spot sampling in combination with lc-ms/ms for quantitative analysis of small molecules. *Biomedical Chromatography*, 24(1):49–65, 2010.

[237] Caroline Bylda, Roland Thiele, Uwe Kobold, and Dietrich A. Volmer. Recent advances in sample preparation techniques to overcome difficulties encountered during quantitative analysis of small molecules from biofluids using lc-ms/ms. *Analyst*, 139(10):2265–2276, 2014.

[238] Giuseppe Paglia, Andrew J. Smith, and Giuseppe Astarita. Ion mobility mass spectrometry in the omics era: Challenges and opportunities for metabolomics and lipidomics. *Mass Spectrometry Reviews*, (January), 2021.

Appendix A

Reference of Adaption for Chapters

Chapter 1. **Zlibut, E.**; Leaptrot, K. L.; May, J. C.; McLean, J. A. CHAPTER 12. Ion Mobility–Mass Spectrometry in Metabolomics Studies. 2021, 307–335. https://doi.org/10.1039/9781839162886-00307.

Chapter 2. **Zlibut, E.**; May, J. C.; McLean, J. A. Enantiomer Differentiation of Amino Acid Stereoisomers by Structural Mass Spectrometry Using Noncovalent Trinuclear Copper Complexes. J. Am. Soc. Mass Spectrom. 2022, 33 (6), 996–1002. https://doi.org/10.1021/jasms.2c00059.

Chapter 3. Harris, R.A., Picache, J.A., Tomlinson, I.D., **Zlibut, E.**, Berkley E.M., May, J.C., McLean, J.A. Hercules, D.M. (2019). Mass Spectrometry and Ion Mobility Study of Poly(ethylene glycol)-based Polyurethane Oligomers.

Chapter 4. **Zlibut, E.**; May, J. C.; Wei, Y,: Gessmann, D.; Wood, C.S.; Bernat, B.A., Pugh, T. E.; Palmer-Jones, L.; Cosquer, R. P.; Dybeck, E.; McLean, J. A. Noncovalent Host-Guest complexes of artemisinin with α-, β-, and γ-Cyclodextrin Examined with Structural Mass Spectrometry Strategies. Analytical Chemistry. *Submitted September 2022*

Appendix B

Supplemental Material Chapter 2

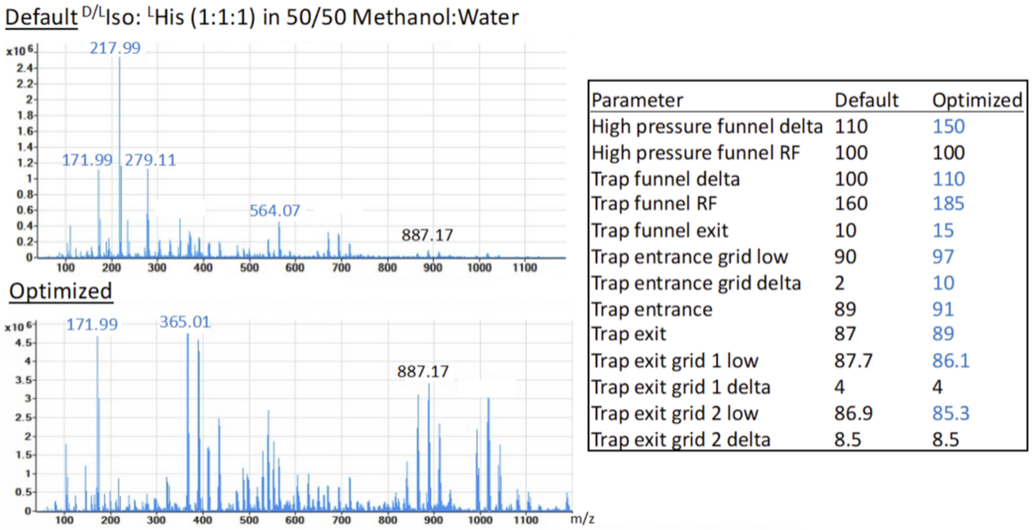

Parameter	Default	Optimized
High pressure funnel delta	110	150
High pressure funnel RF	100	100
Trap funnel delta	100	110
Trap funnel RF	160	185
Trap funnel exit	10	15
Trap entrance grid low	90	97
Trap entrance grid delta	2	10
Trap entrance	89	91
Trap exit	87	89
Trap exit grid 1 low	87.7	86.1
Trap exit grid 1 delta	4	4
Trap exit grid 2 low	86.9	85.3
Trap exit grid 2 delta	8.5	8.5

Figure B.1: Transmission and survivability of complexes using optimized and default instrument parameters. Default and optimized parameters are listed in table.

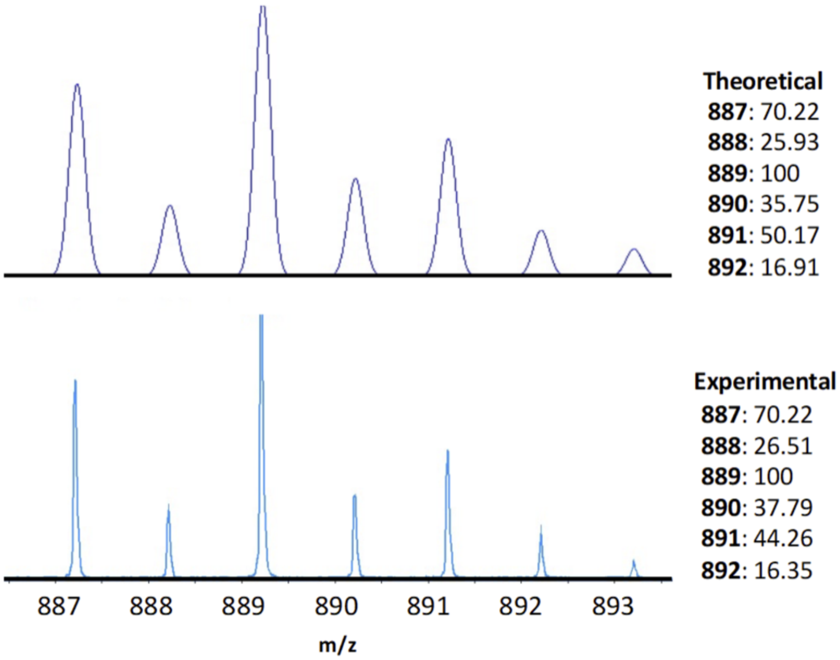

Figure B.2: Theoretical and experimental MS isotope distributions with percent abundance.

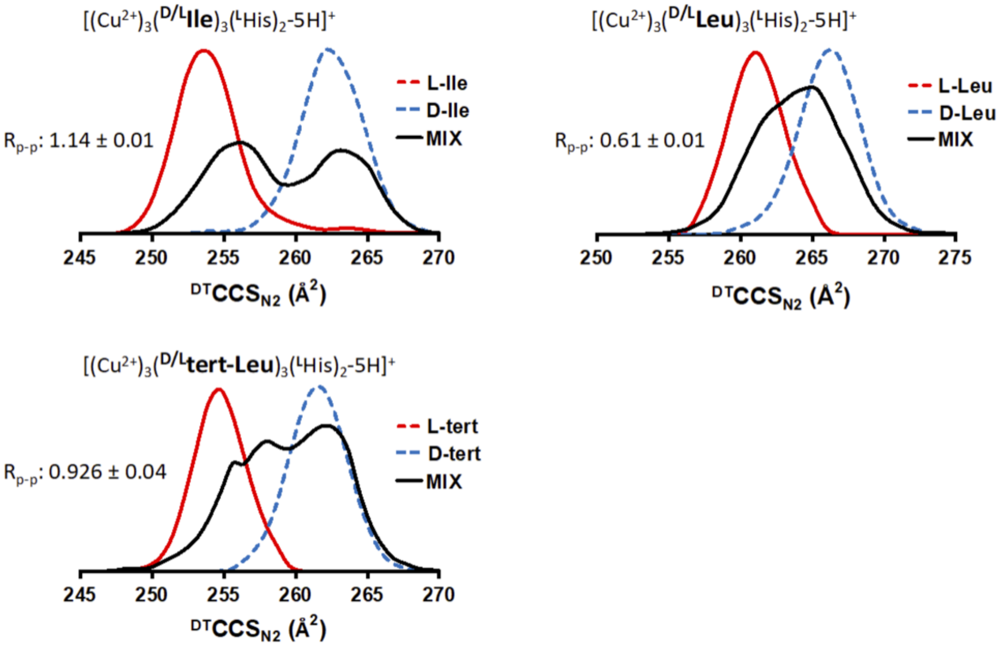

$[(Cu^{2+})_3(^{D/L}\mathbf{Ile})_3(^{L}His)_2\text{-}5H]^+$

$[(Cu^{2+})_3(^{D/L}\mathbf{Leu})_3(^{L}His)_2\text{-}5H]^+$

$[(Cu^{2+})_3(^{D/L}\mathbf{tert\text{-}Leu})_3(^{L}His)_2\text{-}5H]^+$

Figure B.3: Theoretical and experimental MS isotope distributions with percent abundance.

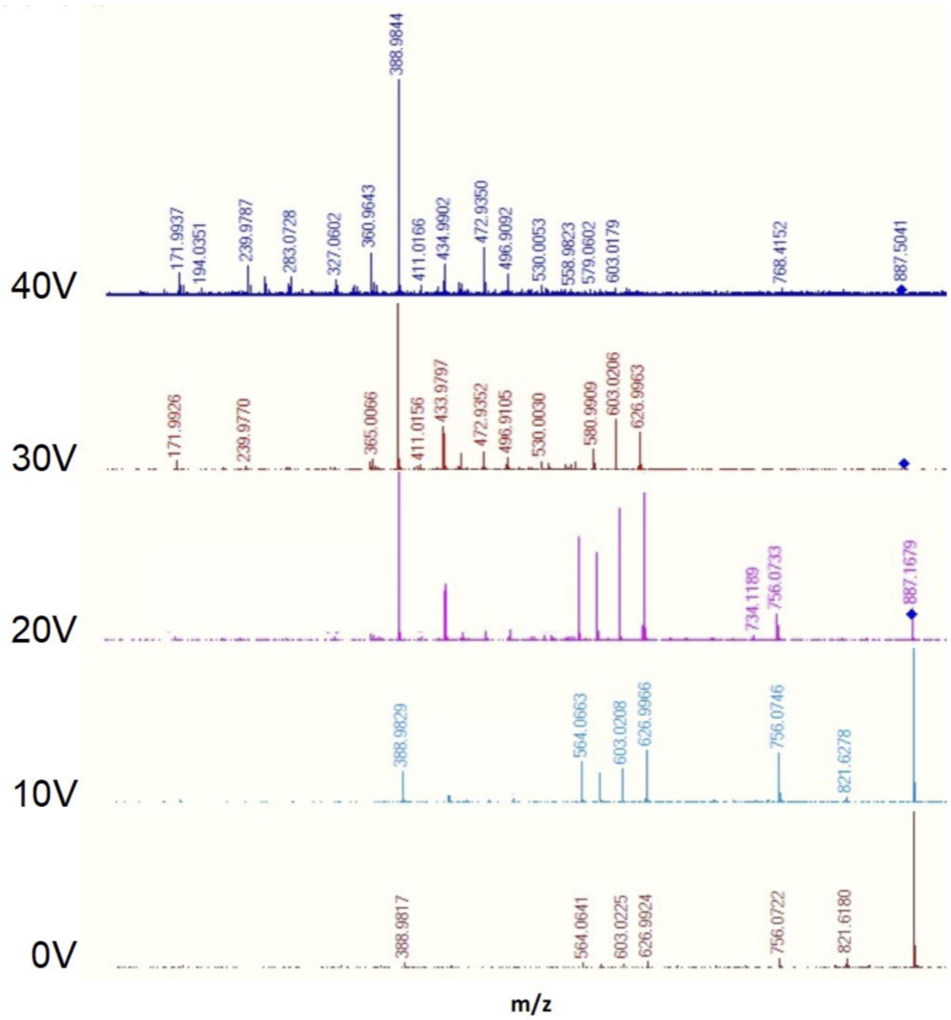

Figure B.4: Mass-selected ion fragmentation (MS^2) spectra of the isoleucine trinuclear copper complex with L-histidine CS ($[(Cu^{2+})_3(Ile)_3(^L His)_2+5H]^+$, m/z 887) using laboratory frame collision voltages from 0V to 40V in 10V increments.

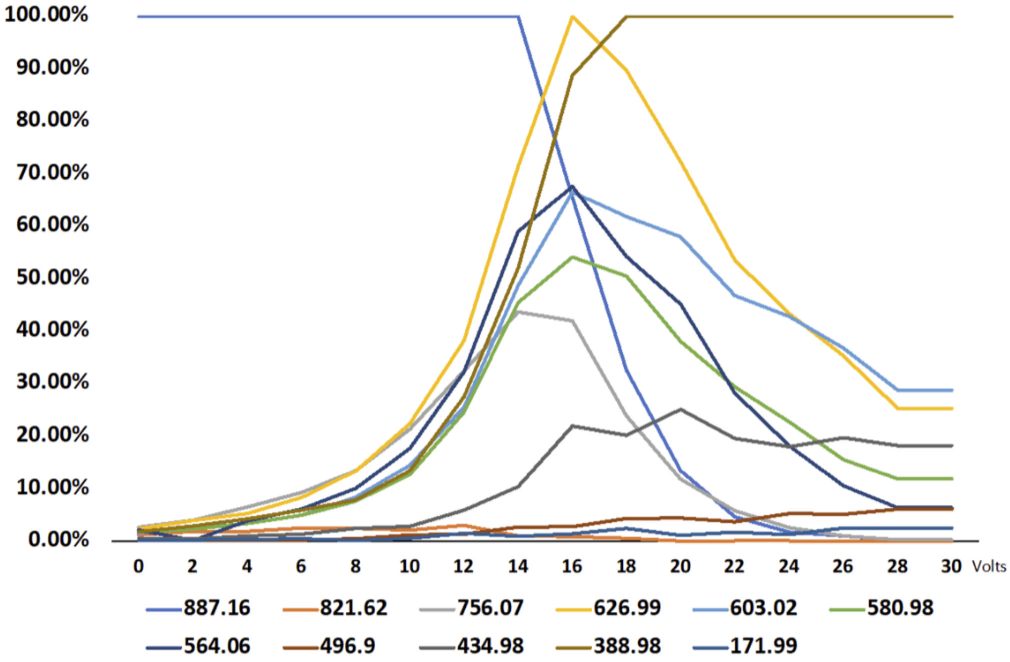

Figure B.5: Ion breakdown curves of the isoleucine trinuclear copper complex with L- histidine CS ($[(Cu^{2+})_3(Ile)_3(^{L}His)_2+5H]^+$, m/z 887).

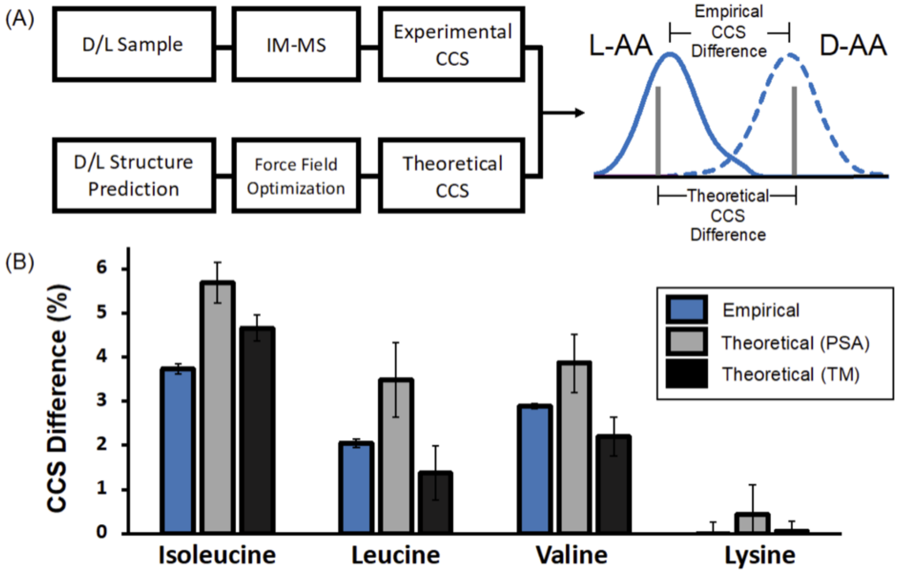

Figure B.6: (A) Simplified workflow merging computational modeling with IM-MS experimental results. (B) Comparison of CCS difference between empirically-measured and theoretically-derived trinuclear complexes for isoleucine, leucine, valine, and lysine enantiomer pairs.

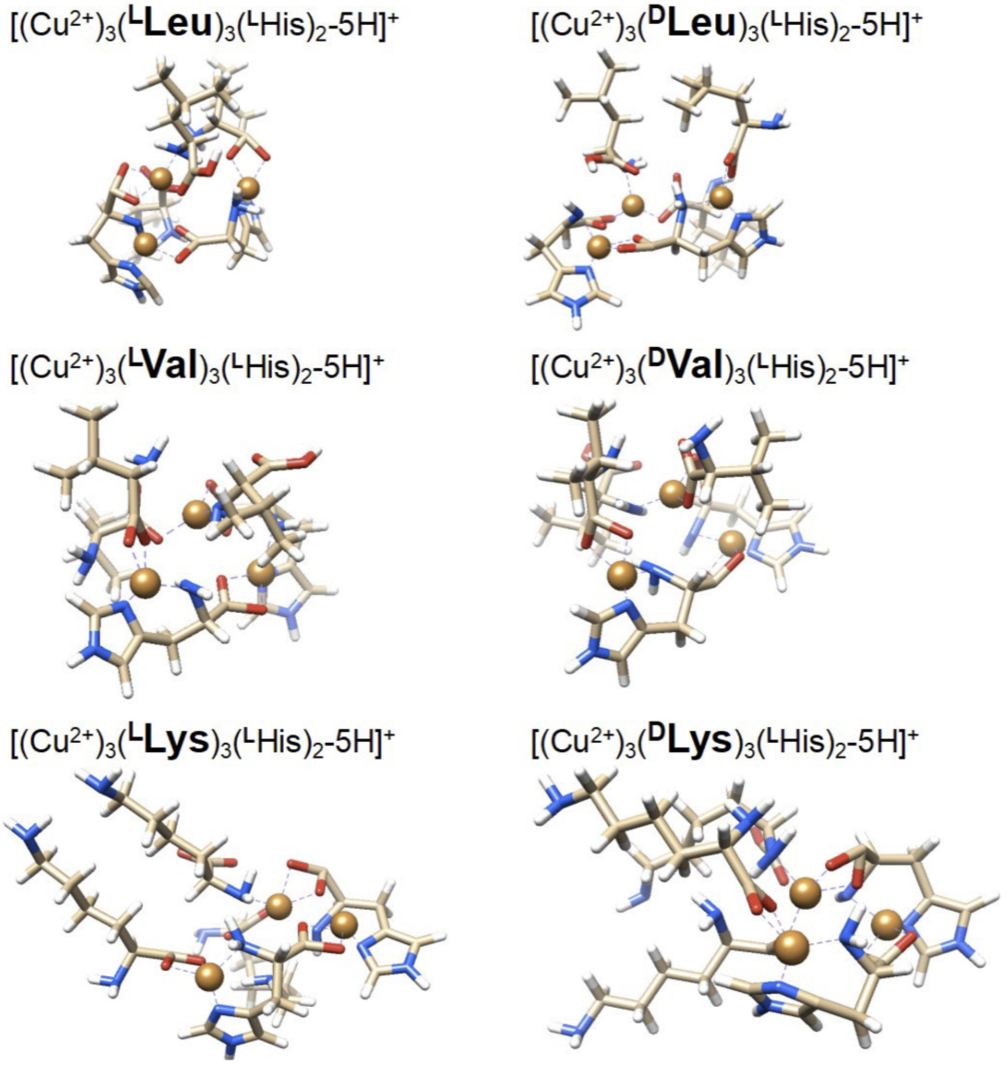

$[(\mathrm{Cu}^{2+})_3(^{\mathrm{L}}\mathbf{Leu})_3(^{\mathrm{L}}\mathrm{His})_2\text{-}5\mathrm{H}]^+$

$[(\mathrm{Cu}^{2+})_3(^{\mathrm{D}}\mathbf{Leu})_3(^{\mathrm{L}}\mathrm{His})_2\text{-}5\mathrm{H}]^+$

$[(\mathrm{Cu}^{2+})_3(^{\mathrm{L}}\mathbf{Val})_3(^{\mathrm{L}}\mathrm{His})_2\text{-}5\mathrm{H}]^+$

$[(\mathrm{Cu}^{2+})_3(^{\mathrm{D}}\mathbf{Val})_3(^{\mathrm{L}}\mathrm{His})_2\text{-}5\mathrm{H}]^+$

$[(\mathrm{Cu}^{2+})_3(^{\mathrm{L}}\mathbf{Lys})_3(^{\mathrm{L}}\mathrm{His})_2\text{-}5\mathrm{H}]^+$

$[(\mathrm{Cu}^{2+})_3(^{\mathrm{D}}\mathbf{Lys})_3(^{\mathrm{L}}\mathrm{His})_2\text{-}5\mathrm{H}]^+$

Figure B.7: Energy-minimized structures for leucine, valine, and lysine enantiomers.

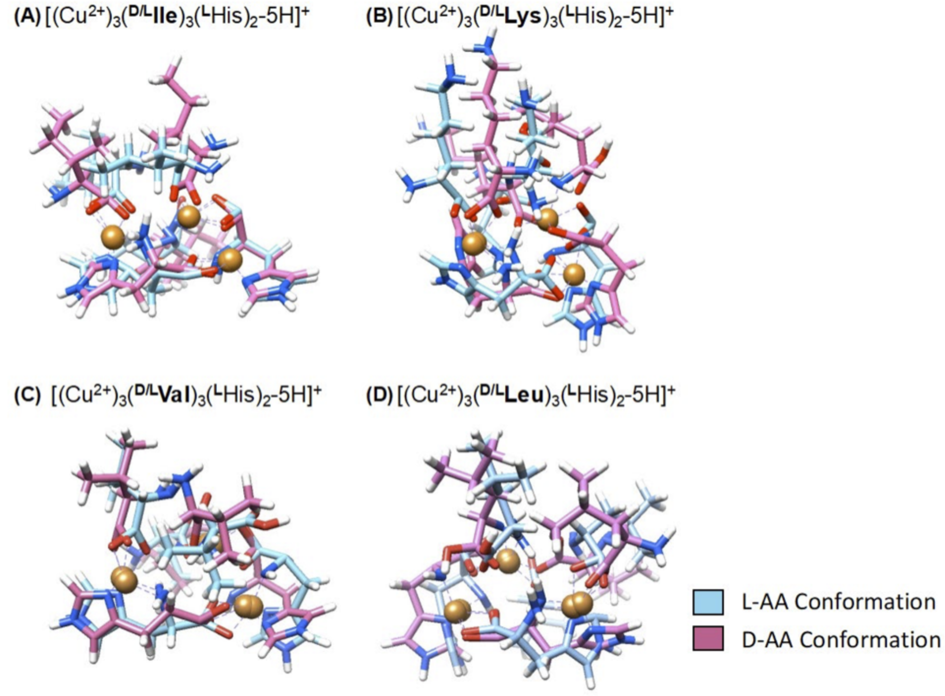

Figure B.8: Overlaid D- and L- conformations of (A) Isoleucine, (B) lysine, (C) valine, and (D) leucine.

Adduct	Charge	EXP m/z	Exact m/z	Error (PPM)
$[(Cu^{+2})C_2H_3N]^+$	1	103.9558	103.95615	3.37
$[(Cu^{+2})C_4H_6N_2]^+$	1	144.9823	144.98269	2.69
$[(Cu^{+2})(His)\text{-}H_2CO_2]^+$	1	171.993	171.99359	3.43
$[(Cu^{+2})(His)]^+$	1	217.9986	217.99907	2.16
$[(Cu^{+2})_2(His)+C_2H_4N]^+$	1	320.9463	320.94739	3.4
$[(Cu^{+2})_2(His)(Ile)\text{-}H_3CO_2]^+$	1	365.0094	365.010014	1.68
$[(Cu^{+2})_2(His)_2\text{-}H_3CO_2]^+$	1	388.9846	388.984862	0.67
$[(Cu^{+2})_2(Ile)(His)\text{-}2H+Na]^+$	1	432.9965	432.997434	2.16
$[(Cu^{+2})_2(Ile)_3\text{-}H_4CO_2]^+$	1	471.1208	471.121975	2.49
$[(Cu^{+2})_4(Ile)_2(His)_3\text{-}6H]^{+2}$	2	486.5333	486.534583	2.64
$[(Cu^{+2})_2(Ile)_2(His)\text{-}H_4CO_2]^+$	1	495.0956	495.096823	2.47
$[(Cu^{+2})_4(Ile)_5(His)\text{-}6H]^{+2}$	2	528.1057	528.107049	2.55
$[(Cu^{+2})_2(Ile)_2(His)\text{-}3H]^+$	1	540.0956	540.094473	-2.09
$[(Cu^{+2})_4(Ile)_3(His)_3\text{-}6H]^{+2}$	2	552.0806	552.081897	2.35
$[(Cu^{+2})_2(Ile)(His)_2\text{-}3H]^+$	1	564.0683	564.069321	1.81
$[(Cu^{+2})_3(Ile)_2(His)\text{-}3H]^+$	1	603.0232	603.02404	1.39
$[(Cu^{+2})_3(Ile)(His)_2\text{-}3H]^+$	1	626.9977	626.9989	1.91
$[(Cu^{+2})_5(Ile)_4(His)_3\text{-}8H]^{+2}$	2	648.0859	648.086191	0.45
$[(Cu^{+2})_2(Ile)_4\text{-}4H+Na]^+$	1	669.1951	669.196204	1.65
$[(Cu^{+2})_2(Ile)_3(His)\text{-}4H+Na]^+$	1	693.17	693.171052	1.52
$[(Cu^{+2})_2(Ile)_2(His)_2\text{-}4H+Na]^+$	1	717.1442	717.1459	2.37
$[(Cu^{+2})_3(Ile)_3(His)\text{-}5H]^+$	1	733.1168	733.110881	-8.07
$[(Cu^{+2})_2(Ile)(His)_3\text{-}4H+Na]^+$	1	741.1188	741.120748	2.63
$[(Cu^{+2})_3(Ile)_5\text{-}5H]^+$	1	839.221	839.222842	2.19
$[(Cu^{+2})_3(Ile)_4(His)\text{-}5H]^+$	1	863.1954	863.19769	2.65
$[(Cu^{+2})_3(Ile)_3(His)_2\text{-}5H]^+$	1	887.1715	887.1749	3.83
$[(Cu^{+2})_3(Ile)_3(His)_2\text{-}6H+Na]^+$	1	909.1526	909.154488	2.08
$[(Cu^{+2})_3(Ile)_6\text{-}6H+Na]^+$	1	992.2973	992.299421	2.14
$[(Cu^{+2})_3(Ile)_5(His)\text{-}6H+Na]^+$	1	1016.2719	1016.27427	2.33
$[(Cu^{+2})_3(Ile)_4(His)_2\text{-}6H+Na]^+$	1	1040.2473	1040.24912	1.75
$[(Cu^{+2})_4(Ile)_4(His)_2\text{-}7H]^+$	1	1079.1801	1079.18113	0.95
$[(Cu^{+2})_4(Ile)_3(His)_3\text{-}7H]^+$	1	1103.1535	1103.15597	2.24
$[(Cu^{+2})_4(Ile)_5(His)_2\text{-}7H]^+$	1	1210.2773	1210.27576	-1.28
$[(Cu^{+2})_4(Ile)_5(His)_2\text{-}8H+Na]^+$	1	1232.2559	1232.25771	1.47
$[(Cu^{+2})_4(Ile)_4(His)_3\text{-}8H+Na]^+$	1	1256.2311	1256.23255	1.16

Table B.1: Identified complexes observed in the mass spectra obtained from a mixture of isoleucine, copper acetate and L-histidine; presented in Figure 1 of the manuscript.

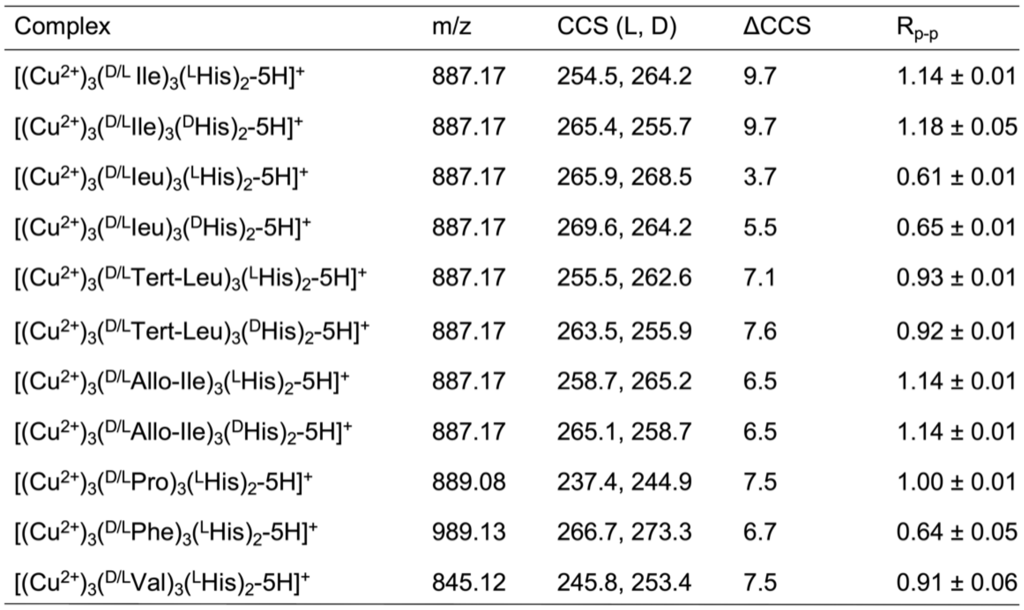

Complex	m/z	CCS (L, D)	ΔCCS	$R_{p\text{-}p}$
$[(\mathrm{Cu}^{2+})_3(^{\mathrm{D/L}}\,\mathrm{Ile})_3(^{\mathrm{L}}\mathrm{His})_2\text{-}5\mathrm{H}]^+$	887.17	254.5, 264.2	9.7	1.14 ± 0.01
$[(\mathrm{Cu}^{2+})_3(^{\mathrm{D/L}}\mathrm{Ile})_3(^{\mathrm{D}}\mathrm{His})_2\text{-}5\mathrm{H}]^+$	887.17	265.4, 255.7	9.7	1.18 ± 0.05
$[(\mathrm{Cu}^{2+})_3(^{\mathrm{D/L}}\mathrm{leu})_3(^{\mathrm{L}}\mathrm{His})_2\text{-}5\mathrm{H}]^+$	887.17	265.9, 268.5	3.7	0.61 ± 0.01
$[(\mathrm{Cu}^{2+})_3(^{\mathrm{D/L}}\mathrm{leu})_3(^{\mathrm{D}}\mathrm{His})_2\text{-}5\mathrm{H}]^+$	887.17	269.6, 264.2	5.5	0.65 ± 0.01
$[(\mathrm{Cu}^{2+})_3(^{\mathrm{D/L}}\mathrm{Tert\text{-}Leu})_3(^{\mathrm{L}}\mathrm{His})_2\text{-}5\mathrm{H}]^+$	887.17	255.5, 262.6	7.1	0.93 ± 0.01
$[(\mathrm{Cu}^{2+})_3(^{\mathrm{D/L}}\mathrm{Tert\text{-}Leu})_3(^{\mathrm{D}}\mathrm{His})_2\text{-}5\mathrm{H}]^+$	887.17	263.5, 255.9	7.6	0.92 ± 0.01
$[(\mathrm{Cu}^{2+})_3(^{\mathrm{D/L}}\mathrm{Allo\text{-}Ile})_3(^{\mathrm{L}}\mathrm{His})_2\text{-}5\mathrm{H}]^+$	887.17	258.7, 265.2	6.5	1.14 ± 0.01
$[(\mathrm{Cu}^{2+})_3(^{\mathrm{D/L}}\mathrm{Allo\text{-}Ile})_3(^{\mathrm{D}}\mathrm{His})_2\text{-}5\mathrm{H}]^+$	887.17	265.1, 258.7	6.5	1.14 ± 0.01
$[(\mathrm{Cu}^{2+})_3(^{\mathrm{D/L}}\mathrm{Pro})_3(^{\mathrm{L}}\mathrm{His})_2\text{-}5\mathrm{H}]^+$	889.08	237.4, 244.9	7.5	1.00 ± 0.01
$[(\mathrm{Cu}^{2+})_3(^{\mathrm{D/L}}\mathrm{Phe})_3(^{\mathrm{L}}\mathrm{His})_2\text{-}5\mathrm{H}]^+$	989.13	266.7, 273.3	6.7	0.64 ± 0.05
$[(\mathrm{Cu}^{2+})_3(^{\mathrm{D/L}}\mathrm{Val})_3(^{\mathrm{L}}\mathrm{His})_2\text{-}5\mathrm{H}]^+$	845.12	245.8, 253.4	7.5	0.91 ± 0.06

Table B.2: Collision cross section measurements for trinuclear complexes with measured two-peak resolutions (R_{p-p}) of greater than 0.6.

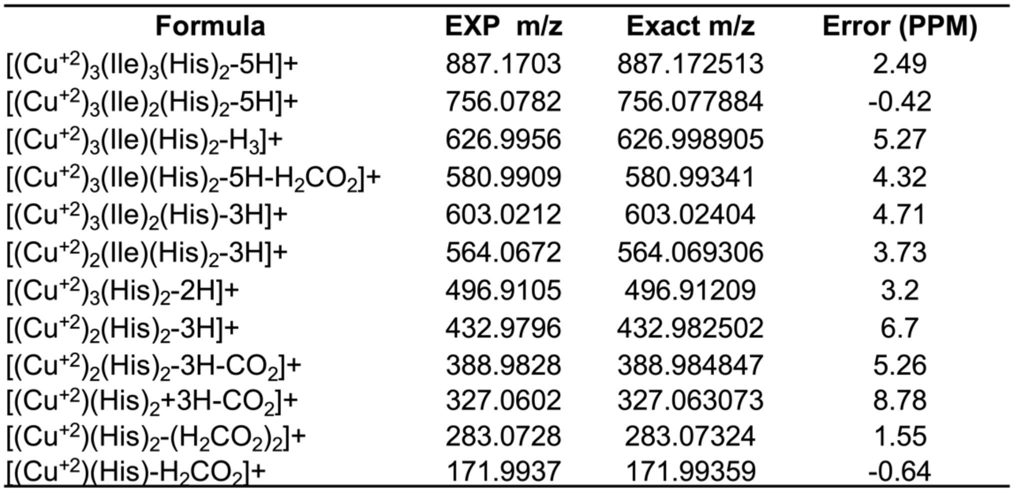

Formula	EXP m/z	Exact m/z	Error (PPM)
$[(Cu^{+2})_3(Ile)_3(His)_2\text{-}5H]+$	887.1703	887.172513	2.49
$[(Cu^{+2})_3(Ile)_2(His)_2\text{-}5H]+$	756.0782	756.077884	-0.42
$[(Cu^{+2})_3(Ile)(His)_2\text{-}H_3]+$	626.9956	626.998905	5.27
$[(Cu^{+2})_3(Ile)(His)_2\text{-}5H\text{-}H_2CO_2]+$	580.9909	580.99341	4.32
$[(Cu^{+2})_3(Ile)_2(His)\text{-}3H]+$	603.0212	603.02404	4.71
$[(Cu^{+2})_2(Ile)(His)_2\text{-}3H]+$	564.0672	564.069306	3.73
$[(Cu^{+2})_3(His)_2\text{-}2H]+$	496.9105	496.91209	3.2
$[(Cu^{+2})_2(His)_2\text{-}3H]+$	432.9796	432.982502	6.7
$[(Cu^{+2})_2(His)_2\text{-}3H\text{-}CO_2]+$	388.9828	388.984847	5.26
$[(Cu^{+2})(His)_2+3H\text{-}CO_2]+$	327.0602	327.063073	8.78
$[(Cu^{+2})(His)_2\text{-}(H_2CO_2)_2]+$	283.0728	283.07324	1.55
$[(Cu^{+2})(His)\text{-}H_2CO_2]+$	171.9937	171.99359	-0.64

Table B.3: MS^2 Identifications of isoleucine trinuclear copper complexes with L-histidine CS.

Appendix C

Supplemental Material Chapter 3

6-M-6

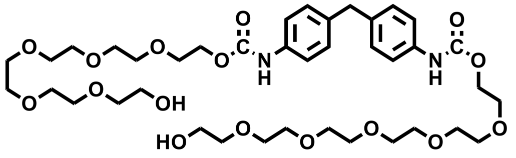

4-M-8

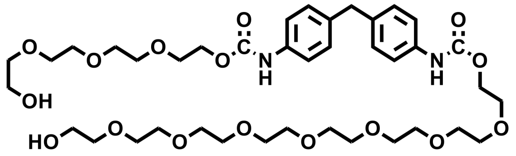

2-M-10

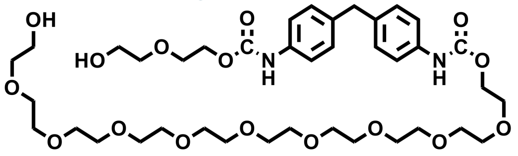

Figure C.1: PEG oligomers structures.

Vasopressin

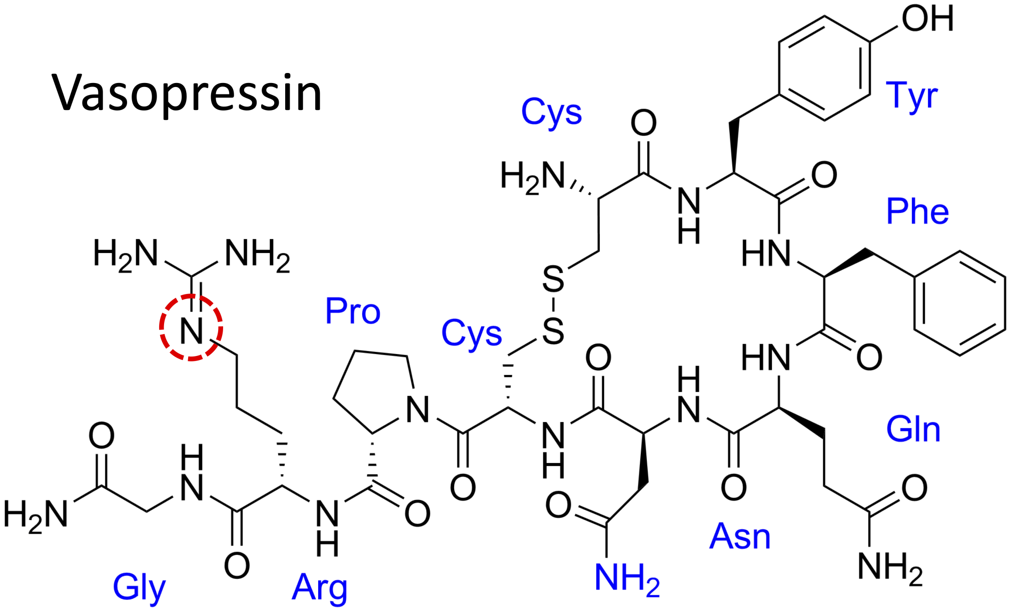

Pressinoic Acid

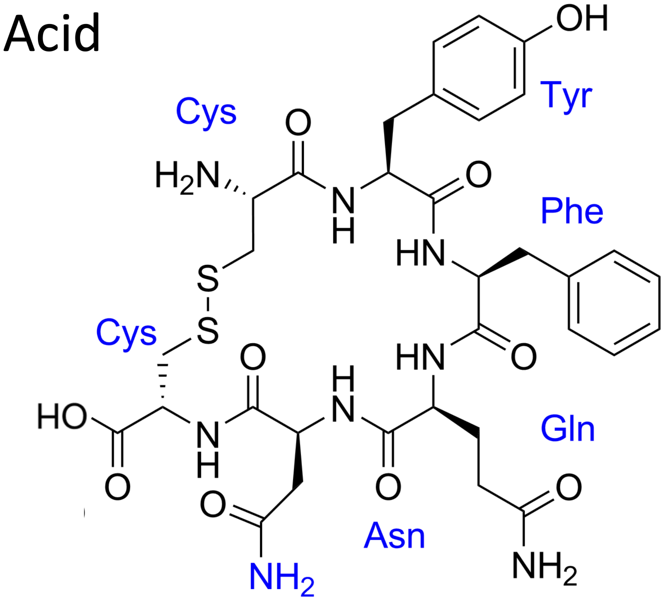

Figure C.2: Nonapeptides structures.

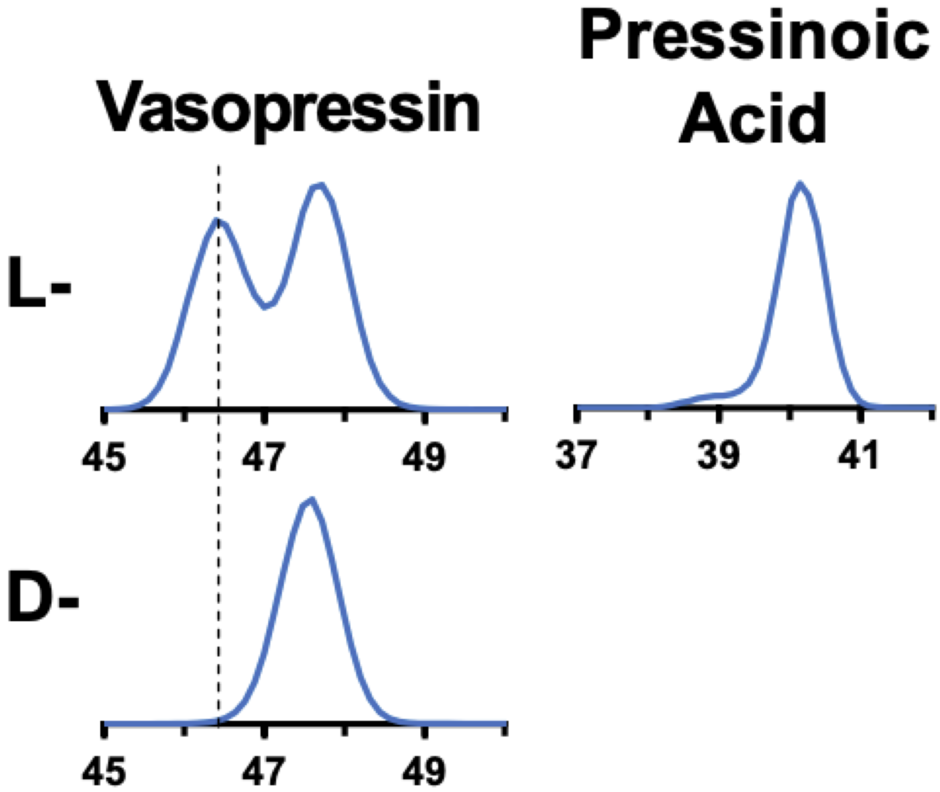

Figure C.3: Protonated nonapeptides IM-MS spectra acquired on Agilent 6560.

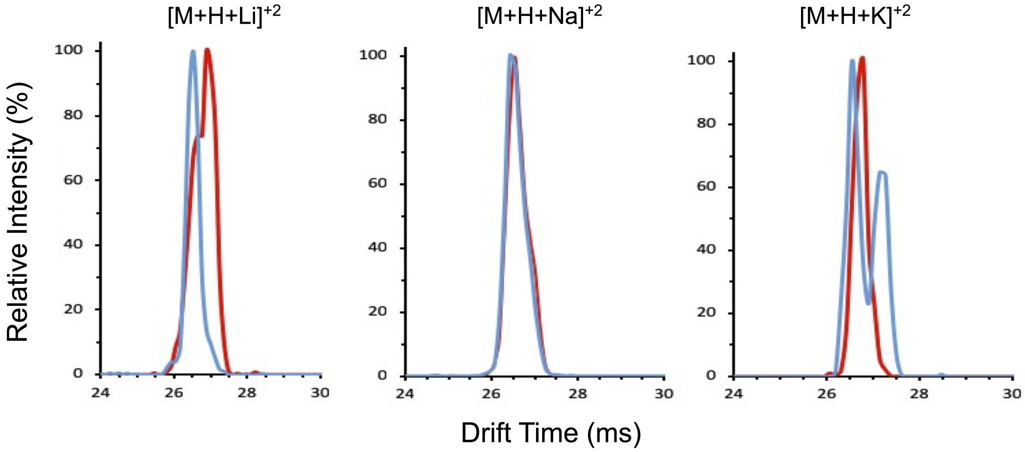

Figure C.4: Vasopressin IM-MS spectra acquired on Agilent 6560 mass spectrometer of the [M+H+X]+2 adduct.

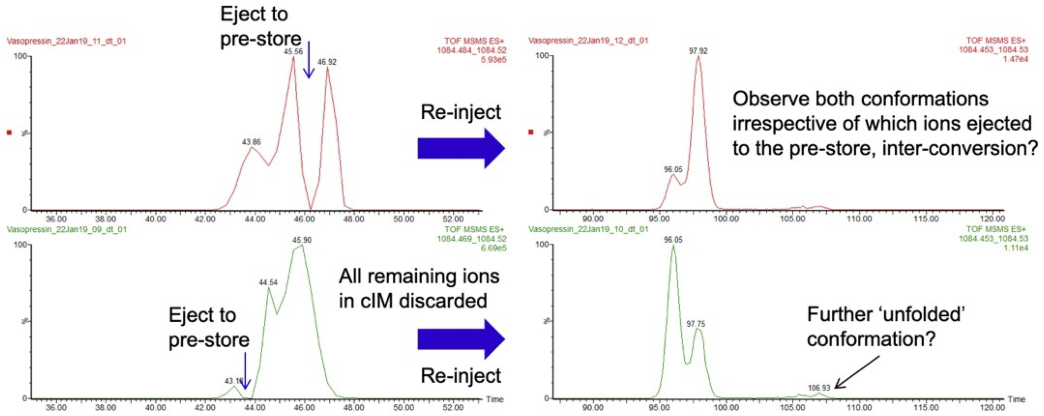

Figure C.5: Protonated Vasopressin tandem IM-MS experiment. Ion ”slices” were taken from each distributions and reinjected in the cIM.

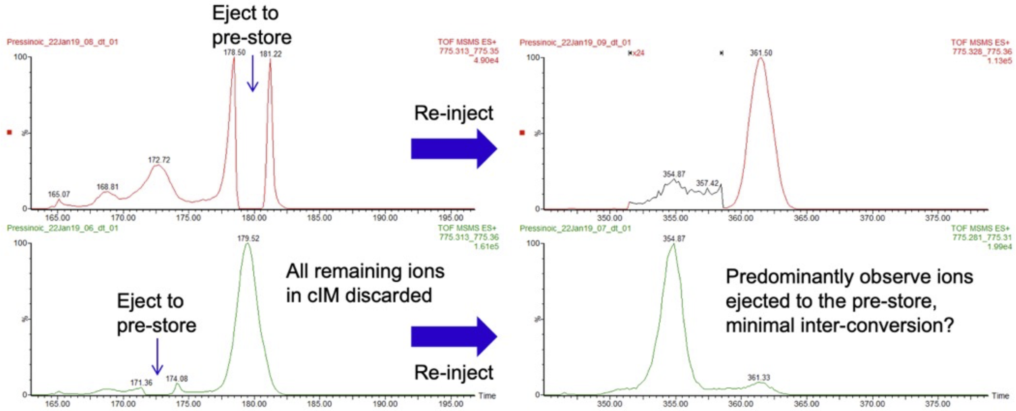

Figure C.6: Protonated pressinoic acid tandem IM-MS experiment. Ion ”slices” were taken from each distributions and reinjected in the cIM.

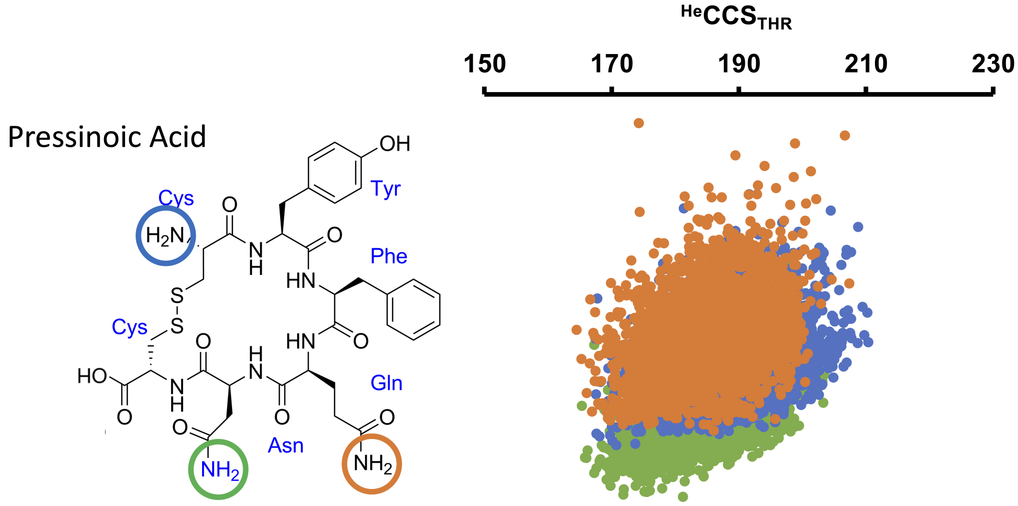

Figure C.7: Theoretical modeling results of protonated pressinoic acid. Three protonation sites were explored.

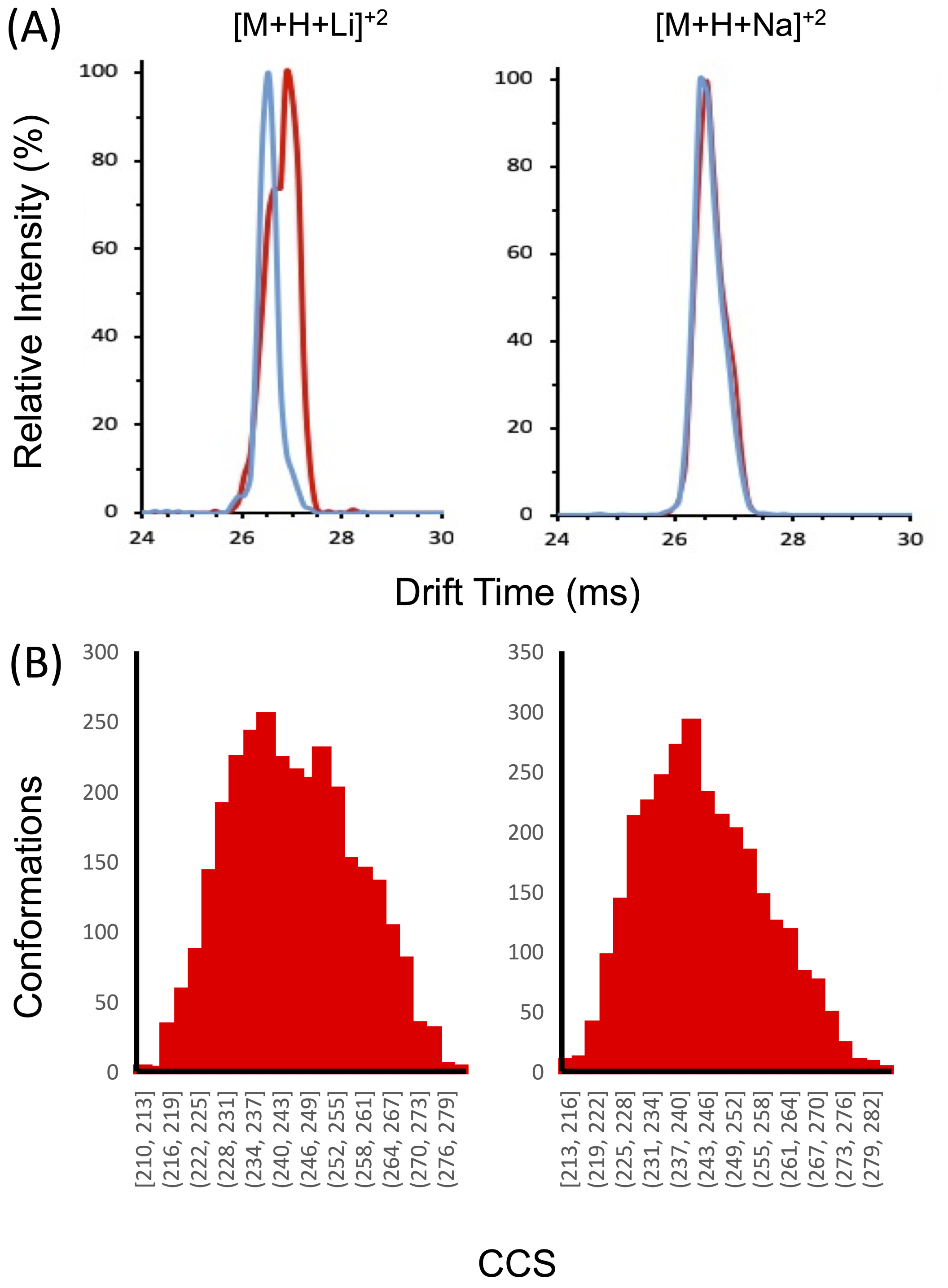

Figure C.8: $[\text{Vaso+H+X}]^{+2}$ (where X= Li or Na) adduct (A) IM-MS spectra collect on Agilent 6560 and (B) theoretical modeling results.

(A) [L-Vasopressin + H + Li]$^{+2}$

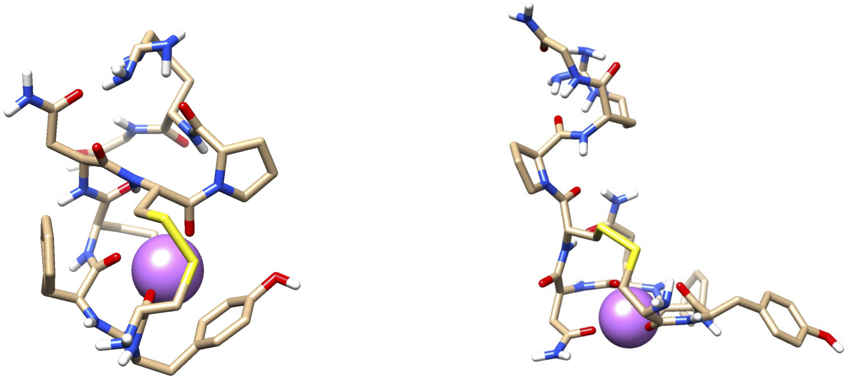

"Shoulder"

(B) [L-Vasopressin + H + Na]$^{+2}$

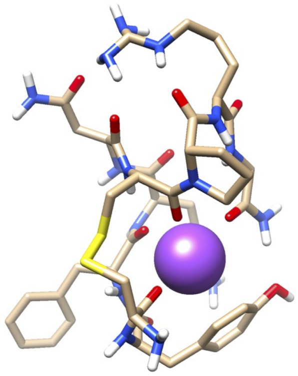

Figure C.9: Lowest energy structures of theoretical modeling of L-vasopressin.

Appendix D

Supplemental Material Chapter 4

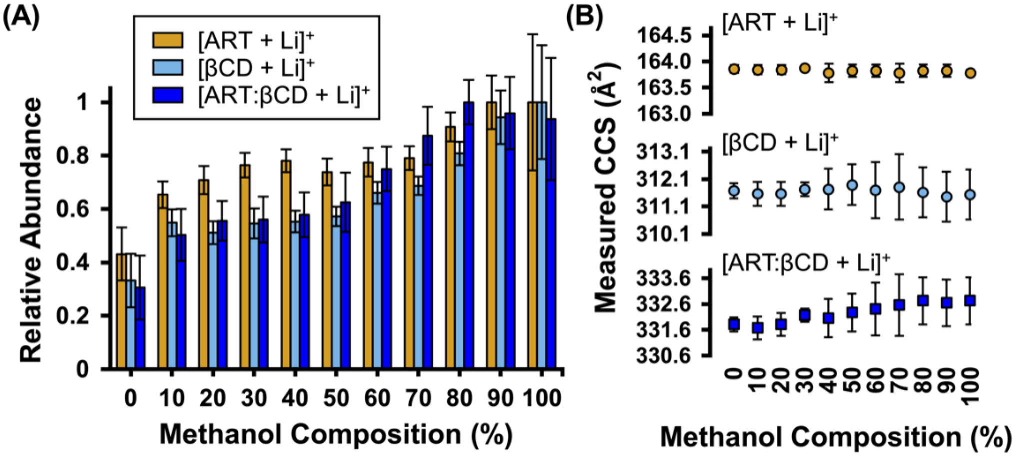

Figure D.1: (A) Relative abundance of three select ions from the artemisinin:β- cyclodextrin:lithium acetate (1:10:10) sample, and (B) corresponding CCS measurements. Data was acquired in triplicate (intra-day, randomized). The CCS projections are scaled to ±0.5% of the average CCS to facilitate direct comparisons.

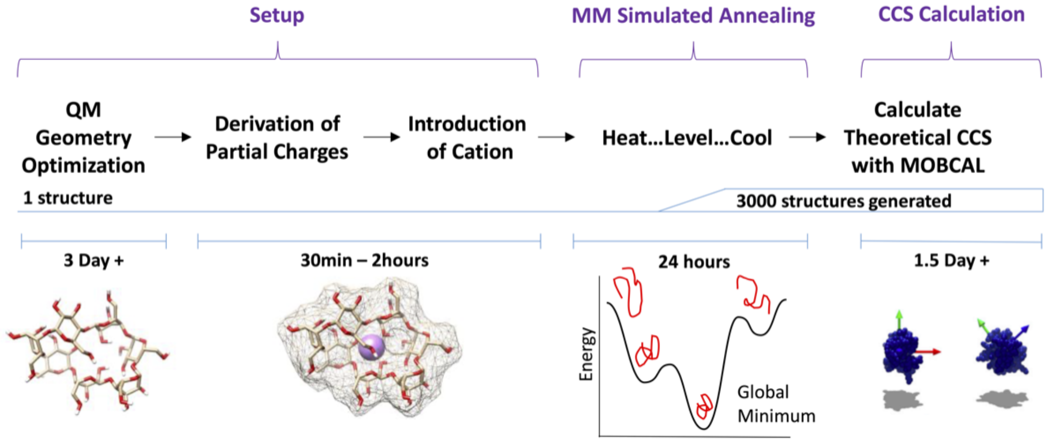

Figure D.2: Computational workflow optimized in this study. A starting structure is geometry- optimized using density functional theory, then the charge carrier is added and the resulting ion structure is subjected to simulated annealing to generate 3000 candidate structures. The CCS of these 3000 structures is then determined using the parameterized trajectory method in MOBCAL, then plotted as a function of the relative energy and subsequently compared with empirical CCS measurements in helium.

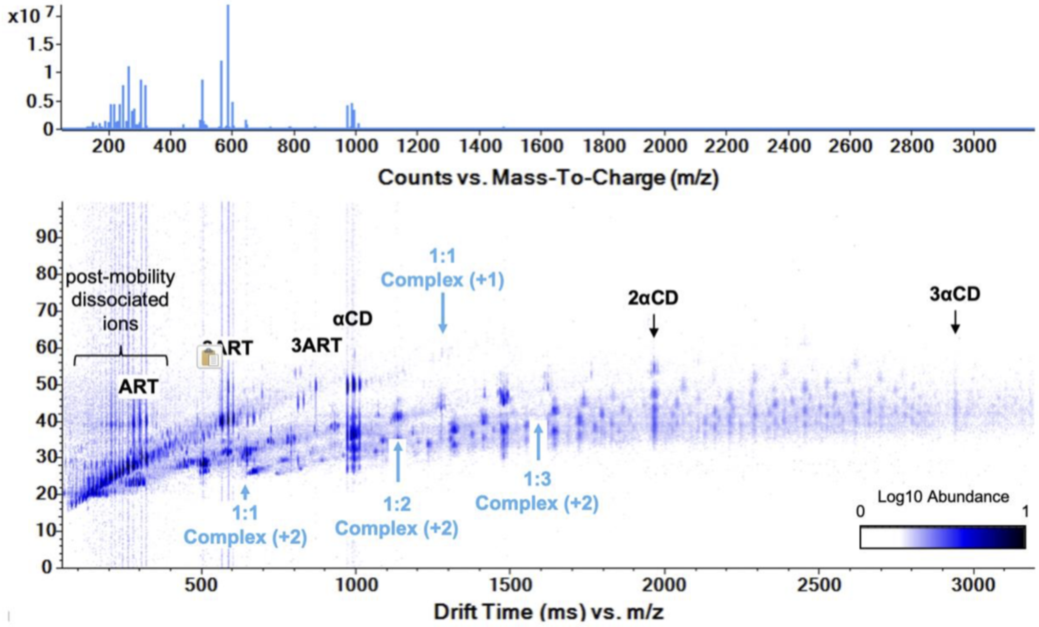

Figure D.3: DTIMS-MS spectrum of artemisinin with -cyclodextrin and lithium acetate (1:10:10). Artemisinin:CD (1:1, 1:2, 1:3).

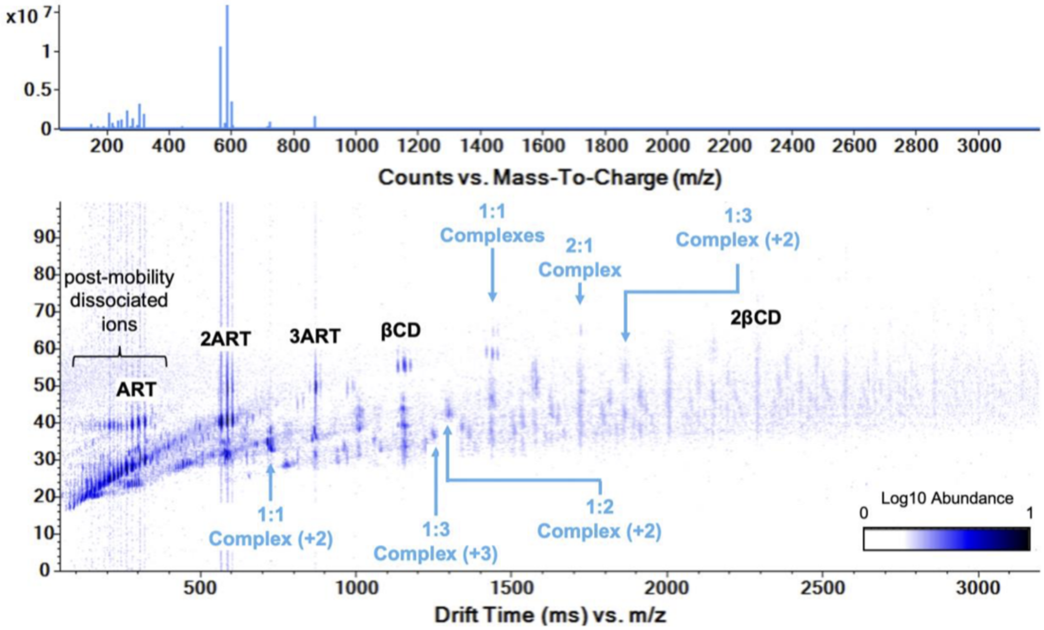

Figure D.4: DTIMS-MS spectrum of artemisinin with -cyclodextrin and lithium acetate (1:10:10). Artemisinin:CD (1:1, 1:2, 1:3, 2:1).

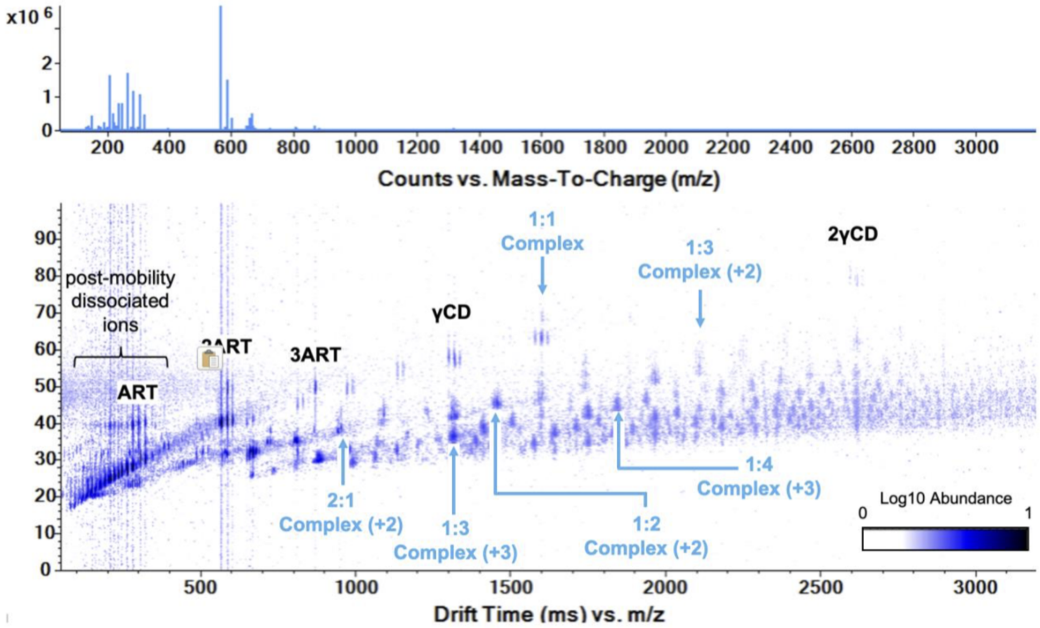

Figure D.5: DTIMS-MS spectrum of artemisinin with -cyclodextrin and lithium acetate (1:10:10). Artemisinin:CD (1:1, 1:2, 1:3, 1:4, 2:1).

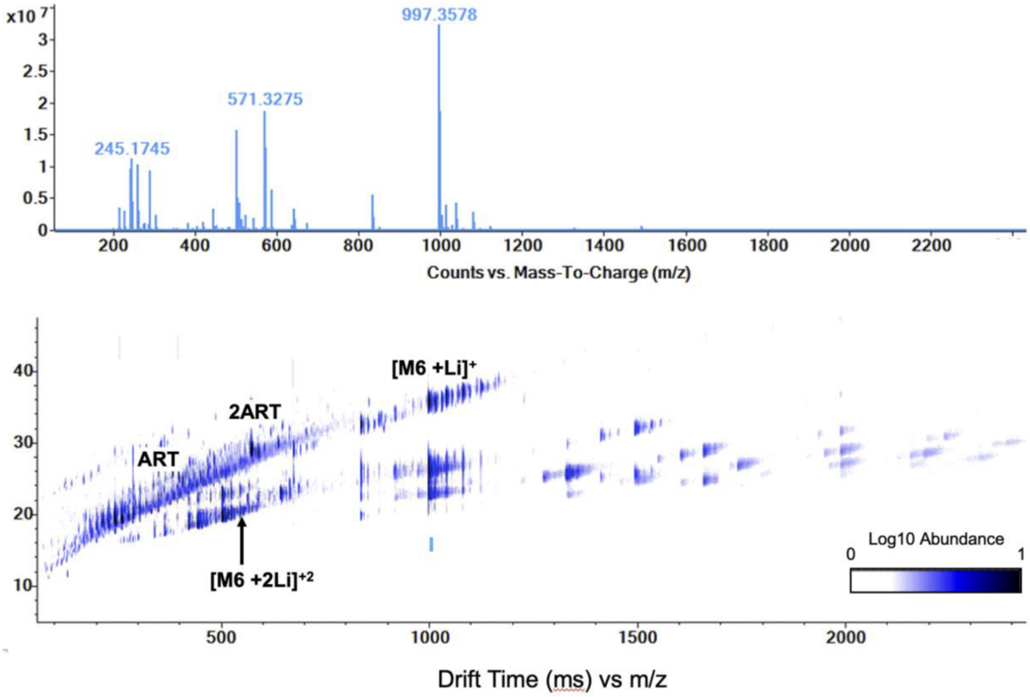

Figure D.6: DTIMS-MS spectrum of artemisinin with maltohexaose and lithium acetate (1:10:10).

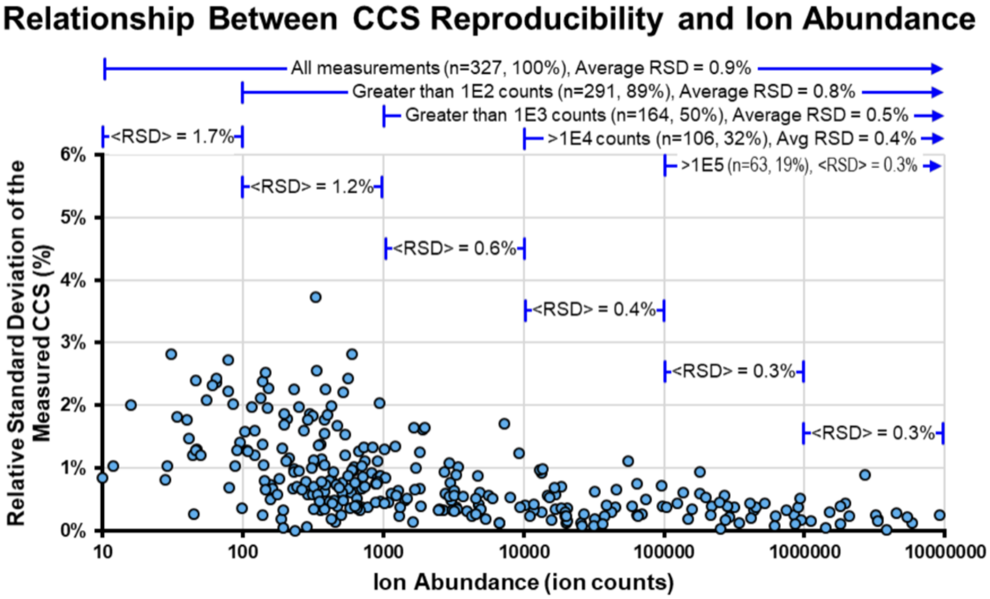

Figure D.7: DTIMS-MS empirically-observed relationship between the ion abundance (measured in arbitrary ion counts) and the CCS reproducibility (measured as a percent relative standard deviation, RSD). Intuitively, the reproducibility of the CCS measurement is dependent on the ion abundance, as sufficient ion counts are needed to accurately reproduce the ion mobility distribution and corresponding peak centroid used to determine the CCS. In this study, the reproducibility is found to be high (0.5% average RSD) for ion counts above 1,000 (0.05% relative ion abundance), and only improves marginally at higher abundances.

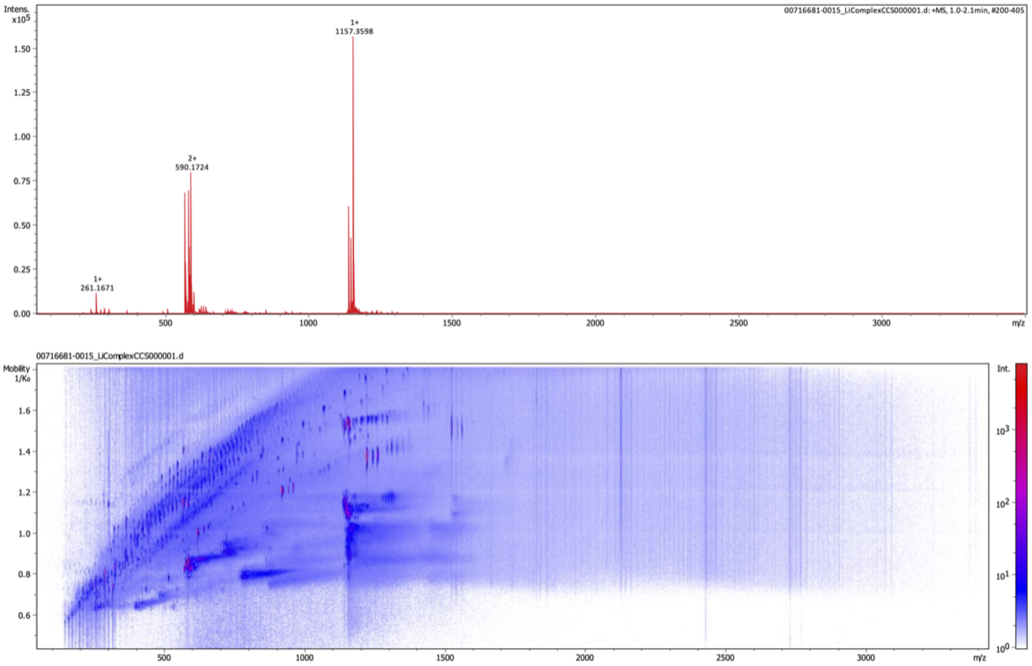

Figure D.8: Full ESI(+) scan IM-MS spectrum of artemisinin with beta-cyclodextrin and lithium acetate on TIMS-TOF.

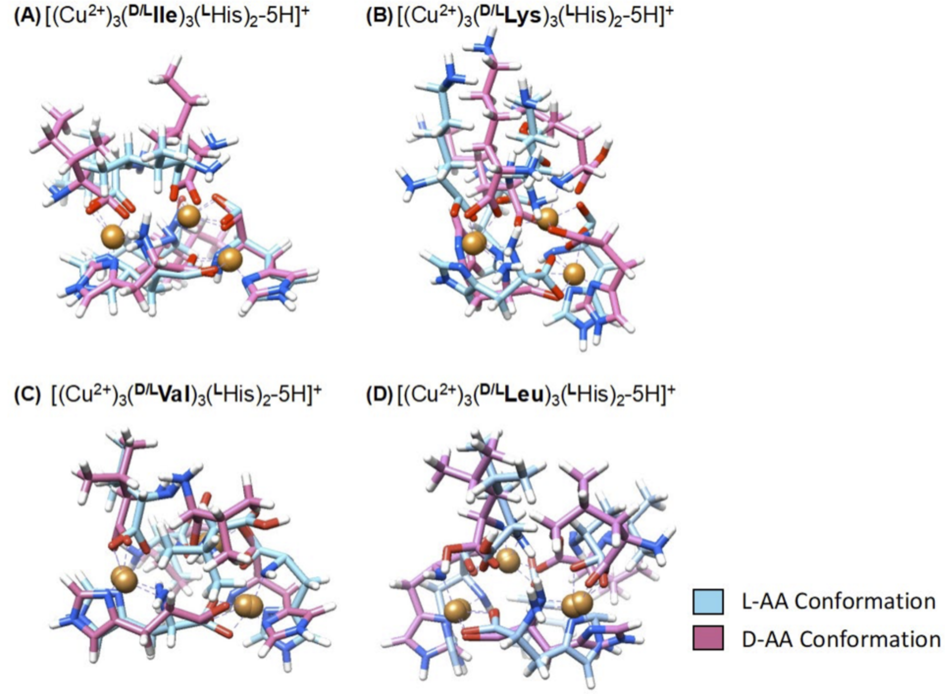

Figure D.9: Overlaid D- and L- conformations of (A) Isoleucine, (B) lysine, (C) valine, and (D) leucine.

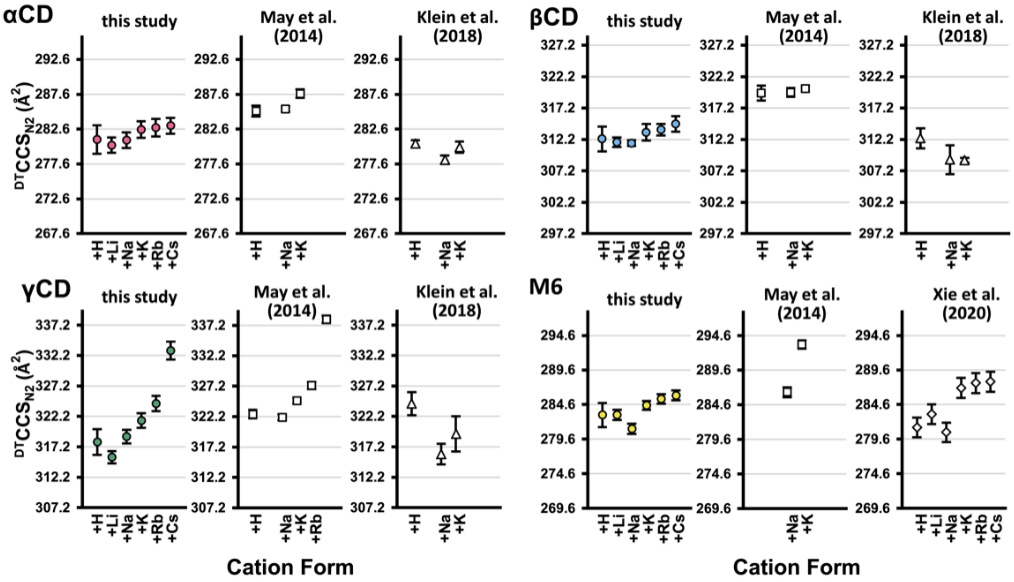

Figure D.10: Comparison of oligosaccharide CCS measurements obtained in this study (DTIMS- MS) with CCS values previously published in the literature. Agreement is within 3%, however the relative trends observed for each analyte is reproduced, which suggests the same gas-phase structures are being sampled in these different studies.

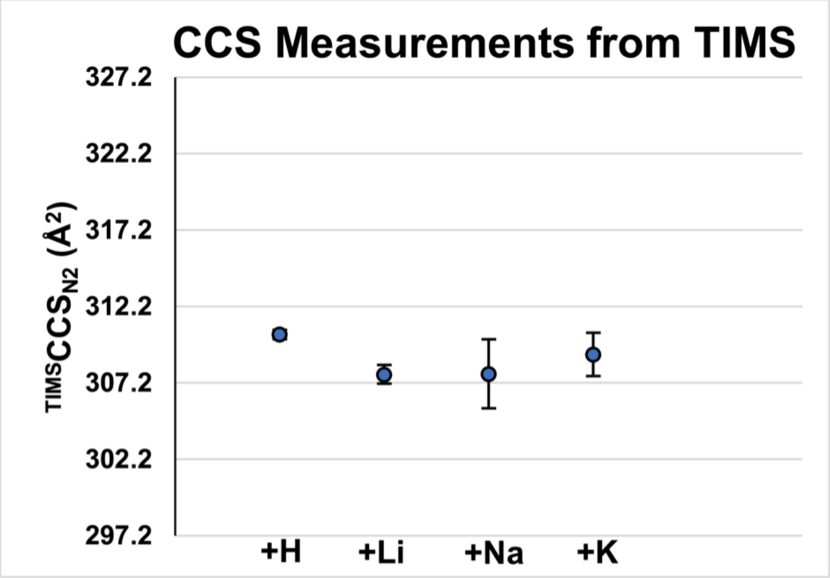

complex	1	2	3	average	SD
$[\beta CD + H]^+$	310.3	310.7	310.1	310.4	0.3
$[\beta CD + Li]^+$	307.9	307.1	308.3	307.8	0.6
$[\beta CD + Na]^+$	306.6	306.4	310.4	307.8	2.3
$[\beta CD + K]^+$	308.2	308.3	310.7	309.1	1.4

Figure D.11: Comparison of oligosaccharide CCS measurements obtained on the TIMS-TOF. Relative trends observed for each analyte are consistent with observations from the DTIMS, which suggests the same gas-phase structures are being sampled with TIMS.

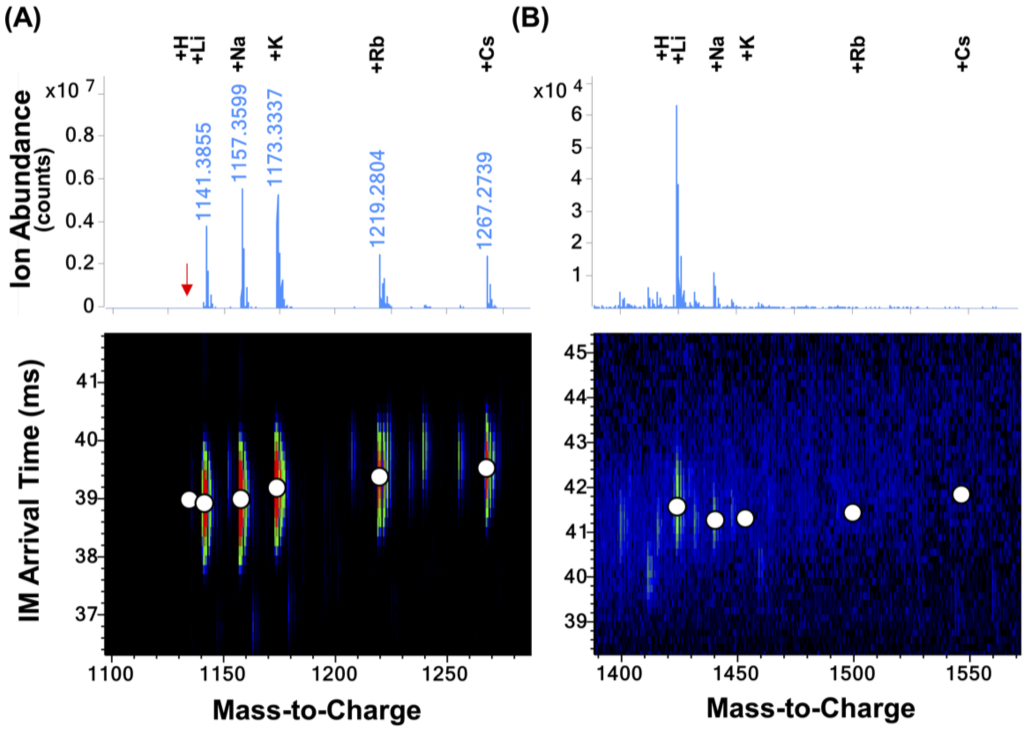

Figure D.12: DTIMS-MS spectra from cation competition experiments in which an equimolar mixture of the five acetate salts (Li, Na, K, Rb, Cs) was introduced to a sample solution containing artemisinin and CD. As with the other experiments, βCD and the acetate salt mixture were added at a 10x excess to artemisinin to promote complex/adduct ion formation (artemisinin:βCD:acetate salt; 1:10:10). Expanded regions of the spectra for (A) βCD and (B) artemisinin:βCD complexes are shown. White dots have been added to help locate the peak apices and regions in the mass spectrum is annotated were the cation-bound species are expected to appear.

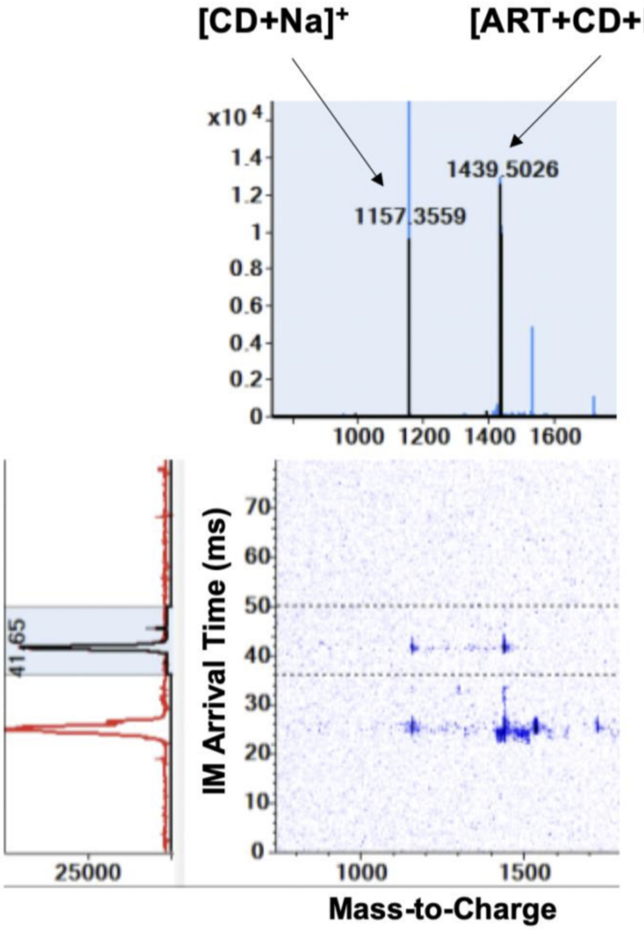

Figure D.13: DTIMS-tandem MS spectra of the [artemisinin:βCD + Na]+ ion. The mobility spectrum presents two distinct sets of fragment ions post quadrupole isolation (at 25 ms and 40 ms), with the higher arrival time fragments being from the ion of interest. The ions at lower arrival time (25 ms) exhibit non-structural fragments as well as signals appearing at m/z values higher than the isolated precursor, indicating these are artifacts. Using mobility as a filter is an important step taken in this work to improve the confidence in the generated SY plots for CD complexes.

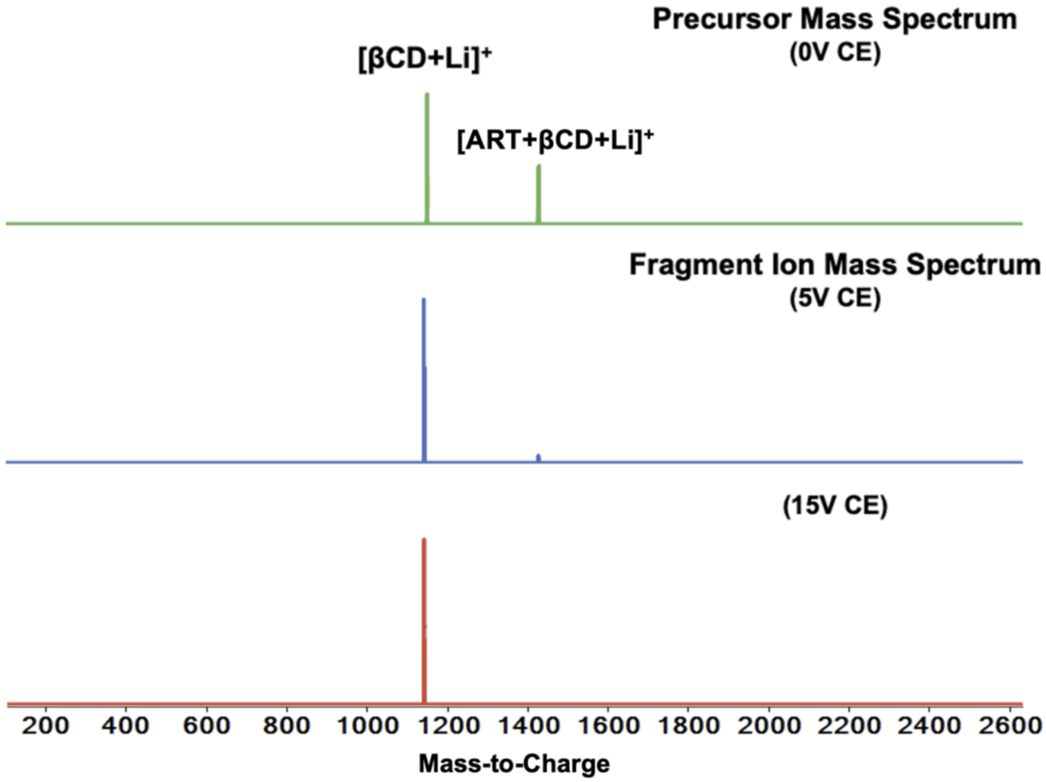

Figure D.14: DTIMS-tandem MS/MS spectra of [artemisinin:βCD + Li]$^+$ at 0, 5, and 15 eV. At 0 eV, the primary ion dissociates with nearly complete dissociation at 15eV. Interesting to note, fragmentation of primary ion resulted in [βCD + Li]$^+$, but no observed [artemisinin + Li]$^+$ fragment ions (m/z = 289.1617), suggesting that the charge carrier preferentially forms a strong interaction with CD molecules. Because of this preferred interaction the drug:CD complexes, the SY projections are expected to be more representative of artemisinin interaction with CDs than of cation dissociation.

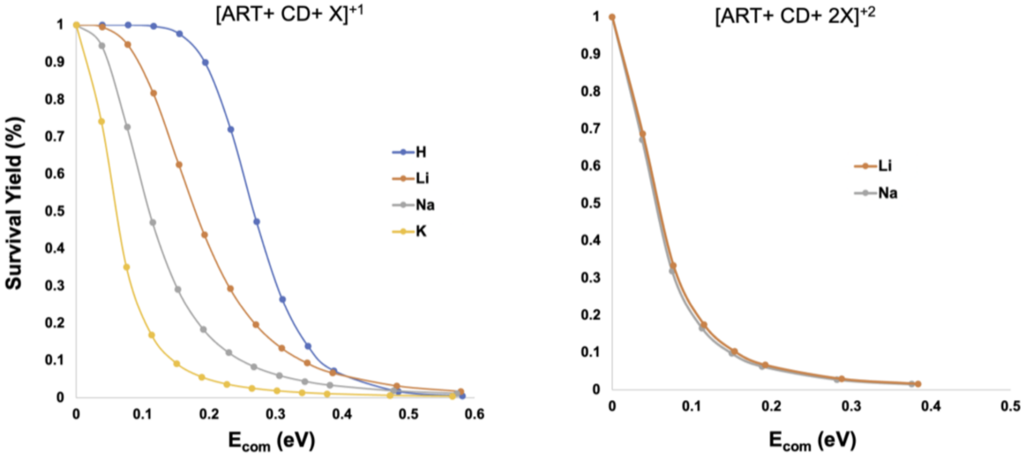

Figure D.15: Tandem MS SY curves of the [artemisinin:βCD + X]$^{+1}$ ion (X = H, Li, Na, K) demonstrates a decreased stability of the ion complex with increasing cation and trend reversal is observed with the +2 charge state ion [artemisinin:βCD + X]$^{+2}$ (X = Li, Na). Whereas an appropriate comparison of drug:CD interaction entails comparing across the same charge carrier, a challenge with exploring artemisinin:CD interaction preference arises because no single charge carrier exists in high abundance across all drug-CDs tested for the +1 charge state. (A) Measurements from the Agilent 6560 DTIMS-QTOF.

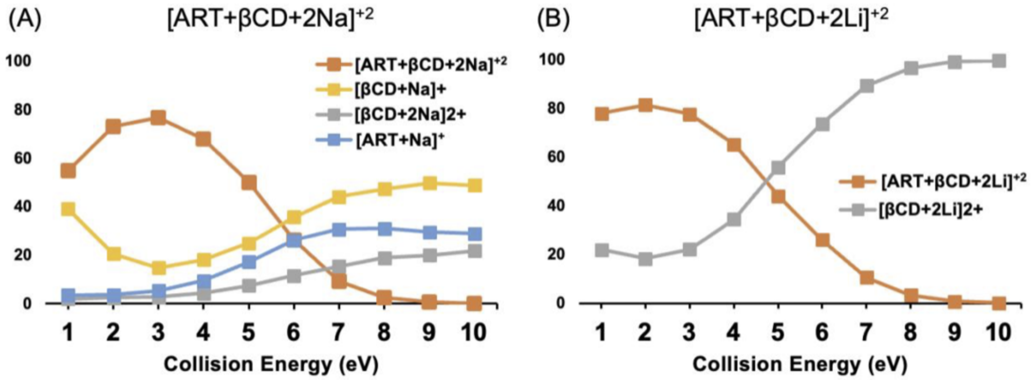

Figure D.16: Tandem MS/MS primary ion breakdown curves of (A) [artemisinin:βCD + 2Na]$^{+}$2 and (B) [artemisinin:βCD + 2Li]$^{+2}$ ions collected on the Bruker TIMS-TOF Pro.

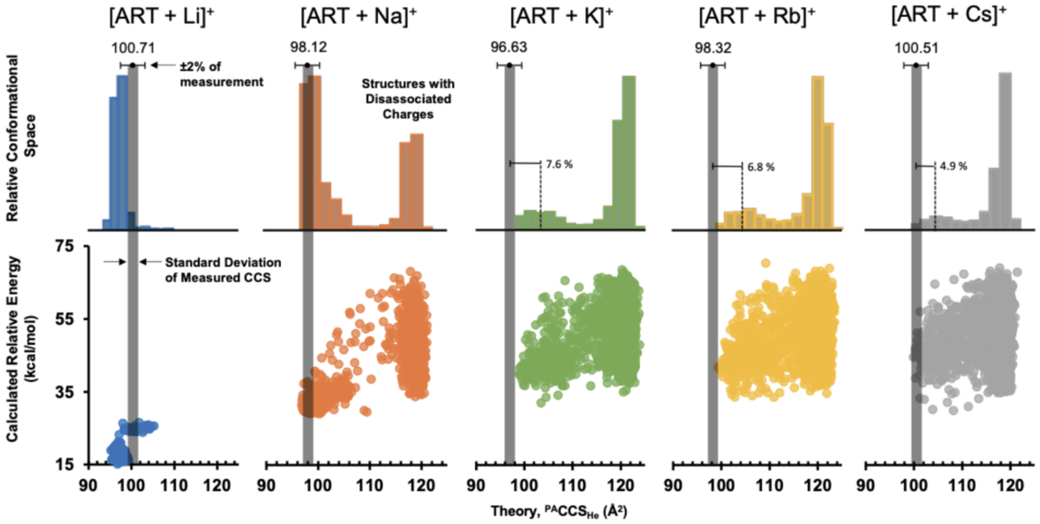

Figure D.17: Computational results for artemisinin with various cations. Theoretically-predicted CCS values are plotted relative to their calculated energies in the lower plots. The empirical helium CCS measurements are projected as shaded vertical bars, with the width of the bar corresponding to the experimental standard deviation of each measurement. Here, a second distribution of structures appears at higher CCS resulting from disassociation of the cation from artemisinin during the energy-minimization step—these higher CCS structures would not be observable in the IM-MS analysis. Overall good agreement is observed between experiment and theory for Li and Na (¡2%), and deviates for the larger sized cations (5 to 8%).

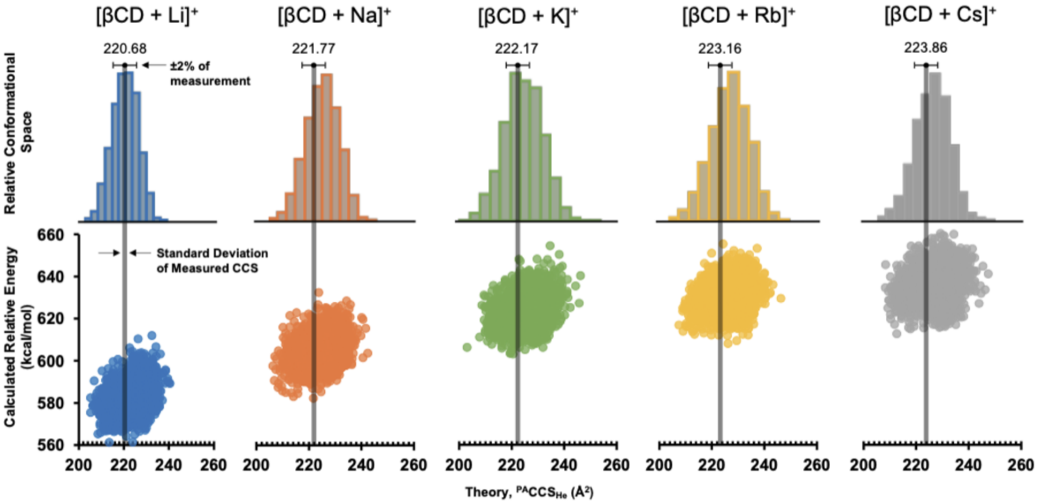

Figure D.18: Computational results for βCD with various cations. Here, agreement between experiment and theory is all within ca. 2%, indicated with the horizontal error bars.

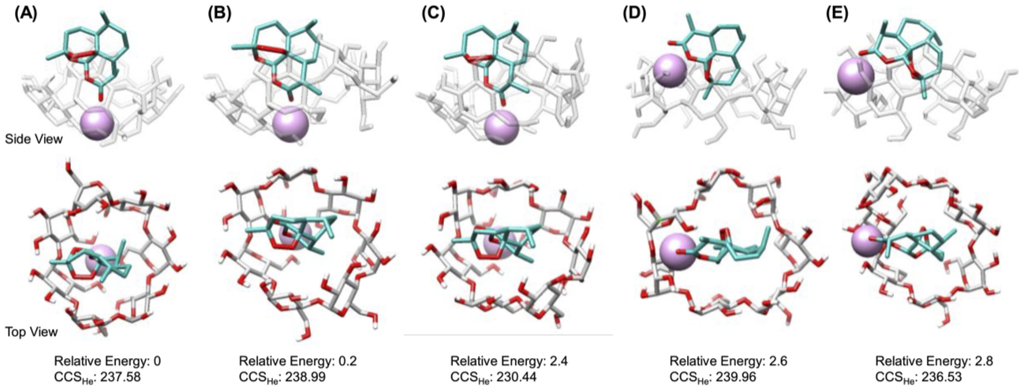

Figure D.19: Five lowest-energy structures of the 1:1 [artemisinin:βCD + Li]$^+$ ion complex that fall within the experimental CCS range. The three lowest energy structures at left orient artemisinin with the ketone group facing the larger βCD cavity and lithium occupying the smaller opening of the cavity.

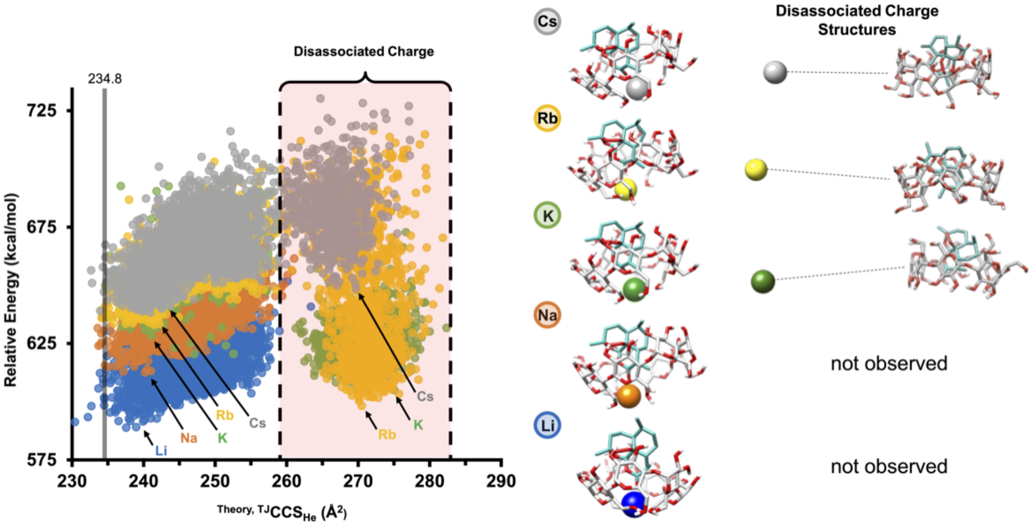

Figure D.20: Computational results for the singly-charged artemisinin:βCD complex with various charge carriers. The lower energy portion of the conformational distributions (at left) have the closest correspondence to the experimentally-measured CCS, indicated with the grey vertical bar. Lithium-adducted ART:βCD exhibits the lowest energy, followed by sodium-adducted ions. At right are the lowest energy structures (called out with the arrows in the left plot) for two clusters of conformations. The structures at high CCS exhibit a cation which is disassociated from the analyte and thus are not expected in the empirical data. Finally, the lowest-energy structures in which the cation is associated with ART:βCD are all inclusion complexes in which the cation localizes at the smaller opening of the cyclodextrin barrel. Experimental CCS of 234.8 noted with transparent grey bar.

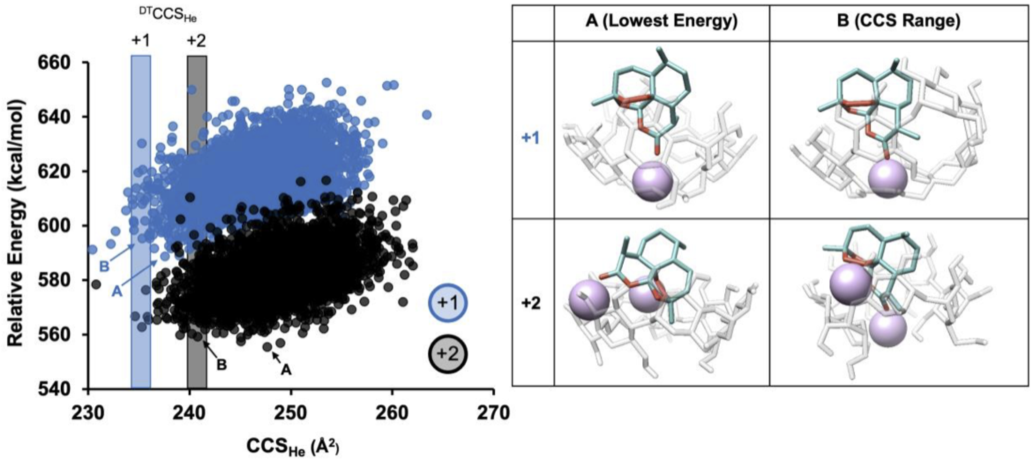

Figure D.21: Computational results for the singly- and doubly-lithium bound ART:βCD complex. Experimental CCS noted with transparent blue (+1) and black (+2) bar.

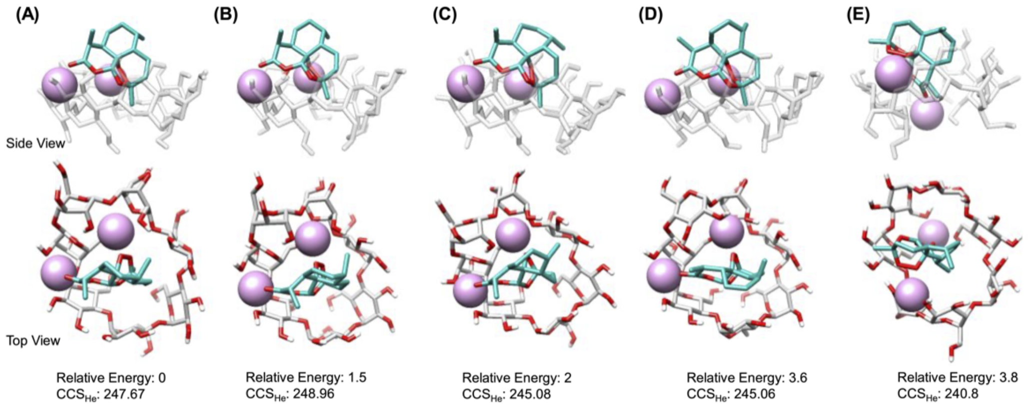

Figure D.22: The five lowest-energy structures of the double-lithium ART:βCD ion complex. Structures are presented from low to higher relative energies from left to right. The first four structures at left all suggest a gas-phase complex in which both lithium cations share the larger opening of the cyclodextrin with artemisinin.

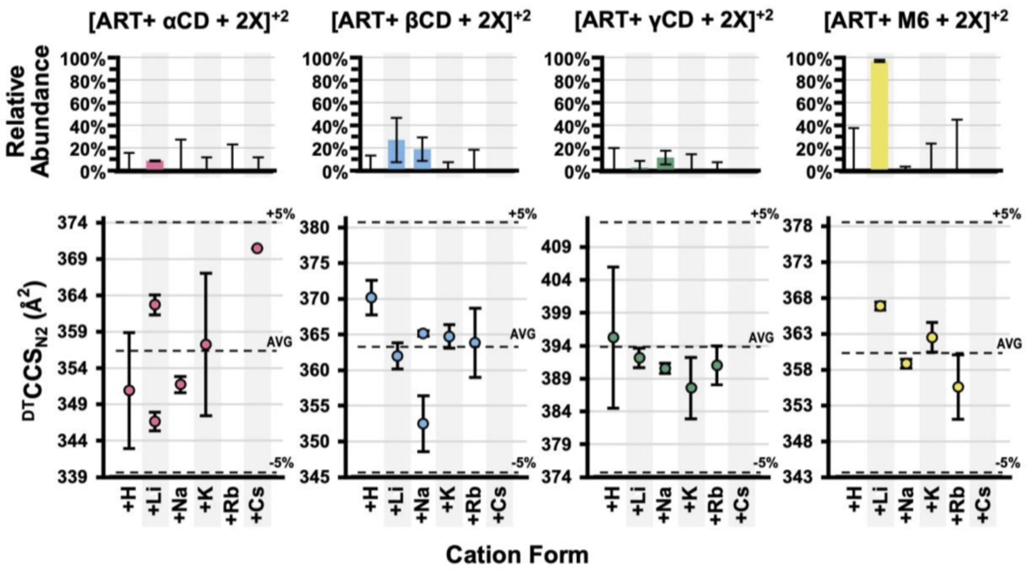

Figure D.23: Relative ion abundances (n>3) and collision cross sections across different charge carriers for the 1:1 complexes with two identical charge carriers (z=2).

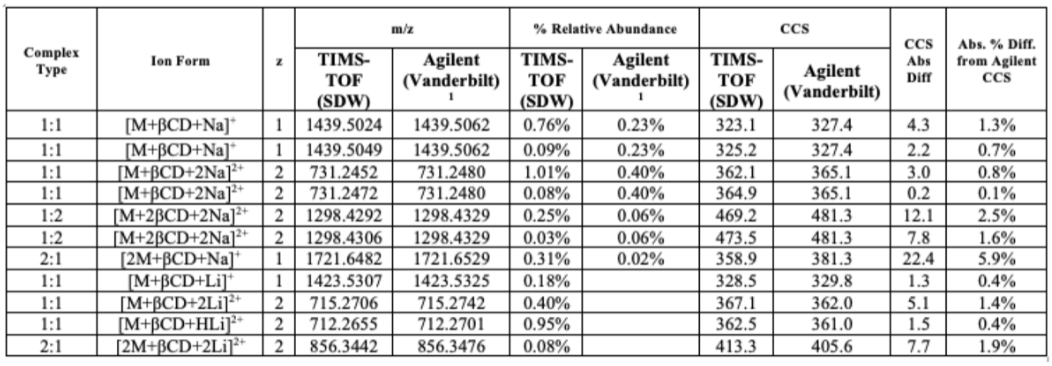

Complex Type	Ion Form	z	m/z		% Relative Abundance		CCS		CCS Abs Diff	Abs. % Diff. from Agilent CCS
			TIMS-TOF (SDW)	Agilent (Vanderbilt)[1]	TIMS-TOF (SDW)	Agilent (Vanderbilt)[1]	TIMS-TOF (SDW)	Agilent (Vanderbilt)		
1:1	$[M+\beta CD+Na]^{+}$	1	1439.5024	1439.5062	0.76%	0.23%	323.1	327.4	4.3	1.3%
1:1	$[M+\beta CD+Na]^{+}$	1	1439.5049	1439.5062	0.09%	0.23%	325.2	327.4	2.2	0.7%
1:1	$[M+\beta CD+2Na]^{2+}$	2	731.2452	731.2480	1.01%	0.40%	362.1	365.1	3.0	0.8%
1:1	$[M+\beta CD+2Na]^{2+}$	2	731.2472	731.2480	0.08%	0.40%	364.9	365.1	0.2	0.1%
1:2	$[M+2\beta CD+2Na]^{2+}$	2	1298.4292	1298.4329	0.25%	0.06%	469.2	481.3	12.1	2.5%
1:2	$[M+2\beta CD+2Na]^{2+}$	2	1298.4306	1298.4329	0.03%	0.06%	473.5	481.3	7.8	1.6%
2:1	$[2M+\beta CD+Na]^{+}$	1	1721.6482	1721.6529	0.31%	0.02%	358.9	381.3	22.4	5.9%
1:1	$[M+\beta CD+Li]^{+}$	1	1423.5307	1423.5325	0.18%		328.5	329.8	1.3	0.4%
1:1	$[M+\beta CD+2Li]^{2+}$	2	715.2706	715.2742	0.40%		367.1	362.0	5.1	1.4%
1:1	$[M+\beta CD+HLi]^{2+}$	2	712.2655	712.2701	0.95%		362.5	361.0	1.5	0.4%
2:1	$[2M+\beta CD+2Li]^{2+}$	2	856.3442	856.3476	0.08%		413.3	405.6	7.7	1.9%

Table D.1: Comparison of complex CCS measurements between Drift tube and TIMS-TOF. M used to represent artemisinin drug within adduct.

CCS of Dextrins (Å²)

	+H	+Li	+Na	+K	+Rb	+Cs
αCD	281.1	280.3	281.0	282.5	282.8	283.1
βCD	312.3	311.8	311.6	313.3	313.8	314.7
γCD	325.3	315.5	318.9	321.5	324.3	333.0
M6	283.1	283.1	281.1	284.5	285.4	285.9

CCS of Artemisinin:Dextrin Complexes (Å²)

	+H	+Li	+Na	+K	+Rb	+Cs
ART:αCD	335.4	329.6	329.8	329.3	329.6	331.6
ART:βCD	337.2	329.8	327.4	328.1	329.3	329.4
ART:γCD	354.7	355.4	355.1	353.0	353.7	354.3
ART:M6	323.4	326.3	316.7	318.1	321.2	313.7

Increase in CCS Upon Coordination

	+H	+Li	+Na	+K	+Rb	+Cs
αCD → ART:αCD	17.6%	16.2%	16.0%	15.3%	15.3%	15.8%
βCD → ART:βCD	7.7%	5.6%	5.0%	4.6%	4.8%	4.6%
γCD → ART:γCD	8.7%	11.9%	10.8%	9.3%	8.7%	6.2%
M6 → ART:M6	13.3%	14.2%	11.9%	11.2%	11.8%	9.3%

Table D.2: Measured change in oligosaccharide CCS upon coordination with artemisinin across all cations.

Ion Form	Exact *m/z*	$^{DT}CCS_{N2}$ (Å^2)	$^{DT}CCS_{He}$ (Å^2)
[βCD + Li]$^+$	1141.2745	311.8	221.4
[βCD + Na]$^+$	1157.3593	311.6	221.8
[ART:βCD + Li]$^+$	1423.5325	329.8	234.8
[ART:βCD + Na]$^+$	1439.5062	327.4	--
[ART:βCD + 2Li]$^{+2}$	715.2745	362.0	240.7

Table D.3: Drift tube CCS measurements obtained in nitrogen ($^{DT}\text{CCS}_{N2}$) and helium ($^{DT}\text{CCS}_{He}$) drift gas for βCD and the artemisinin:βCD complexes (Li and Na). The helium CCS values have less contribution of the drift gas and are used for alignment with computational results.

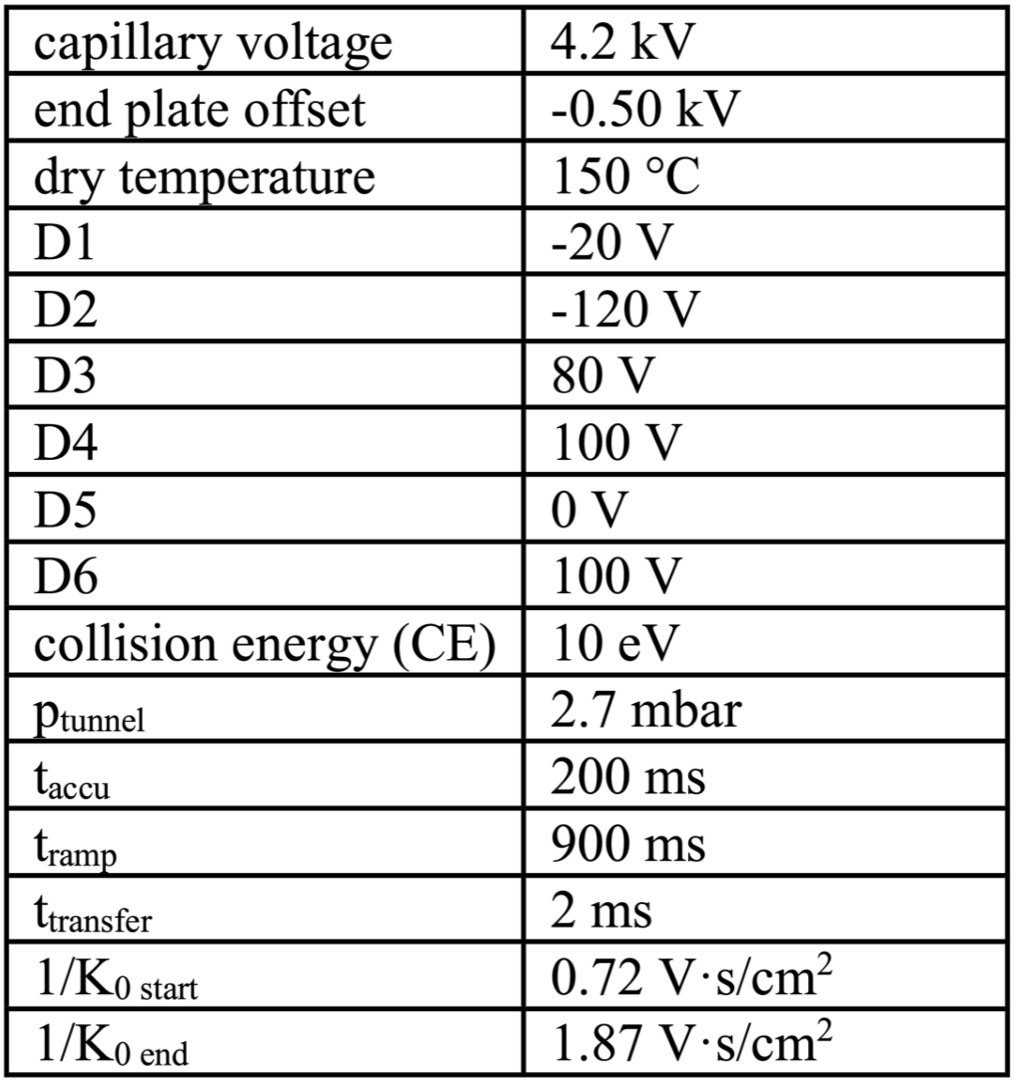

capillary voltage	4.2 kV
end plate offset	-0.50 kV
dry temperature	150 °C
D1	-20 V
D2	-120 V
D3	80 V
D4	100 V
D5	0 V
D6	100 V
collision energy (CE)	10 eV
p_{tunnel}	2.7 mbar
t_{accu}	200 ms
t_{ramp}	900 ms
$t_{transfer}$	2 ms
$1/K_{0\ start}$	$0.72\ V \cdot s/cm^2$
$1/K_{0\ end}$	$1.87\ V \cdot s/cm^2$

Table D.4: Description of TIMS-TOF instrument parameters.

Appendix E

Supplemental Material Chapter 5

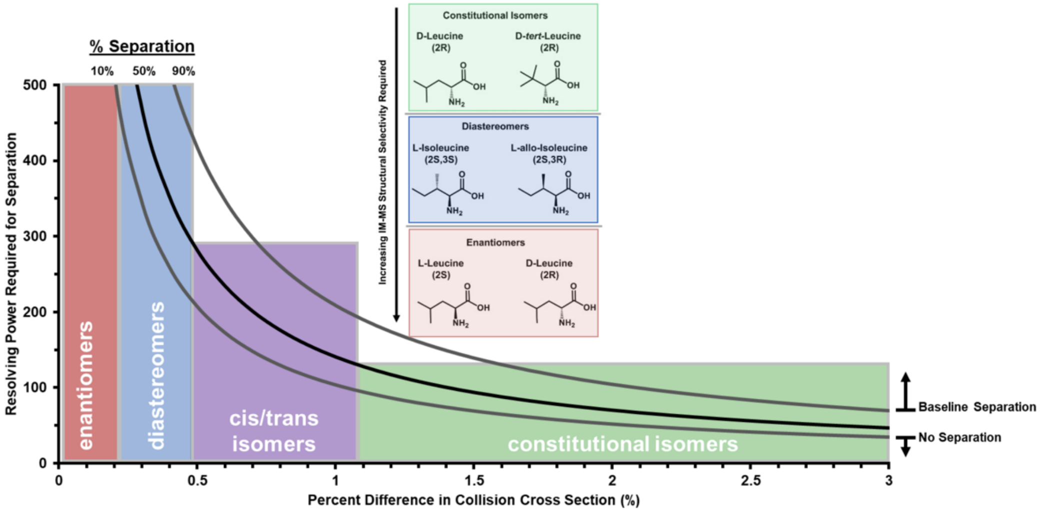

Figure E.1: Schematic of IMS resolving power necessary to separate isomer classes.

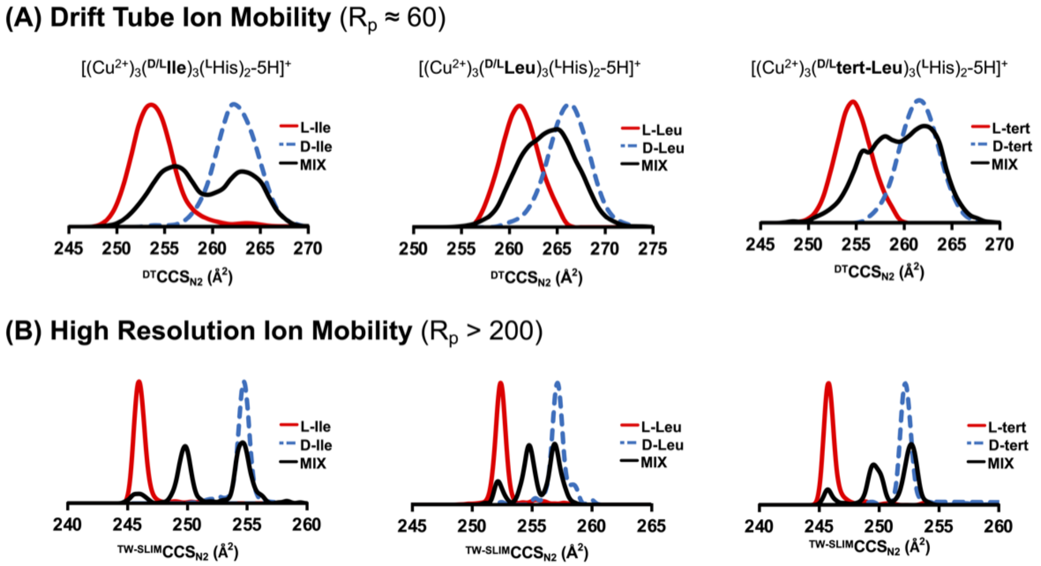

Figure E.2: Tri-nuclear copper complexes of Isoluecine, Leucine, and tert-leucine with an L-histidine chiral selector acquired on a (A) drift tube (B) and SLIM IM-MS platforms.